NISTIR 88-3886

Research for Electric Energy Systems - - An Annual Report

R. J. Van Brunt, Editor

75 Years Stimulating America's Progress
1913-1988

NISTIR 88-3886

Research for Electric Energy Systems - - An Annual Report

R. J. Van Brunt, Editor

U.S. DEPARTMENT OF COMMERCE
National Institute of Standards and Technology
(Formerly National Bureau of Standards)
Center for Electronics and Electrical Engineering
Electrosystems Division
Gaithersburg, MD 20899

December 1987

Issued November 1988

National Bureau of Standards became the National Institute of Standards and Technology on August 23, 1988, when the Omnibus Trade and Competitiveness Act was signed. NIST retains all NBS functions. Its new programs will encourage improved use of technology by U.S. industry.

U.S. DEPARTMENT OF COMMERCE
C. William Verity, Secretary

NATIONAL INSTITUTE OF STANDARDS
AND TECHNOLOGY
Ernest Ambler, Director

TABLE OF CONTENTS

Foreword

This report summarizes the progress of four technical investigations conducted during FY 87. Although reasonable efforts have been made to ensure the reliability of the data presented, it must be emphasized that this is an interim progress report and that further experimentation and analysis may be performed before the conclusions from any of these investigations are formally published. It is therefore possible that some of the observations presented in this report will be modified, expanded, or clarified by our subsequent research.

RESEARCH FOR ELECTRIC ENERGY SYSTEMS -- AN ANNUAL REPORT

Richard J. Van Brunt, Editor

Abstract

This report documents the technical progress in the four investigations which make up the project "Support of Research Projects for Electrical Energy Systems", Department of Energy Task Order Number 137, funded by the U.S. Department of Energy and performed by the Electrosystems Division of the National Institute of Standards and Technology (NIST). The first investigation covers the measurement of ions in the vicinity of dc high-voltage transmission lines and in biological exposure facilities designed to simulate power line environments. Two techniques for measuring ion mobilities in air were evaluated, namely a pulsed time-of-flight (TOF) drift-tube and an AC TOF drift-tube. The problems associated with extracting reliable mobilities from TOF data are discussed. The second investigation addresses concerns with electrical breakdown and chemical decomposition of commonly used gaseous dielectrics like SF_6. For this investigation, the results from a number of separate activities are reported. Examples of results from direct measurement of the temperature dependences of the rate coefficients for F^- transfer reactions between SF_6^- and various discharge generated contaminants like SOF_4, SOF_2, SO_2, SF_4, and SiF_4 are presented. Also covered is an analysis of the electron transport and swarm parameters in SF_6 using numerical solutions of the Boltzmann transport equation to find an improved "complete" set of electron-collision cross sections that were then used to compute electron-impact rate coefficients for SF_6 dissociation in SF_6/N_2, SF_6/O_2, and SF_6/Ne mixtures as a function of electric field-to-gas density ratio, E/N. Another study presents preliminary results obtained from a "three zone" type chemical kinetics model for oxidation of SF_6 in a glow-type corona discharge which accounts for observed oxyfluoride yields when water vapor is present in the gas at trace levels. And finally, the further development of a theoretical model to evaluate the consistency among electron collision cross section, swarm, and dielectric strength data for binary electronegative gas mixtures is included. For the investigation on interfacial phenomena in liquids, results include a description of an image-preserving optical delay (IPOD) together with fast electrical pulse detection to observe correlations between the partial discharge current pulses and development of optically opaque regions near a point electrode. Results of an investigation of the streamer initiation and collapse in hexane under pressure are also detailed. Finally, in the investigation concerned with measurement of high-voltage transients, a detailed evaluation is given of the performance of different free standing dividers for measurement of fast impulses. The focus is on use of step response determination and application of convolution techniques to interpretation of waveforms recorded during transient measurements.

1. INTRODUCTION

Under an Interagency Agreement between the U.S. Department of Energy (DOE) and the NIST, the Electrosystems Division of NIST, has been providing technical support to DOE on a number of tasks concerned with research on electrical energy systems. This document summarizes the technical accomplishments of this program during fiscal year 1987.

Section 2 of this report describes the work in ac electric and magnetic fields and dc field and ion measurements. Section 3 summarizes the work performed under task 3 on the development of the measurement techniques and the accumulation of fundamental data needed for gaseous dielectrics research. Section 4 describes the development of techniques to measure interfacial phenomena in liquids. The final technical project, which deals with the measurement of nanosecond breakdown in power system dielectrics, is summarized in section 5.

2. ELECTRIC FIELD MEASUREMENTS
Task 01

Martin Misakian and William Anderson
Electrosystems Division
National Institute of Standards and Technology

2.1 Introduction

The objectives of this project are to develop methods to evaluate and calibrate instruments which are used, or are being developed, to characterize the electrical parameters in the vicinity of power lines and in laboratory apparatus designed to simulate the power line environment. Electrical measurement support is also provided for DOE-funded efforts to determine if there are biological effects due to ac fields and dc fields with ions.

The electrical parameters of interest include the electric field strength, magnetic flux density, ion current and charge densities, ion mobility and ion species. Recent laboratory studies have focused on the measurement of ion mobilities at atmospheric pressure using drift-tubes; some results of these studies are described in the following sections. In addition, during 1987 the first draft of a new IEEE standard for measuring dc electric fields and ion related quantities was prepared at NIST in collaboration with members of the DC Fields and Ions Working Group. Other activities in 1987 include: the preparation of a chapter (Exposure Systems and Measurements) of a National Council on Radiation Protection and Measurements report on ELF field effects; a site visit to the Battelle Pacific Northwest Laboratories to characterize electrical parameters in several bioeffects exposure systems; and the issuance of the IEEE and the International Electrotechnical Commission standards which provide guidance for measuring power frequency electric and magnetic fields. The final drafts of these standards were prepared at NIST and include the results of NIST studies.

1

2.2 Ion Mobility

The mobility of an ion as it moves through a gas under the influence of a weak electric field is defined as the ratio of the ion drift velocity to the electric field strength. Corrections for pressure and temperature are normally made to obtain a "reduced mobility." The motivation for measuring ion mobilities, within the context of possible bioeffects due to dc power lines, is that mobility values provide, in some cases, a rough measure of ion mass [1,2]. Ideally, the ion species is of interest when considering the possibility of bioeffects due to exposure to ions from dc power lines, but sampling ions at atmospheric pressure with a mass spectrometer is difficult and requires a complex apparatus [3]. Ion mobility spectra can be measured at atmospheric pressure with less complicated instrumentation and ascertaining that the mobility spectra remain unchanged during a bioeffects study may be as important as knowing that the electric field strength or ion current density remain constant. Mobility spectra would also be useful in determining whether an equivalence might exist between bioeffects studies conducted in different laboratories.

Ion mobility can be determined by measuring the time required for an ion to travel a given distance in a known dc electric field. A device that has been used extensively for this measurement is the drift tube. Following earlier studies with a prototype parallel-plate drift tube [4], two cylindrical drift tubes have been fabricated and used for ion mobility measurements in room air ionized by corona. The design of the drift tubes differs from those normally used for mobility measurements in that metal guard rings with insulating spacers and alignment rods have been replaced with an insulating cylinder on which guard rings have been coated. One drift tube is of the pulsed time-of-flight type [5] and the other is an ac time-of-flight device [6]. The guard ring design was used for establishing an approximately uniform electric field for the mobility measurements after earlier attempts to apply a uniform resistive coating to the inside wall of an insulating tube failed.

2.3 Experimental Arrangement

Schematic views of the two cylindrical drift tubes are shown in figure 1. Both drift tubes are fabricated from commercially available "machinable glass" rods that have been bored to form tubes with an inside diameter of 5.65 cm. The inside walls of the tubes are then coated with a commercial conductive ink. After drying, guard rings 1 cm in width (end guard rings are 0.5 cm) are formed by cutting ~0.05 cm wide circular grooves with a lathe. The tubes are fired to make the rings permanent. An approximately uniform electric field is established along the axis of the cylinder by grading the potential of the guard rings using a resistive voltage divider [7].

Figure 1(a) shows a drift tube designed to operate in a pulsed time-of-flight (TOF) mode. Briefly, ions arriving from the right are prevented entry into the drift tube by the shutter (double mesh, 12 wires/cm, 90% transparency) which is biased shut with a small voltage supplied to the outside mesh. The ions are produced in untreated room air by wires in corona, using an apparatus that has been previously described [8]. Ions enter the
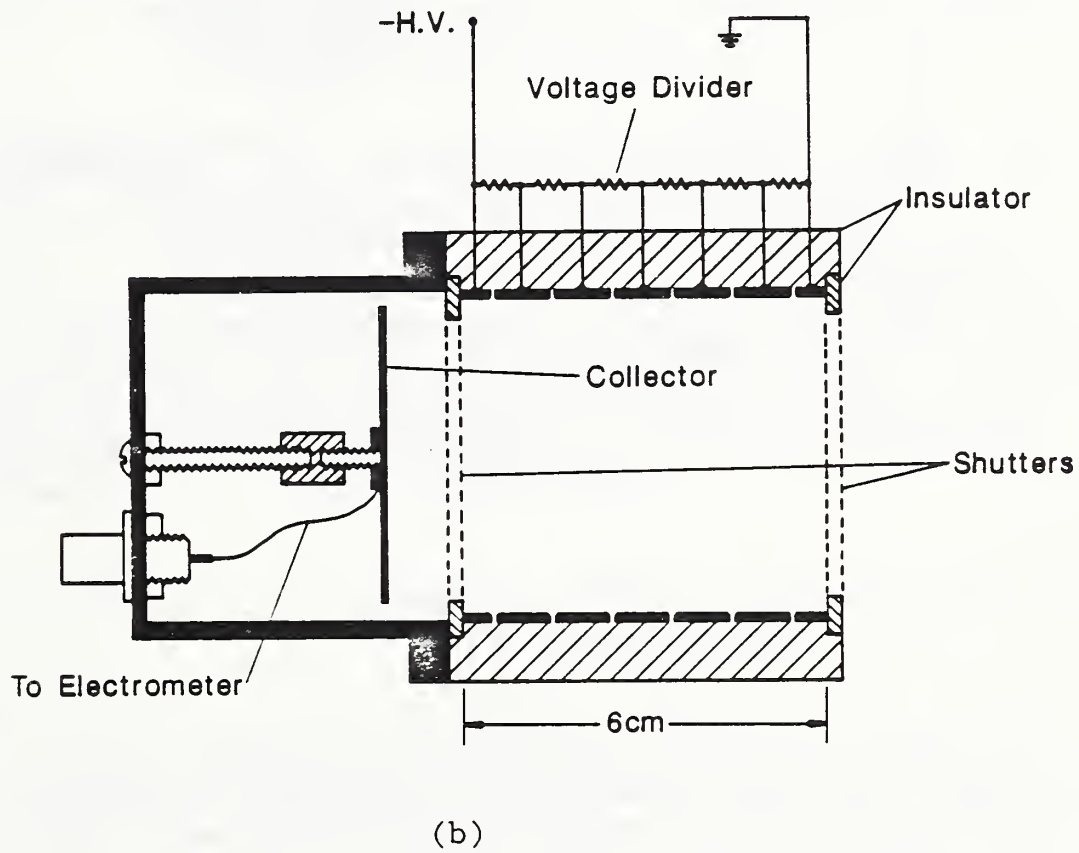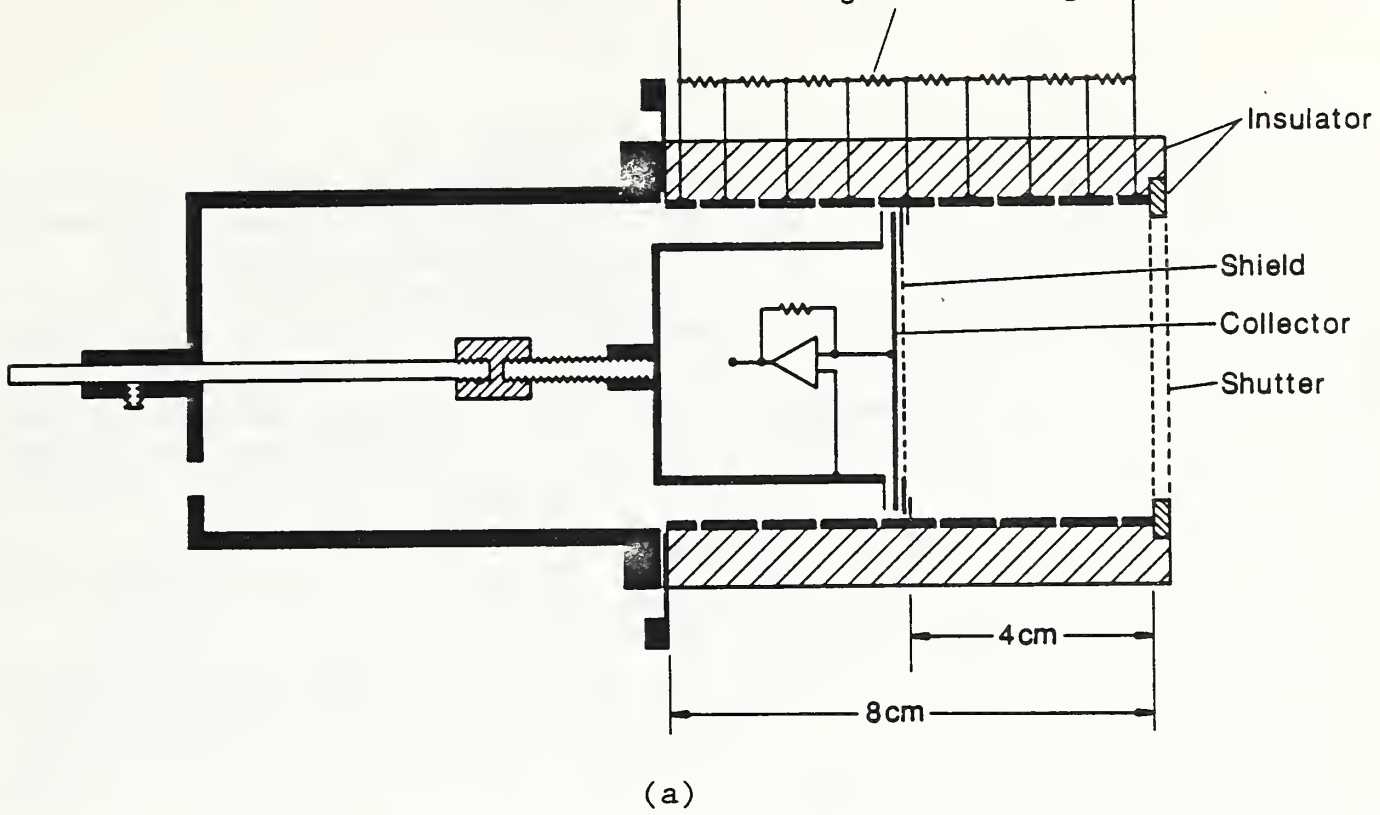
2

Figure 1. Schematic views of drift tubes made of insulating cylinders
and conductive guard rings on inside walls. (a) pulsed time-of-
flight drift tube with movable collector electrode (b) ac time-of-
flight drift tube. The inside diameter of each tube is 5.65 cm.

3

drift tube and travel to the collector after the shutter is pulsed open for a fraction of a millisecond. Because more than one species of ions is present in the approximately disk-shaped volume of ions that passes through the shutter, the ions will separate into groups with the same drift velocity or mobility as they traverse the length of the drift tube. A shield grid (single mesh, 28 wires/cm, 90% transparency) before the collector prevents the induction of current in the collector circuit until the ions pass through the shield grid. The current induced in the collector circuit as the ions travel between the shield and collector is monitored and exhibits maxima and minima as a function of time because of the different time-of-flights of the different ion species. The current induced in the collector is converted to a voltage using a current-to-voltage operational amplifier-circuit. This signal is sampled with a signal averager to obtain a relatively noise-free spectrum. The length of the drift region is variable so that the distance the ions travel can be made nominally 4 cm or 8 cm. By obtaining TOF spectra at two drift distances, it is possible to eliminate so called "end effects" when computing the TOF of a given ion peak.

Figure 2(a) is a block diagram showing the drift tube, signal averager, and pulse generator for gating the shutter. It is noted that the signal averager is emulated, with some cost saving, using a personal computer with a commercially available data acquisition board and software.

Figure 1(b) shows a schematic view of an ac TOF drift tube similar in principle to that employed by Tyndall and Powell [6]. The shutters at each end of the drift tube are biased closed and are opened periodically with sinusoidal voltages applied to the inner mesh of each shutter. Ions that have TOF's between the shutters equal to half the period of the ac voltage will pass through both shutters to yield a steady-state current which is measured with an electrometer. Measurement of ion current as a function of frequency results in current maxima at specific frequencies for ions with different mobilities. The mobility of an ion, K, is given by the expression

$$K = 2L^2F/V, \tag{1}$$

where F is the frequency of the current maximum, L is the length of the drift space and V is the voltage across the drift tube.

Figure 2(b) is a block diagram showing an automated system, under the control of a minicomputer, that is used for obtaining TOF spectra. A programmable function generator provides the sinusoidal voltages to the shutters via small transformers. As the frequency is varied under control of the computer, the current is measured with the electrometer. The values of the frequency and the associated ion current are stored in the computer for later printout.

2.4 Theoretical Time-of-Flight Spectrum

An approximate expression for the pulsed TOF spectrum of a single ion species, appropriate for a cylindrical drift tube, is derived. It is assumed that there are no reactions between the ions and the air molecules in the drift space and there are no fringing field effects at the ends of the drift
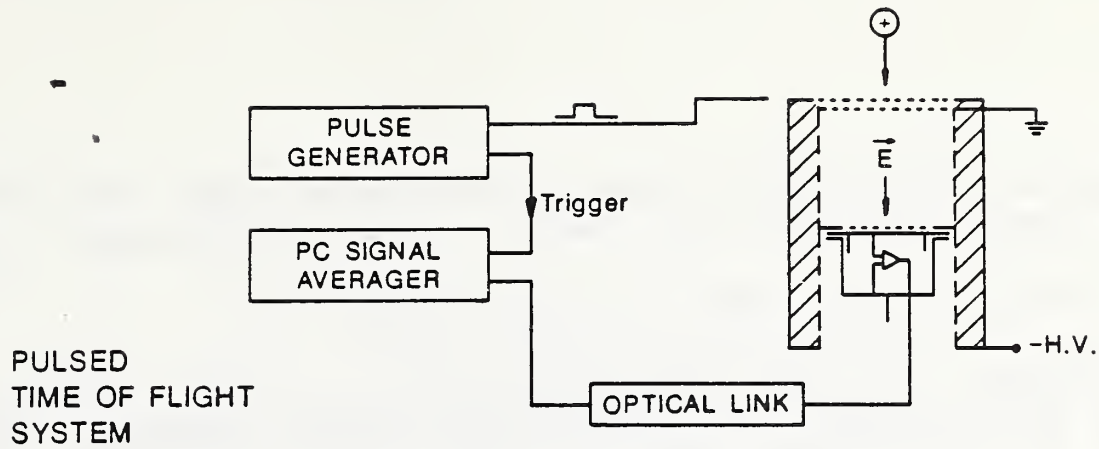
(a)
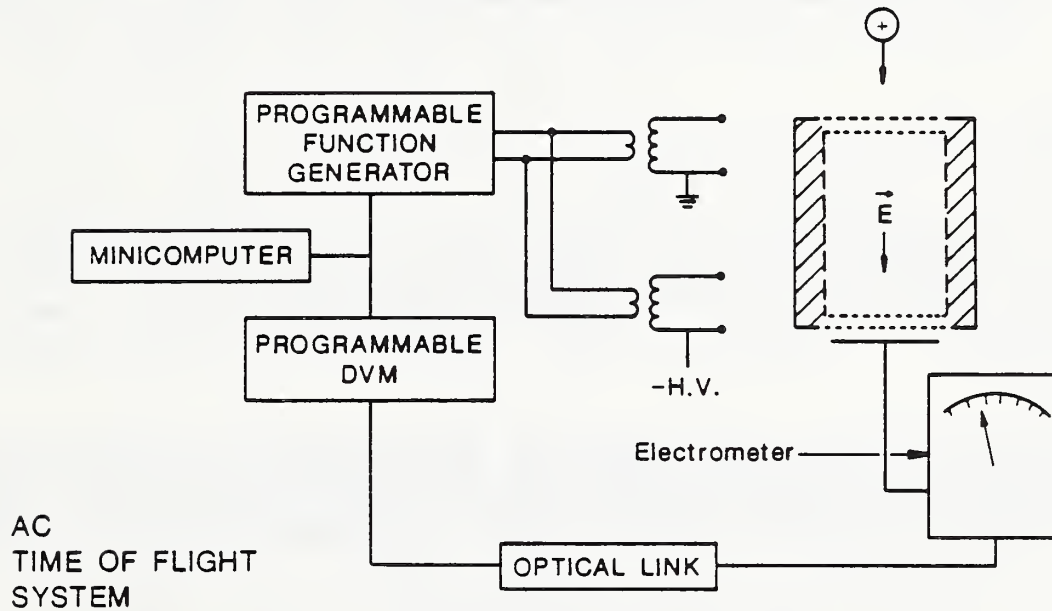
(b)

Figure 2. Block diagrams of pulsed TOF and ac TOF drift tube measurement systems (a) pulsed TOF system includes pulse generator for gating shutter open (normally closed with bias voltage) and signal averager which averages the signal from the drift tube collector circuit (b) ac TOF system includes programmable function generator for producing a sinusoidal voltage under the control of a minicomputer. As the frequency of the gating voltage to the shutter is advanced, ion current values detected with the electrometer are measured and stored in the computer with the corresponding frequencies.

space. Assuming an infinitesimally short shutter pulse width, the diffusion broadened ion current arriving at the shield at time t is given by [5]

$$f(t) = (C/t^{\frac{1}{2}})[v_d + (L/t)] \exp[-(L - v_d t)^2/4D_L t], \qquad (2)$$

where C is a constant, v_d is the ion drift velocity, L is the distance between the shutter and shield meshes and D_L is the longitudinal diffusion coefficient which is given, for our electric field conditions, by the Einstein equation

$$D_L = KkT/e. \qquad (3)$$

In Eq. (3), K is the mobility, k is the Boltzman constant, T is the temperature in degrees Kelvin, and e is the ionic charge. Assuming a rectangularly shaped shutter pulse of width, w, the ion current is increased and the peak of the TOF spectrum is shifted to longer times. The diffusion-broadened, pulse-width-broadened, ion current passing through the shield mesh as a function of time is given by F(t), where [9]

$$F(t)dt = \int_{t-w}^{t} f(t')dt'. \qquad (4)$$

The current, i(t), induced in the collector circuit by the ionic charge as it travels between the shield and the collector is given by [10]

$$i(t) = q(t)v_d'/s, \qquad (5)$$

where q(t) is the ionic charge moving between the shield and collector with drift velocity, v_d'; s is the spacing between shield and collector. The ionic charge, q(t), between the shield and collector is found from integrals of the form

$$q(t) = \int_{t_o}^{t} F(t')dt', \qquad (6)$$

where t_o is the TOF of the ions that first reach and pass through the shield mesh. Because the first ions to pass through the shield mesh will reach the collector at some time, t_c, and be eliminated, and because some ions will still be present in the shield-collector space after the last ions pass through the mesh at time, t_f, the expression for q(t) will change. For

$$t_o \leq t \leq t_c, \quad q(t) = \int_{t_o}^{t} F(t')dt',$$

$$t_c \leq t \leq t_f, \quad q(t) = \int_{t_o}^{t} F(t')dt' - \int_{t_o}^{t_o+(t-t_c)} F(t')dt', \quad (7)$$

$$t \geq t_f, \quad q(t) = \int_{t_o+(t-t_c)}^{t_f} F(t')dt'.$$

Figure 3 shows schematically the positions of $f(t)$, $F(t)$, and $i(t)$ along the time axis with the peak heights of each function normalized to the same value. By choosing trial values of v_d in Eq. (2), fits can be attempted of an experimental TOF spectrum using Eqs. (2)-(7).

As noted above, Eqs. (2) through (7) are obtained assuming that there are no fringing electric field effects at the ends of the drift tube and that the leading and trailing edges of the ion cloud that passes through the shutter coincide with the gating pulse. In addition, it is assumed that Coulomb repulsion between the ions and space charge distortion of the drift field have negligible effect on the TOF spectrum. These assumptions are briefly examined.

When the shutter is pulsed-open, the amplitude of the voltage pulse is chosen to make the electric field in the shutter nearly the same as that in the drift region. This reduces the effect of the fringing fields for a fraction of a millisecond. However, during most of the ion TOF, the drift field near the shutter will be significantly perturbed because there exists an electric field in the shutter that differs in magnitude and direction. A simplified, but conservative two-dimensional model calculation of the perturbed electric field and ion TOF along a path midway between two shutter wires indicates that the trailing edge of the ion cloud which passes through the shutter would have its TOF retarded by about 1.4% for L equal to 4 cm and about 0.7% for L equal to 8 cm for the electric fields in our drift tube. Comparable results are expected for trajectories that will not pass midway between the shutter wires because the longer path length near the wires is compensated for by the stronger electric field and drift velocity. Because the shutter mesh actually consists of crossed wires, the retardation of the trailing edge of the ion cloud should be less.

The effect of fringing electric fields on the drift velocity, as the ions approach the shield, is reduced by making the electric field between the shield and collector the same as in the drift space. A numerical two-dimensional calculation of the perturbed electric field and ion TOF along a path midway between two shield wires indicates that the TOF is increased by less than 0.02% for a path length of 4 cm. The reduction of the drift

7

APPROXIMATE THEORY
FOR PULSED TIME OF FLIGHT DATA:
ONE ION SPECIES
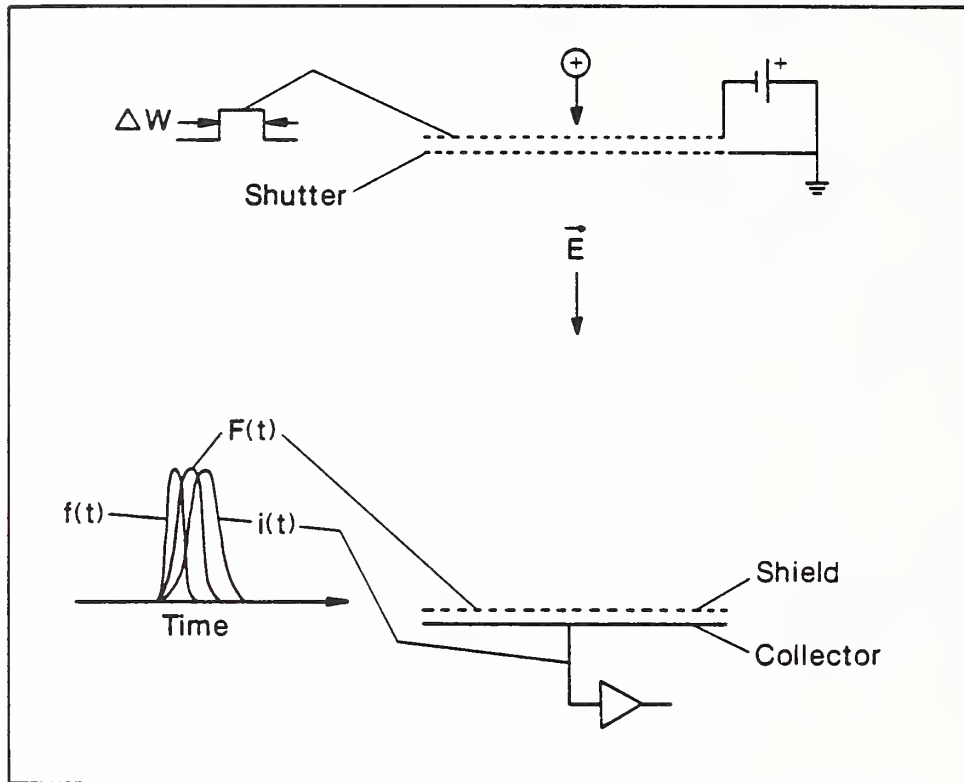
$$f(t) = C_1(v_d + \frac{L}{t}) \exp\left[\frac{-(L-v_d t)^2}{4Dt}\right]$$

$$F(t)dt = \int_{t-\Delta W}^{t} f(t)dt$$

$$i(t) = C_2 q(t)$$

Figure 3. The ion current arriving at the shield mesh as a function of time is described by F(t). The current signal in the collector circuit, i(t), is proportional to the charge moving between the shield and collector. C_1 and C_2 are constants.

velocity should be less for the crossed-wire mesh actually used for the shield.

A parallel-plate apparatus which can produce a known charge density [8] is used to introduce ions into the drift tube. The number density of the ions that enter the drift tube is approximately 2×10^5 ions/cm^3. This density is sufficiently low that the effects of Coulomb repulsion between the ions and space charge distortion of the drift field can be ignored [11].

A theoretical expression for the mobility spectrum obtained with the ac TOF drift tube is not readily developed because the shape of the gating voltage applied to the shutters makes it difficult to characterize the "open" condition compared to the pulse-waveform. Other disadvantages with the sinusoidal waveform for measuring ion mobilities at atmospheric pressure are readily apparent. From Eq. (1), and the typical operating parameters $V = 2.0$ kV, $L = 0.06$ m, $K \simeq 1.5 \times 10^{-4}$ m^2/Vs, F is about 42 Hz. At such low frequencies and for the ac voltage amplitudes required to adequately open the shutters, the duration of the "open" condition can be several milliseconds. The long duration results in a very broad spectrum making it difficult to identify the frequency in Eq. (1). Because more than one ion species is normally present in the spectrum, the long opening of the shutters also results in the loss of resolution of the individual current maxima.

2.5 Experimental Results

Pulse TOF Spectra. Examples of TOF spectra of ions produced by corona in untreated laboratory air are shown in figures 4 through 7. The electric field in the drift space was near 24.8 kV/m in all cases. Figure 4 shows TOF spectra as a function of shutter pulse width and for a drift space of 4 cm. During the first ~0.3 ms, no ions are able to pass through the shutter because their TOF's through the shutter exceeds the pulse width. As the pulse width is increased, the ions with the largest mobility (shortest TOF) appear first. Ions with smaller mobilities can be seen as the pulse width is increased. Thus, depending on pulse width, the shutter can act as a mobility filter, affecting the abundances of the various ion species in the TOF spectrum. In addition, the data indicate that corrections to the axis are necessary because the different ions enter the drift space at different times. For example, about 0.3 ms should be subtracted from the time axis for the fastest ions. The value of w in Eq. (4) should also be adjusted to the effective pulse width. Corrections for the slower ion species cannot be made from the data in figure 4 because the pulse width associated with their first appearance cannot be clearly determined. However, the drift velocities of the different ion peaks can be estimated by obtaining TOF spectra at 4 cm and 8 cm, and dividing the difference in distances by the difference in the corresponding TOF's.

Figure 5 shows positive ion spectra obtained on different days. The data indicate that the number of ion species produced by corona in uncontrolled air, as well as their relative abundances, can vary with time. These results suggest that some attempt be made to control the composition of the air used to produce ions in an animal bioeffects exposure system. In addition, as noted earlier, periodic monitoring of the ion TOF spectrum in a bioeffects

9
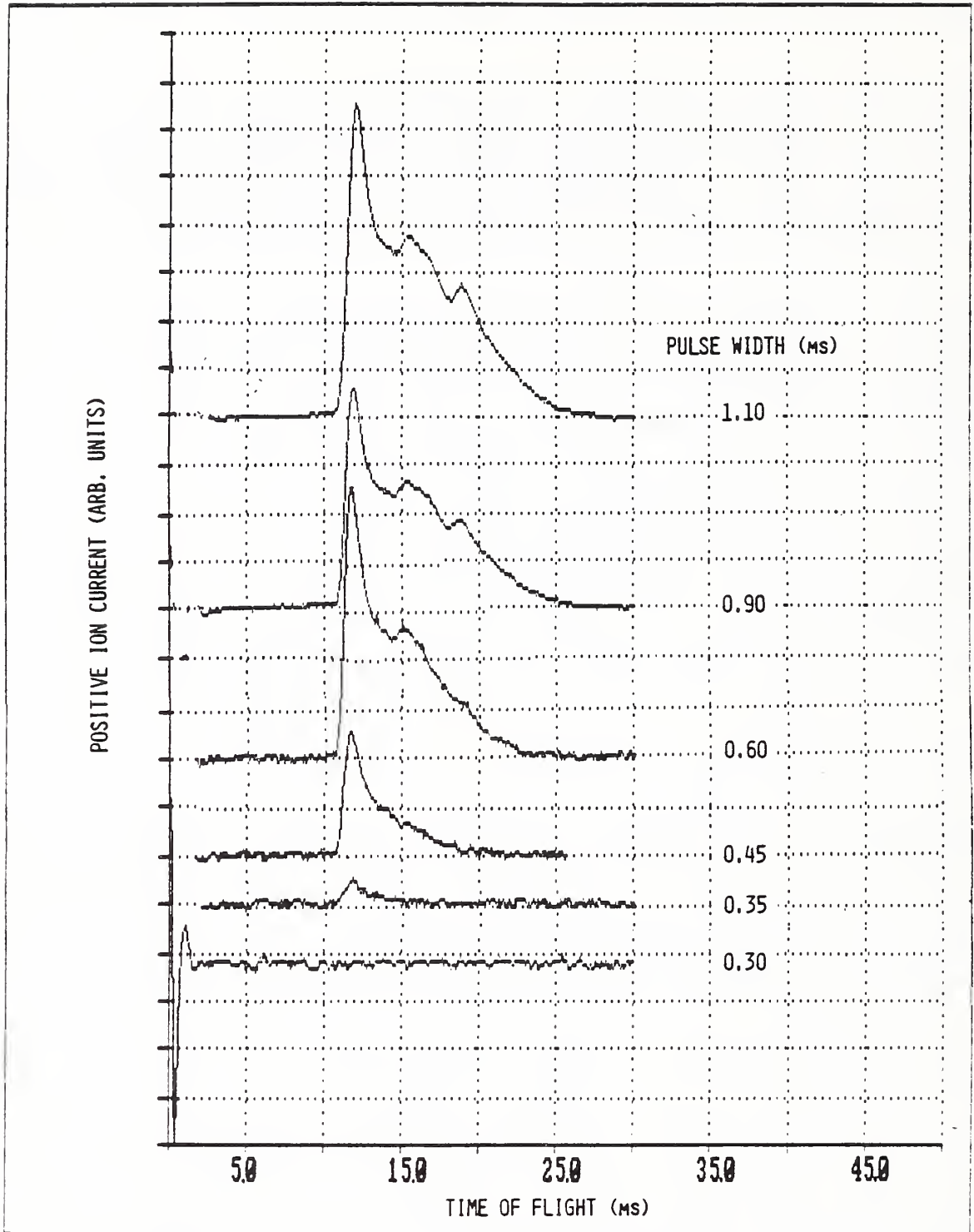
Figure 4. TOF spectra of positive ions as a function shutter pulse width. Ions with small drift velocities fail to clear the shutter until the pulse width is made sufficiently long.
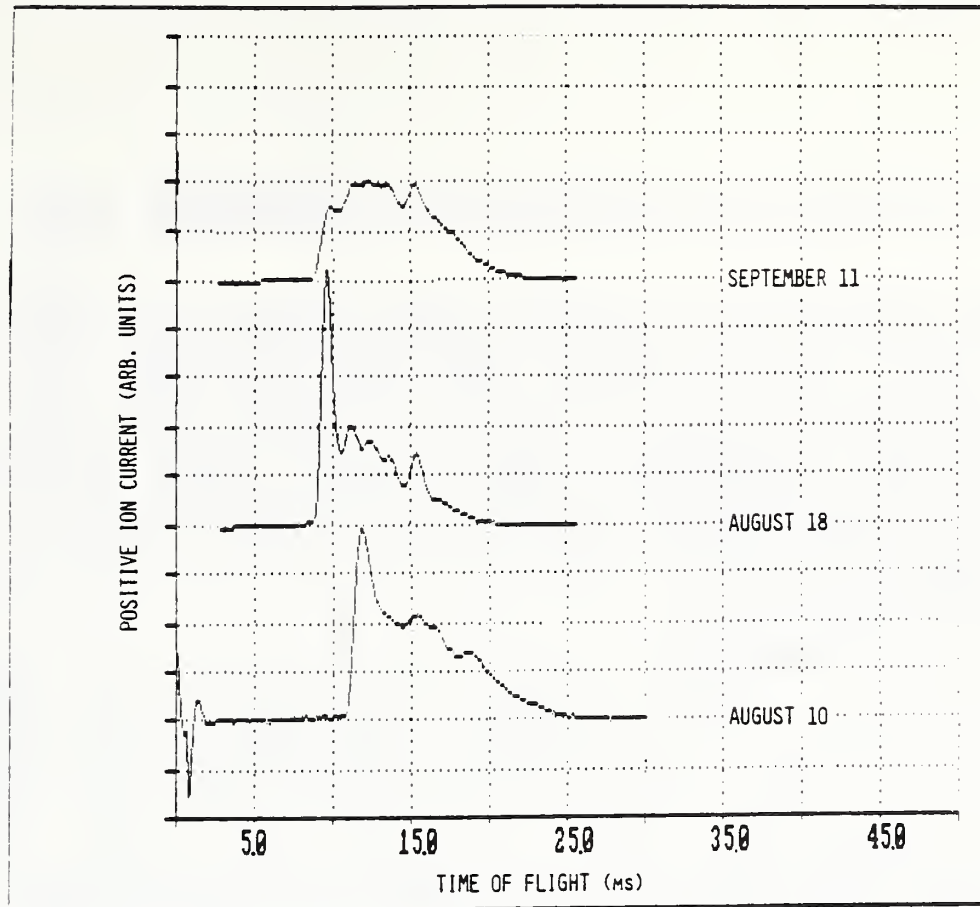
Figure 5. TOF spectra of positive ions measured on different days. The changes in the spectra reflect changes in the air composition.
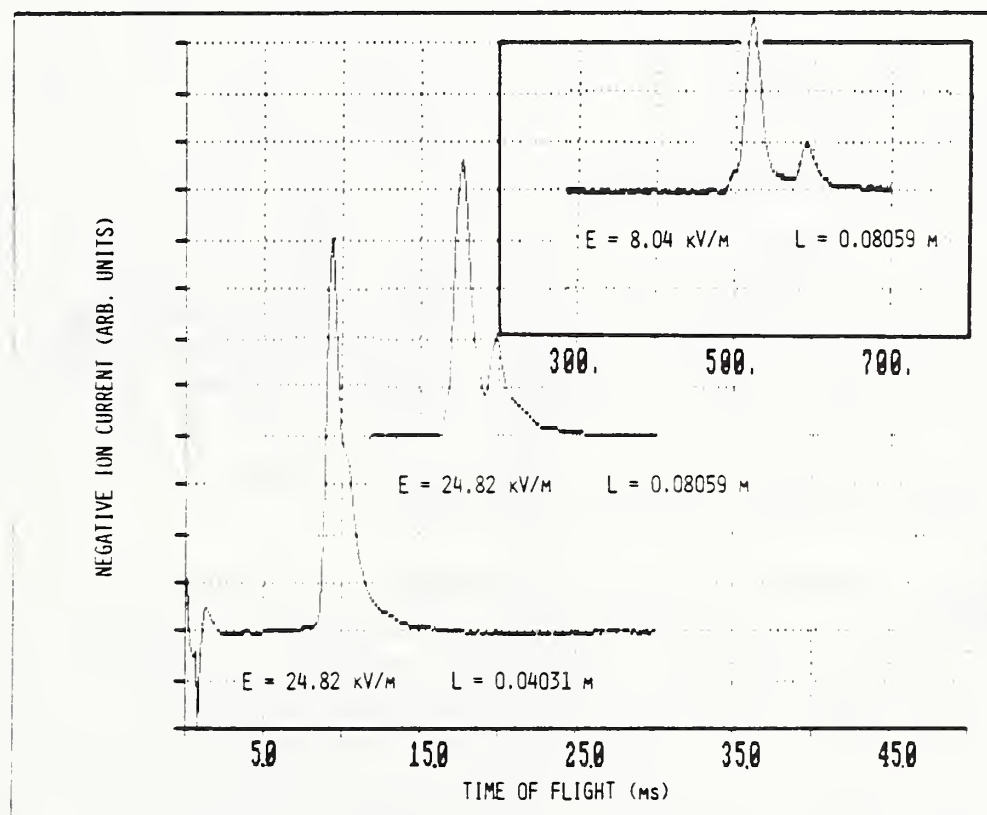
Figure 6. Example of negative TOF spectrum. By increasing the ion time-of-flight, peaks corresponding to ions with different drift velocities are seen.

11

exposure system is necessary to confirm that the composition of the ions has not changed.

Figure 6 shows TOF spectra of negative ions produced by corona in room air. What appears to be two overlapping peaks when the length of the drift tube is 4 cm, is observed to be more than three peaks when the time-of-flight is extended by increasing the length of the drift region and reducing the electric field strength. In addition, the complex and variable spectra in figures 4 through 6 are as expected based on earlier observations of the number of ion species produced by corona in air [12] and the lack of control of the air composition.

Attempts to fit the experimental data using the theory developed earlier have yielded mixed results. Figure 7 shows an experimental fast-peak of a positive ion TOF spectrum for L = 8 cm and the calculated peak taking into account diffusion, pulse-width broadening, and the passage of the ions through the shield-collector region [Eqs. (2) - (7)]. The time axis has been adjusted for delay of the ions passing through the shutter. The theoretical curve is obtained by choosing a drift velocity in Eq. (2) that gives a peak with an onset that should match the experimental one.

When the theoretical drift velocity is compared with that determined by measuring the difference in TOF's for drift distance of nominally 4 and 8 cm, the drift velocity values agree to within about 0.5%. Slightly poorer agreement (difference < 1%) occurs when theoretical drift velocity is calculated for L = 4 cm. It should be noted that drift velocities, determined from the "raw data", i.e. without fitting the data, result in errors of 8% and 4% for measurements at L = 8 cm and L = 4 cm respectively. However, there exists a discrepancy of about 0.3 ms between the theoretical and experimental peak positions in figure 7. Originally it was thought that the experimental peak consisted of two or more closely spaced ion peaks with nearly the same mobility. While there is clearly overlap between adjacent peaks, the good agreement between the theoretical and experimental drift velocities suggests that the 0.3 ms discrepancy may be, in part, an instrumental effect. One possible explanation, which will be checked shortly, is the effects of charging the collector electrode in the drift tube which reduces the electric field in the shield-collector region. This could displace the experimental peak to a longer-time-of-flight as seen in figure 7.

A.C. TOF Spectra. Figure 8 shows an example of a positive ion TOF spectrum obtained with the ac TOF drift tube; the electric field strength in the drift space was near 32.6 kV/m. The inset shows a pulsed TOF spectrum recorded at nearly the same time as the ac data was obtained. As anticipated from the earlier discussion, no structure representing the different ion species can be discerned in the ac TOF spectrum and the mobility value corresponding to the peak ion current is not readily interpreted. Thus, the ac TOF technique for measuring ion mobilities does not appear suitable for obtaining spectra at atmospheric pressure. However, preliminary measurements using a modified ac waveform consisting of pulses of constant width and alternating polarity shows considerable promise for measuring ion mobilities and will be examined in the coming year.
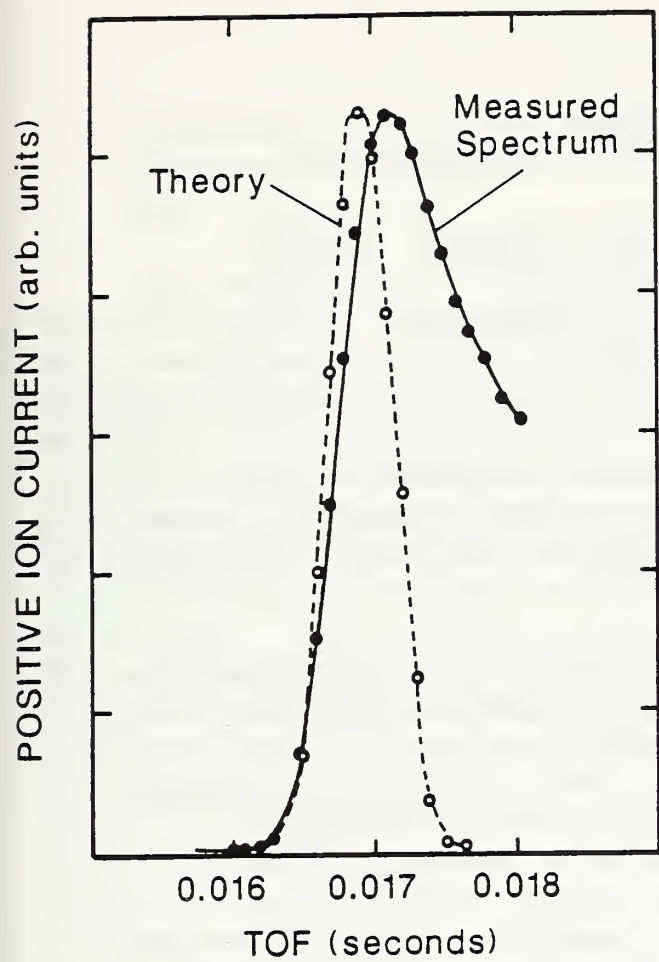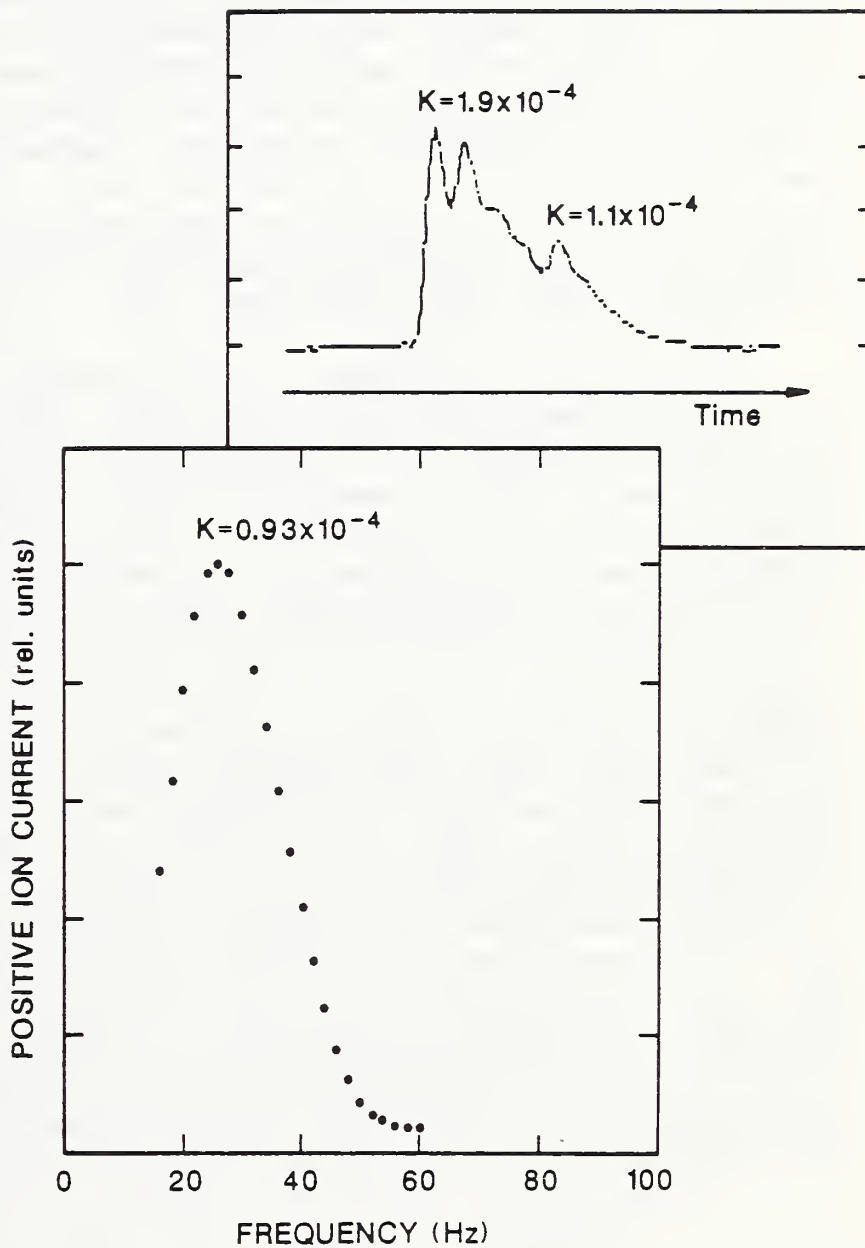
12

Figure 7. Attempt to fit theoretical TOF peak, using eqs.(2)-(7), to experimental peak for L equal to 8 cm. The difference between theory and experiment may indicate an instrumental effect (see text).

Figure 8. AC TOF spectrum for positive ions. Inset shows pulsed TOF spectrum recorded at nearly the same time.

13

3. GASEOUS DIELECTRICS RESEARCH
Task 03

Richard J. Van Brunt, Sanjay V. Kulkarni, and Arthur V. Phelps
Electrosystems Division
National Institute of Standards and Technology

3.1 Introduction

The objectives of this project are the development of measurement capabilities and the providing of fundamental data as part of the Department of Energy's basic research concerned with the development and evaluation of advanced compressed-gas-insulation technology.

To reduce space requirements and improve the efficiency of high-voltage transmission systems, the electric power industry has turned toward more extensive use of compressed-gas insulation. To design meaningful tests of system performance and establish specifications for the quality of materials used in such systems, more information is needed about the fundamental physical and chemical processes which lead to insulation deterioration and electrical breakdown. The research includes applications of gas chromatography-mass spectrometry to characterize corona discharge by-products; and the acquisition of fundamental data, e.g., reaction rate coefficients, corona inception voltages, production rates of corona by-products, the effects of contaminants on discharge initiation, and the rates of discharge-induced decomposition of the gas.

This report highlights four significant technical activities. The first is concerned with the measurements of rate constants for F^- transfer from SF_6^- to fluorinated gases and SO_2 produced by electrical discharges in SF_6. The implications of these processes on ion transport and SF_6 oxidation in corona discharges are also considered. The results have been published during the past year in both conference [13] and archival [14] papers. The second activity concerns the determination of a new "complete" set of electron collision cross sections for SF_6 and the use of these cross sections to compute electron transport, ionization, attachment, and dissociation coefficients in SF_6 and its mixtures with N_2, O_2, and Ne. The results of this work have also been submitted for archival publication [15]. Information acquired from the first two activities were used in the third activity on development of a theoretical, three-zone chemical kinetics model for predicting oxyfluoride production from point-plane glow-type corona discharges in SF_6/H_2O mixtures. Preliminary results of this work were presented in an invited paper at the 5th International Symposium on Gaseous Dielectrics [16]. The fourth activity involved calculation and analysis of dielectric strength data for the binary electronegative gas mixtures SF_6/CO_2, $SF_6/Argon$, $SF_6/Neon$, and $SF_6/Helium$. Information from this activity was presented in two conference papers [17,18]. In this report we provide a brief summary of the more significant findings from these activities.

3.2 Transfer of F⁻ in Collisions of SF_6^- with Fluorinated Gases and SO_2: Temperature Dependence and Implications for Electrical Discharges in SF_6

The reactivity of SF_6^- towards SO_2, SOF_2, SO_2F_2, SOF_4, SF_4, and SiF_4 has been investigated using the technique of pulsed electron beam high-pressure mass spectrometry. These studies were initiated in order to probe the complex anionic chemistry occurring during electrical discharges in SF_6 and to determine the influence of trace level decomposition products upon the identity and reactivity of the negative charge carriers present in the discharge. Although no reaction of any type was observed with SOF_2 and SO_2F_2, efficient F⁻ transfer of the type $SF_6^- + A \rightarrow AF^- + SF_5$ was found to occur in all of the other systems including the $SO_2F^- + SOF_4$ pair, which was studied separately. The reaction of SF_6^- with SO_2 also yields two other products, SF_5^- and $SO_2F_2^-$. With the exception of the $SF_6^- + SiF_4$ reaction, all of the processes exhibited a negative temperature coefficient in that the rate constants for F⁻ transfer decreased substantially with increasing temperature. The reaction $SF_6^- + SiF_4 \rightarrow SiF_5^- + SF_5$ was found to proceed with a rate constant of $5.6 \pm 0.8 \times 10^{-10}$ cm³/s throughout the temperature range studies (298 - 510 K), which corresponds to a collision efficiency of unity. The other transfer reactions were found to approach unit collision efficiency only at reduced temperatures ($\leq$ 300K). Typical results are shown in Fig. 9.

The present data, combined with the existing literature, establish the following F⁻ affinity scale; (F⁻ affinity defined as the energy requirement for the dissociation $AF^- \rightarrow A + F^-$); (SO_2F_2, SOF_2) $< SF_5 < SF_4 < SO_2 < SOF_4 < SiF_4$ suggest an absolute value of 40 ± 3 kcal/mol for the F⁻ affinity of SF_5 which indicates that SF_6^- is reactive towards several of the major stable by-products from electrical discharges in SF_6. This is verified by the data in Fig. 10 showing observed growth and decay of major negative ions from SF_6 previously subjected to a corona discharge. The data shown in this figure correspond to normalized ion intensities observed as a function of time following pulsed ionization at a temperature of 293 K from a sample containing 0.05 mole fraction of corona-decomposed SF_6 in CH_4. Shown in Fig. 11 are similar data from the same decomposed SF_6 sample undiluted in CH_4.

It is obvious from these data that the negative ions SF_5^- and SF_6^- initially produced by electron attachment in SF_6 rapidly react away leaving SiF_5^- and SOF_5^- as terminal negative ions. These ions result predominantly from reactions of SF_6^- with SOF_4 and SiF_4 which are present in the SF_6 at trace levels and result from the decomposition of SF_6 in the discharge [19,20]. The present results are of relevance in any attempt to model negative ion transport in SF_6. They indicate, especially for SF_6^- ions in high-pressure drift tubes or corona discharges, that rapid ion conversion processes involving interactions of SF_6 negative ions with trace contaminants that have higher F⁻ affinities than SF_5^- will convert SF_6^- into other types of charge carriers within a relatively short distance (or time) compared to total drift distances or transit times. We have shown [14], for example, by solving the standard second-order rate equations for F⁻ transfer processes in negative corona-decomposed SF_6 at 200 kPa (2 atm) that 90% of the SF_6^- produced initially in the active corona-discharge region will be replaced by other anions after only 20 μs of transit time.

15
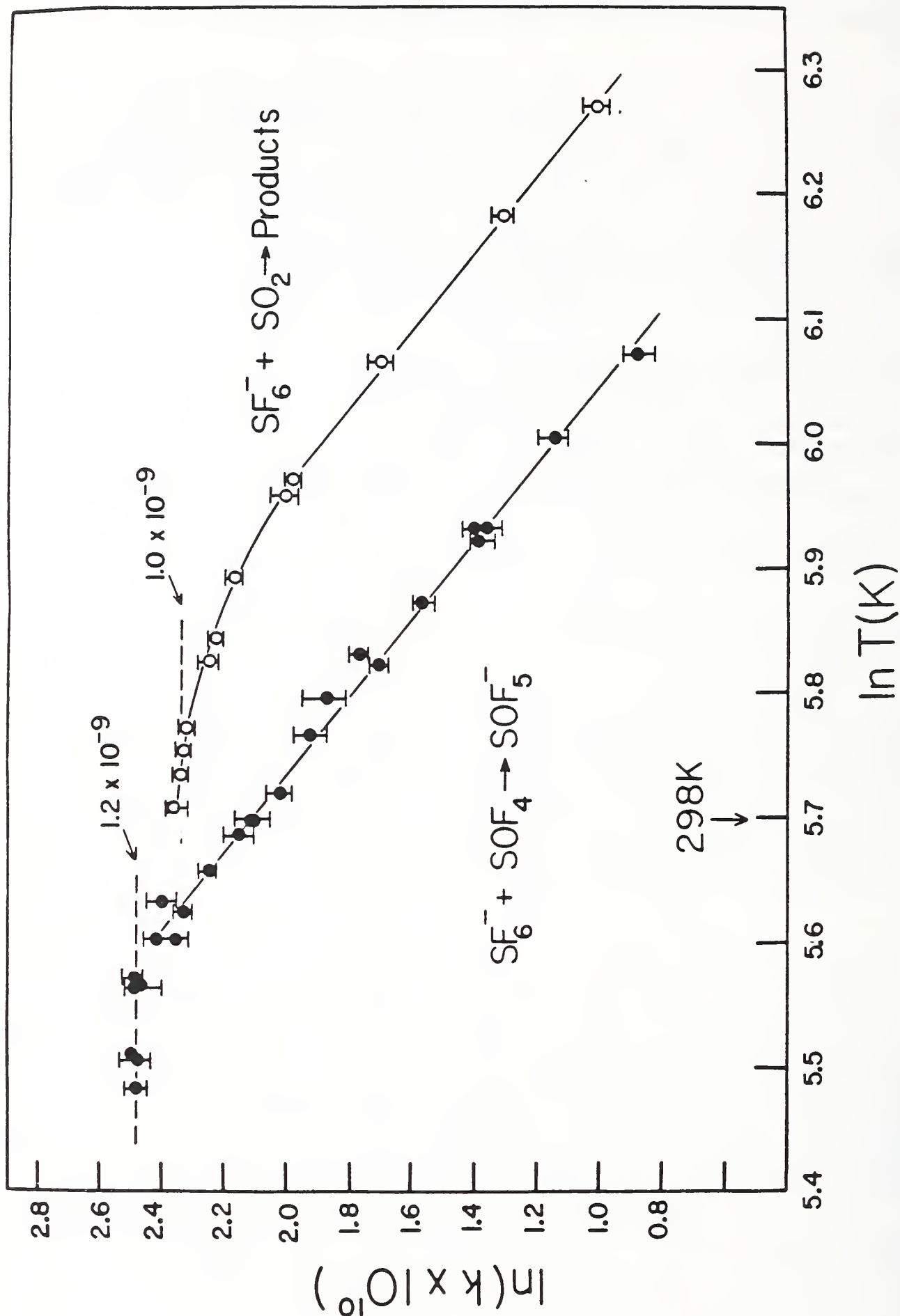
Figure 9. Temperature dependence of rate constants $k(cm^3/s)$ for $SF_6^- + SO_2$ and $SF_6^- + SOF_4$.

16
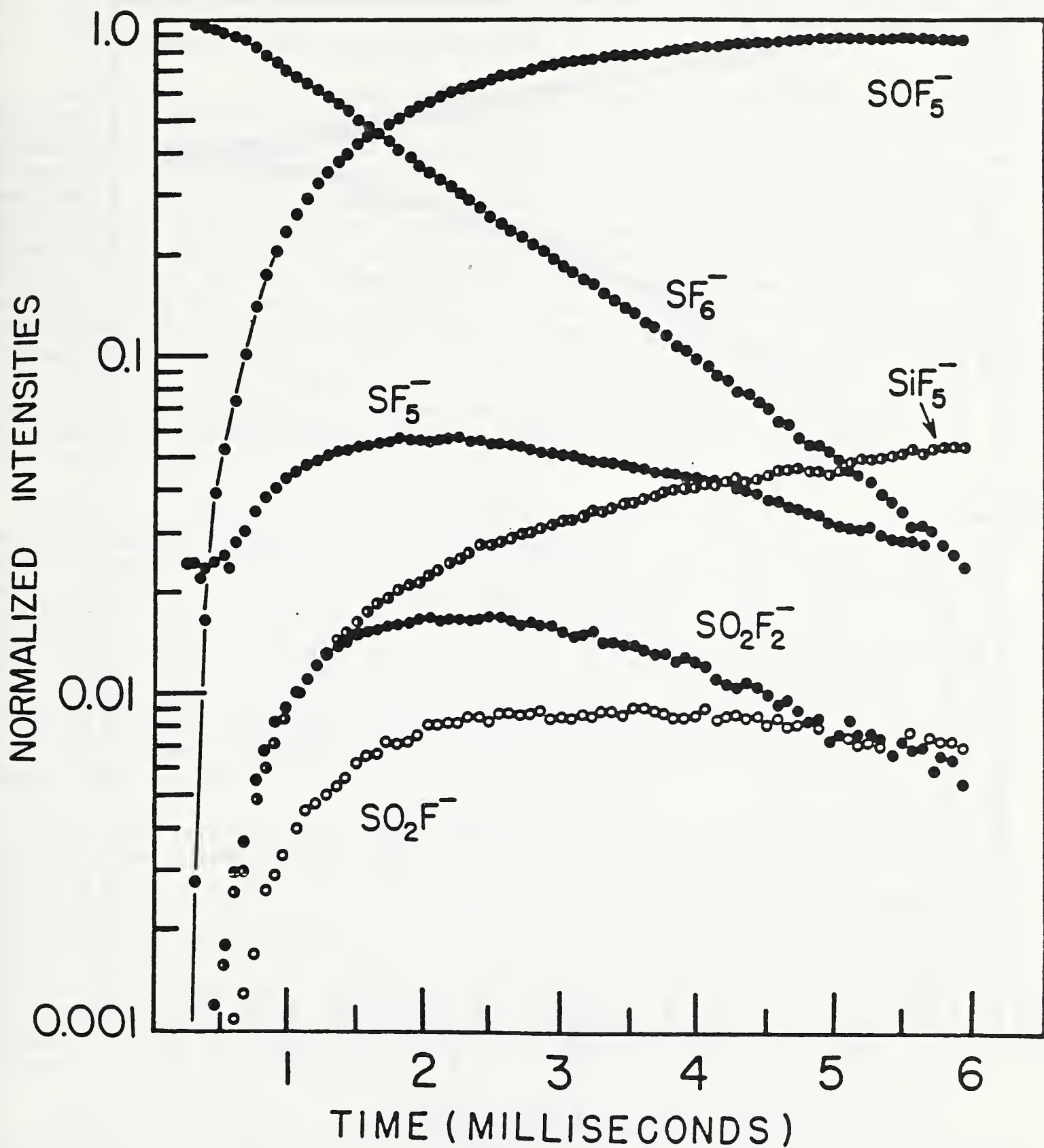
Figure 10. Normalized ion intensities observed as a function of time following
pulsed ionization at 293 K of a sample of 0.05 mole fraction SF_6 in
CH_4 after decomposition of the SF_6 in a negative corona discharge.

17
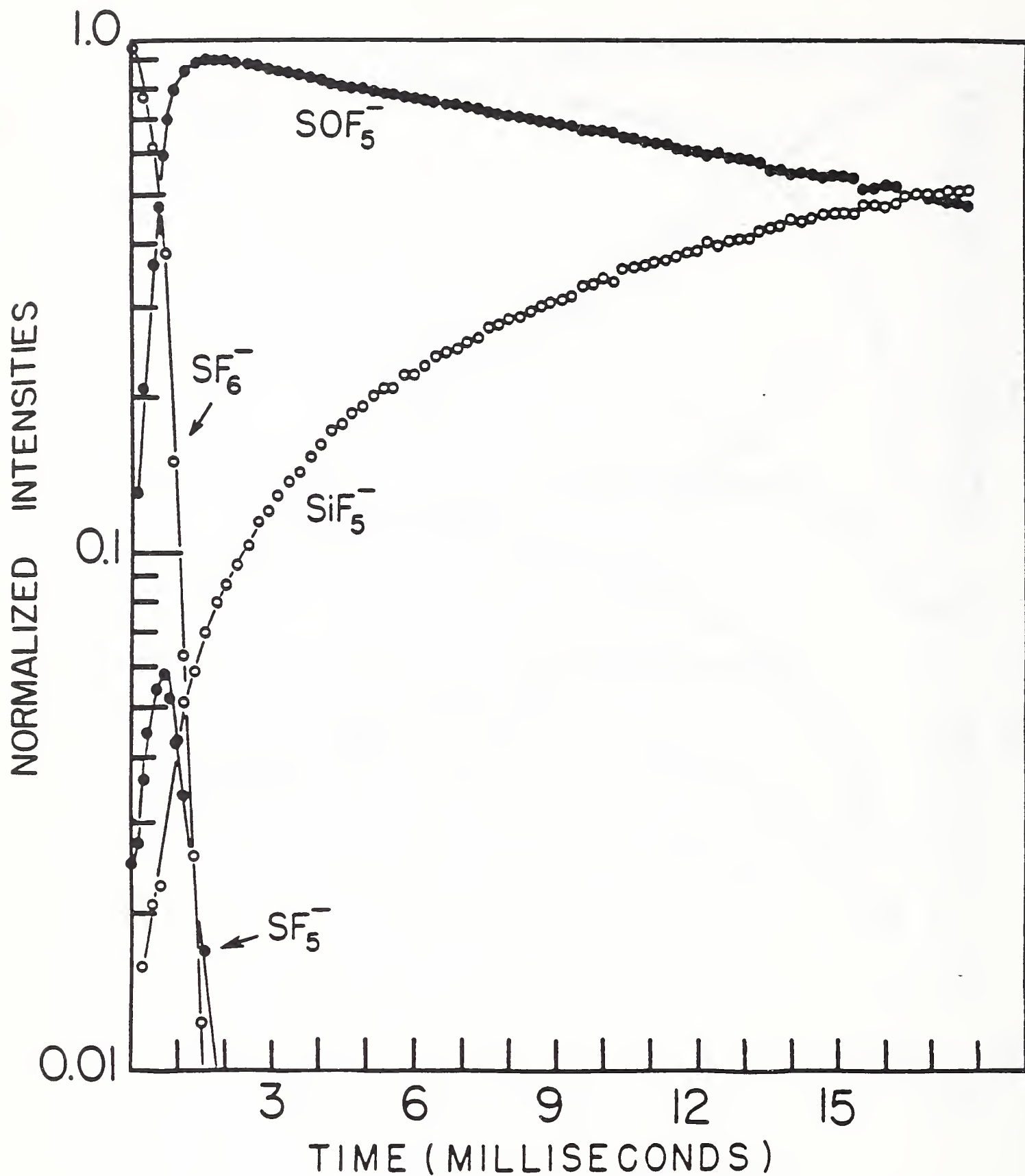
Figure 11. Normalized ion intensities observed as a function of time following pulsed ionization at 293 K of the same sample of SF_6 for which data are shown in Figure 14, but undiluted by CH_4. Pressure is 0.9 Torr.

3.3 Electron Transport, Ionization, Attachment, and Dissociation Coefficients in SF_6 and Its Mixtures

An improved set of electron-collision cross sections was derived for SF_6 and used to calculate transport, ionization, attachment, and dissociation coefficients for pure SF_6 and mixtures of SF_6 with N_2, O_2, and Ne. Our recommended SF_6 cross-section set is shown in Fig. 12 which displays cross sections versus electron energy for momentum transfer, ionization, attachment, and vibrational and electronic excitation. A requirement imposed on the cross-section set was that the electron kinetic-energy distributions obtained as functions of E/N from numerical solutions of the Boltzmann transport equation using this set yield electron transport and ionization and attachment coefficients that are in satisfactory agreement with the data from reliable measurements on both pure SF_6 and its mixtures as shown in Fig. 13. Here E is the electric field strength and N is the gas number density. The transport coefficients of particular interest are the drift velocity (W) and the longitudinal and transverse diffusion coefficients over mobility (D_L/μ and D_T/μ respectively.)

The SF_6 cross sections differ from previously published sets primarily at very low electron energies and at high energies. At energies below 0.03 eV the attachment cross section was adjusted to fit recent data from electron swarm experiments, while the elastic momentum-transfer cross section was increased to the theoretical limit. At high energies, an allowance was made for the excitation of highly excited levels as observed in electron-beam experiments. The individual cross sections agree where possible with directly measured or theoretically calculated cross sections. Where no reliable data were available on the absolute magnitudes of cross sections, they were at least required to be consistent with observed thresholds and energy dependences.

With this cross-section set, electron kinetic-energy distributions were computed from numerical solutions of the electron-transport (Boltzmann) equation using the two-term, spherical harmonic expansion approximation to obtain electron transport and reaction coefficients as functions of E/N and the fractional concentration of SF_6 in the gas mixtures SF_6/N_2, SF_6/O_2, and SF_6/Ne. The critical E/N = $(E/N)_c$ at which the ionization and attachment rates are equal were also determined and compared with various available experimental data. This corresponds to a necessary condition for electrical breakdown in the gas for a uniform electric field and is considered to be a measure of dielectric strength.

The computer code used for solving the electron Boltzmann transport equation for the electron kinetic-energy distributions which were then used to compute transport, swarm, and reaction coefficients is a modified version [21] of that used previously for calculation of temporal ionization coefficients. The code accounts for the gradients resulting from steady-state spatial growth or decay, due to ionization and attachment. In general, any swarm coefficient, α_j/N, corresponding to a process with cross section $Q_j(\epsilon)$, where ϵ is the electron kinetic energy, is computed from the electron kinetic-energy distribution function $f(\epsilon)$ using the relationship

19
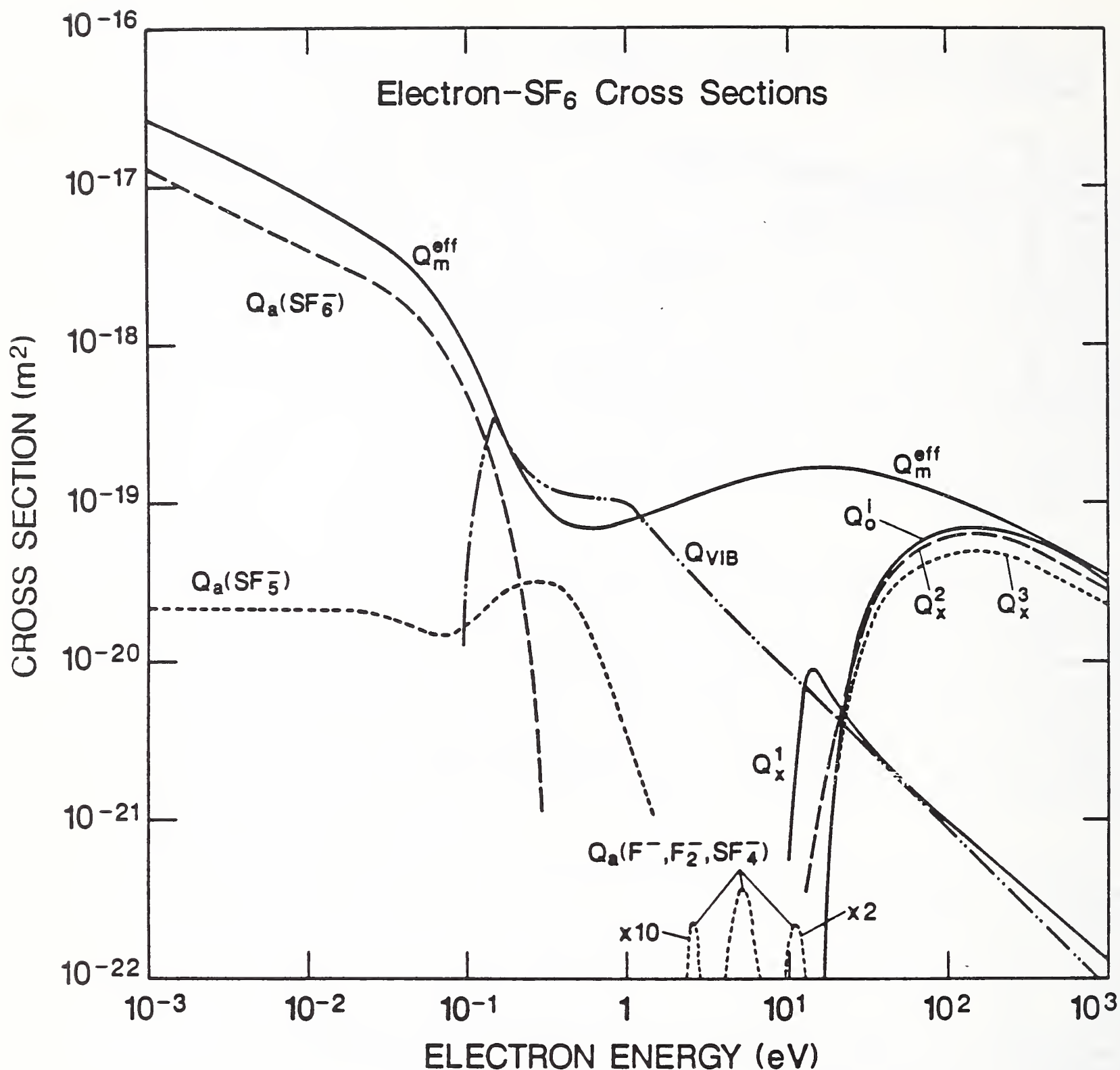
Figure 12. Electron-SF$_6$ collision cross sections versus electron energy. Cross-section symbols are: Q_m^{eff} - effective momentum transfer; $Q_a(SF_6^-)$, $Q_a(SF_5^-)$, and $Q_a(F^-$, F_2^-, $SF_4^-)$ - electron attachment; Q_{VIB} - vibrational excitation; Q_0^i - total ionization; Q_x^j (j = 1,2,3) - electronic excitation.
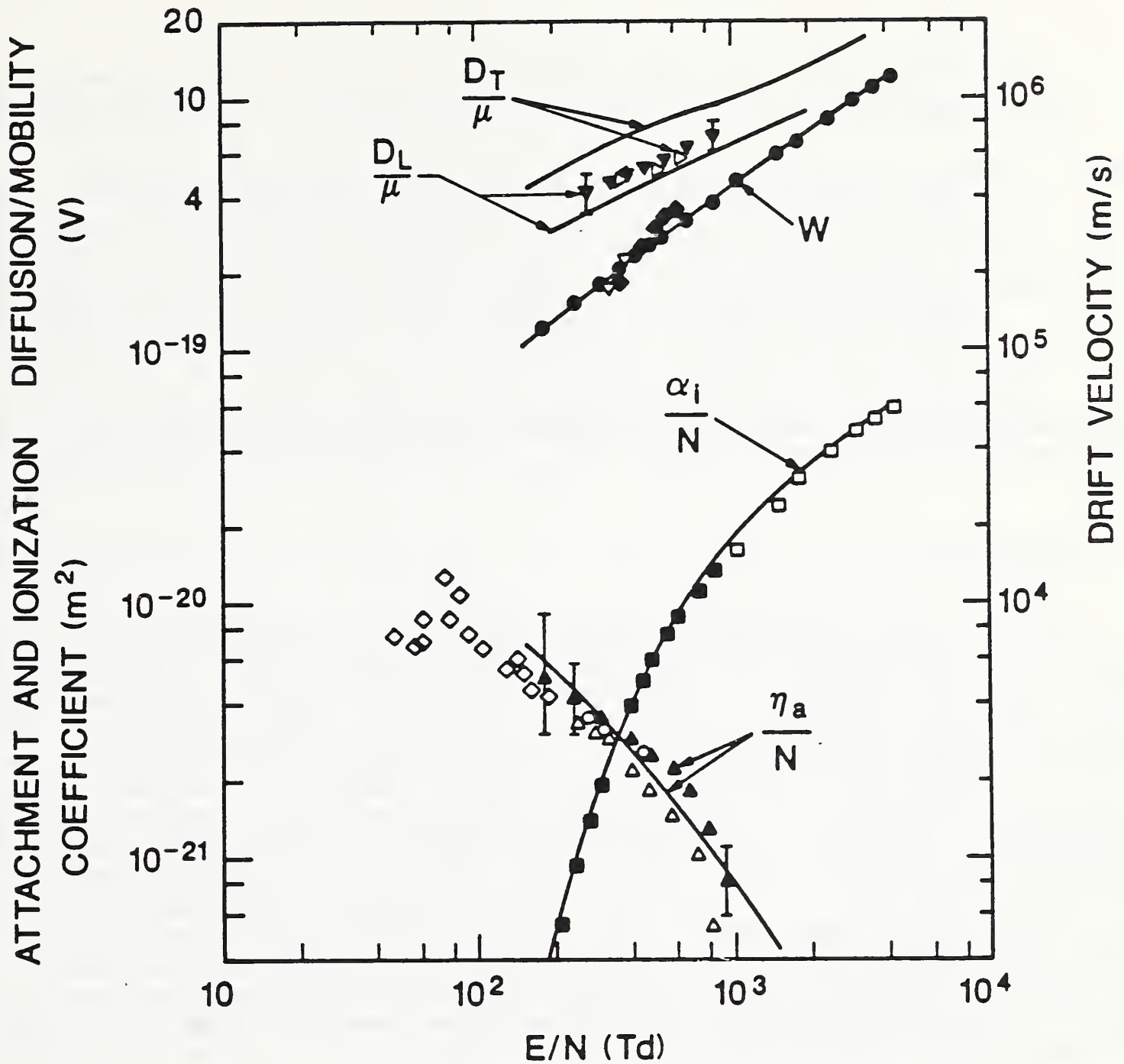
Figure 13. Transport, attachment and ionization coefficients for electrons in pure SF_6. The symbols are: W - drift velocity; D_L/μ and D_T/μ - longitudinal and transverse diffusion coefficients over mobility; α_i/N - ionization coefficient; η_a/N - attachment coefficient. The calculated swarm and transport coefficients are indicated by the solid lines. For comparison we show: results of Aschwanden (Ref. 34) - closed circles (o), closed triangles (Δ), closed squares (◼), and open squares (□) and, closed inverted triangles (▼); data of Siddagangappa et al. (Ref. 48) - open tilted triangles ( ) - data of Verhaart (Ref. 35) - open inverted triangles (∇); data of Naidu and Prasad (Ref. 49) - closed diamonds ( ); data of McAfee (Ref. 50) - open diamonds ( ); data of Hayashi (Ref. 51) - open triangles (Δ) - data of Bhalla and Craggs (Ref. 52) - open circles (o).

21

$$\alpha_j/N = k_j/W \tag{1}$$

where W is the electron drift velocity k_j is a rate coefficient given by

$$k_j = (2/m_e)^{\frac{1}{2}} \int_0^\infty Q_j(\epsilon) f(\epsilon) d\epsilon, \tag{2}$$

and m_e is the electron mass. It is assumed here that $f(\epsilon)$ satisfies the normalization requirement

$$\int_0^\infty f(\epsilon) \epsilon^{\frac{1}{2}} d\epsilon = 1. \tag{3}$$

Shown in Fig. 13 by the solid lines are the calculated ionization coefficient (α_i/N), attachment coefficient ($\eta_a/N = \alpha_a/N$), drift velocity, and longitudinal and transverse diffusion coefficients over mobility for pure SF_6. In the case of pure SF_6, the computer code used to solve the transport equation yielded satisfactory solutions only for E/N greater than 150 Td (1 Td = $10^{-21} Vm^2$). For E/N values below 150 Td, attempts to carry out the iterative determination of the attachment coefficients, i.e., spatial decay coefficients, resulted in oscillatory nonconvergent solutions and/or negative electron energy distributions. We proposed [15] that this failure is due to an inherent limitation of the two-term spherical-harmonic approximation, since this approximation cannot properly account for anisotropies in the electron energy distribution with respect to the electric-field direction for cases like SF_6 where there is a high attachment cross section near zero energy. There are indications that this limitation can be removed by using multi-term representations of the distribution function [22].

The E/N dependence of the SF_6 electron-impact dissociation rate coefficients $k_d(\{Q_x^i\}_j)$, where $\{Q_x^i\}_j$, i = 1,2,3,...j is a particular set of cross sections for dissociative electronic excitation processes, were calculated using:

$$k_d(\{Q_x^i\}_j) = (2/m_e)^{\frac{1}{2}} \sum_{i=1}^{j} \int_{\epsilon_{t,i}}^\infty Q_x^i(\epsilon) f(\epsilon) \epsilon d\epsilon. \tag{4}$$

In this equation $\epsilon_{t,i}$ is the threshold energy for the i th process.

For the calculation of SF_6 dissociation rates, it was assumed, consistent with available experimental data [23], that ionization always leads to dissociation, i.e., SF_5^+ is the largest ion that can be formed. It was also assumed that SF_6 behaves like other large fluorinated molecules for which there is experimental evidence [24] that electronic excitation always leads to dissociation. This assumption is supported by measurements [25,26] of uv and

optical emissions from SF_6 excited by electron impact that show either broad, unstructured emission or a predominance of atomic fluorine emission at energies sufficient for electronic excitation.

The calculated dissociation rate coefficients versus E/N for $\{Q_x^i\}_j$ corresponding to the subsets of cross sections for dissociative attachment,. dissociative ionization, and electronic excitation, as well as the total for all dissociation processes are shown in Fig. 14. Extrapolations of present results indicated by the dashed lines in Fig. 14 are seen to be roughly consistent with the only other known calculation of these rate coefficients by Masek et al. [27] at 100 Td. It is seen from Fig. 14 that in the E/N range of 10^2 to 10^3 Td, the total SF_6 dissociation rate is dominated by electronic excitation processes leading to neutral fragment formation. It is therefore these processes that can be expected to control the rate of SF_6 decomposition in electrical discharges in which $E/N \geq (E/N)_c$ (see Refs 4 and 7).

It is necessary to point out that, both for pure SF_6 and its mixtures, we have neglected the effect of contributions to the gas mixture from products of dissociation or subsequent chemical reactions in obtaining solutions to the Boltzmann transport equation, i.e., the gas decomposition is assumed to be sufficiently small that the products of dissociation do not significantly influence the electron kinetic-energy distribution. It should be cautioned, therefore, that when applying the present results to modelling of chemical processes in electrical discharges, there are cases for which this assumption of constant composition will not be valid, as for example in low-pressure microwave discharges in which most of the gas is dissociated. This assumption should be reasonable, however, for localized high-pressure corona or glow-type discharges [19].

For the mixtures SF_6/O_2, SF_6/N_2, and SF_6/Ne, we show respectively in Figs. 15, 16, and 17 examples of calculated results for the normalized dissociation coefficients $\alpha_d/[X]$ at $(E/N)_c$, where [X] is the concentration of the dissociating molecular species of interest. The corresponding rate coefficients, k_d, can be found using Eq. (1) with the calculated W shown for $E/N = (E/N)_c$ in each case. Also shown in these figures are predicted $(E/N)_c$ values as a function of mixture ratio in comparison where possible with available experimental data. The agreement between the predicted and measured values are seen to be quite good. No measured data for $(E/N)_c$ exist for the SF_6/O_2 mixture.

In the case of SF_6/N_2 mixtures contributions to SF_6 dissociation may occur due to energy transfer in collisions of metastable excited N_2 molecules with SF_6, the maximum effect of these contributions was calculated and is indicated by the curve in Fig. 15 for $[\alpha_d(SF_6) + \alpha_t(N_2)]/NF$, where $\alpha_t(N_2)$ is the sum of the excitation coefficients for the triplet excited states of N_2. It is assumed here that all nitrogen triplet states excited by electron collision are quenched only by dissociative excitation transfer to SF_6. It is known that the lowest $A^3\Sigma_u^+$ metastable state of N_2 is not efficiently quenched by SF_6, although there is evidence that the higher lying $B^3\Pi_g(v = 2)$ state is electronically quenched [28]. Analysis of results for total SF_6 decomposition

23
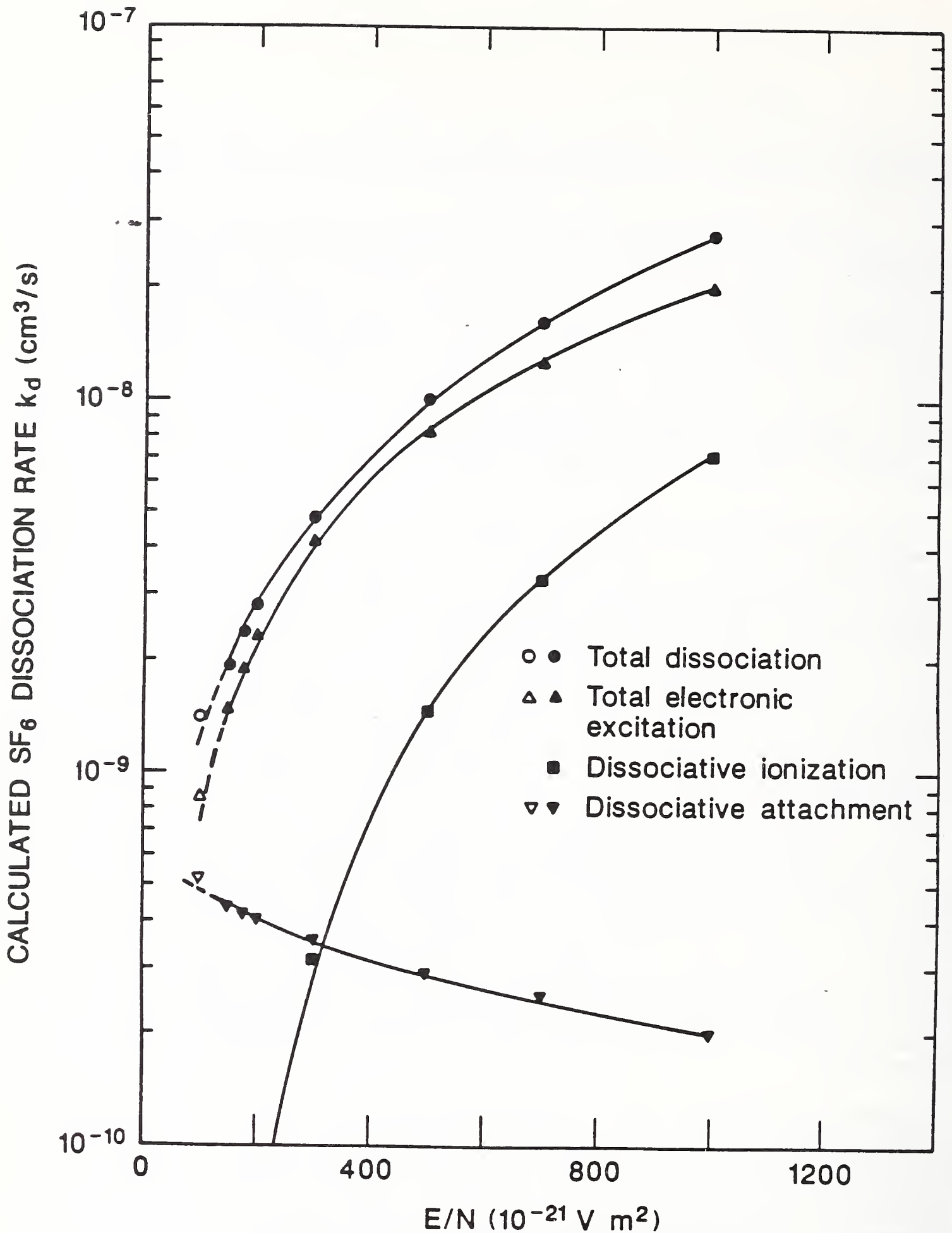
Figure 14. Calculated electron-impact SF_6 dissociation rate coefficients for total dissociation (closed circles - o), total electronic excitation (closed triangles - Δ), total dissociative ionization (closed squares - ▣), and total dissociative attachment (closed inverted triangles -▼) versus E/N in comparison with previous calculation of Masek et al. (Ref. 27) at E/N = 100 Td (open points o, Δ, ▽). The dashed line represents an extrapolation of the present calculated results.

Figure 15. Calculated dissociation coefficients for SF_6 with (dotted curve) and without (solid curve) excitation transfer from N_2 and the drift velocities (dashed curve) at the critical fields, $(E/N)_c$, and $(E/N)_c$ (dot-dashed curve) versus the fractional SF_6 content F in SF_6/N_2 mixtures in comparison with the indicated experimental results of Aschwanden (Ref. 34) and Verhaart (Ref. 35).
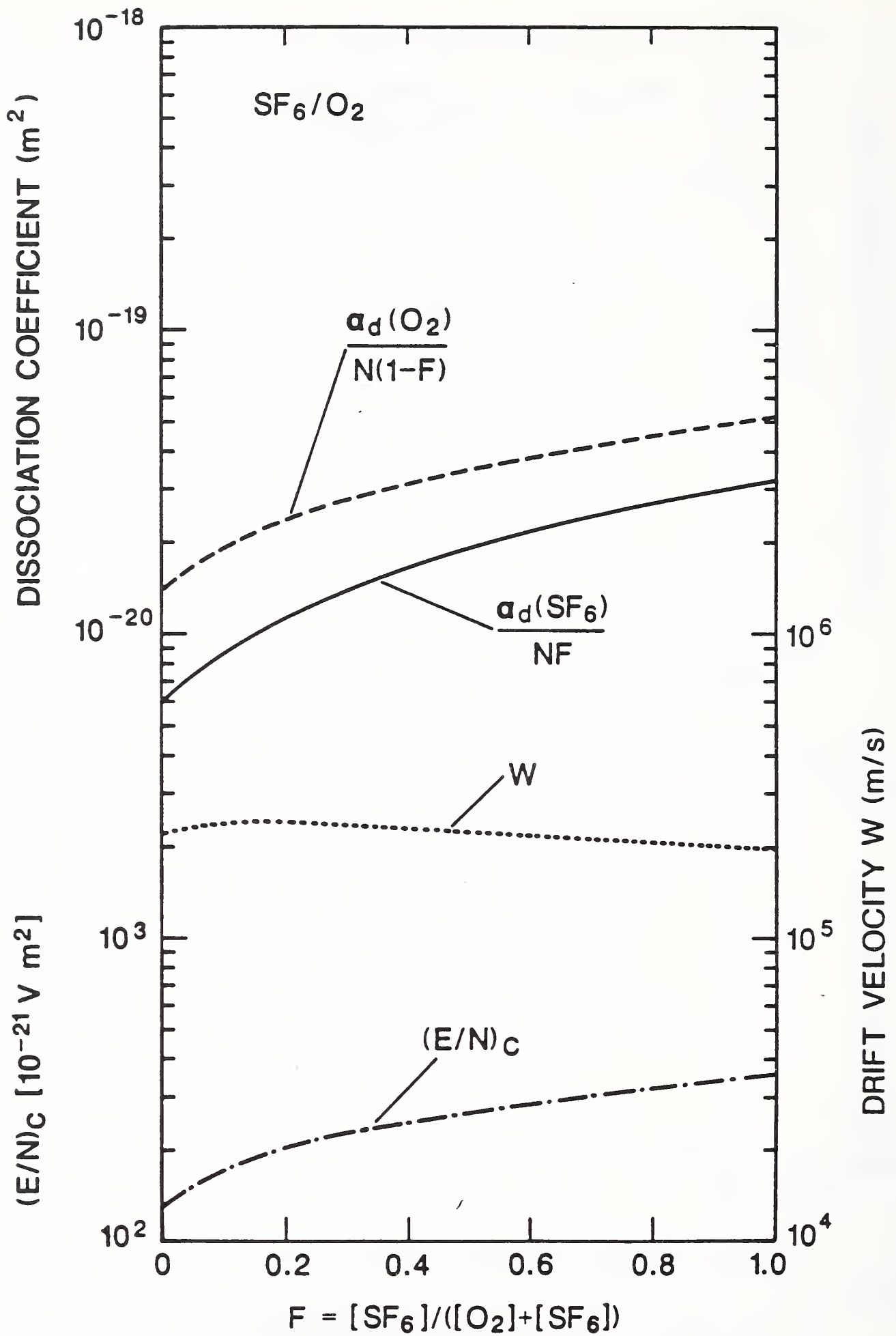
Figure 16. Calculated dissociation coefficients for SF_6 (solid curve) and O_2 (dashed curve) and electron drift velocity (dotted curve) at the critical fields, $(E/N)_c$, and $(E/N)_c$ (dot-dashed curve) versus the fractional SF_6 concentration F in SF_6/O_2 mixtures.

26

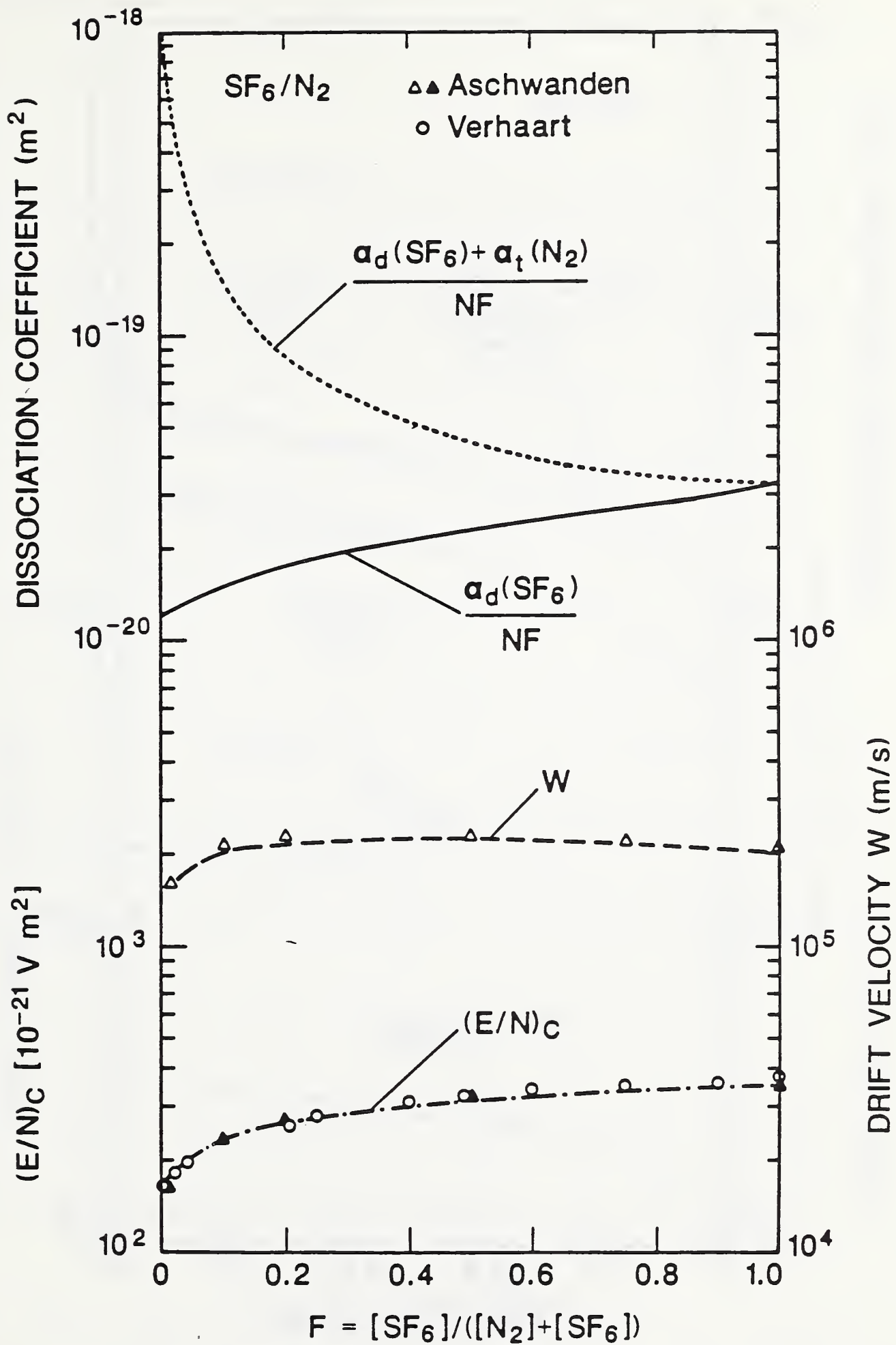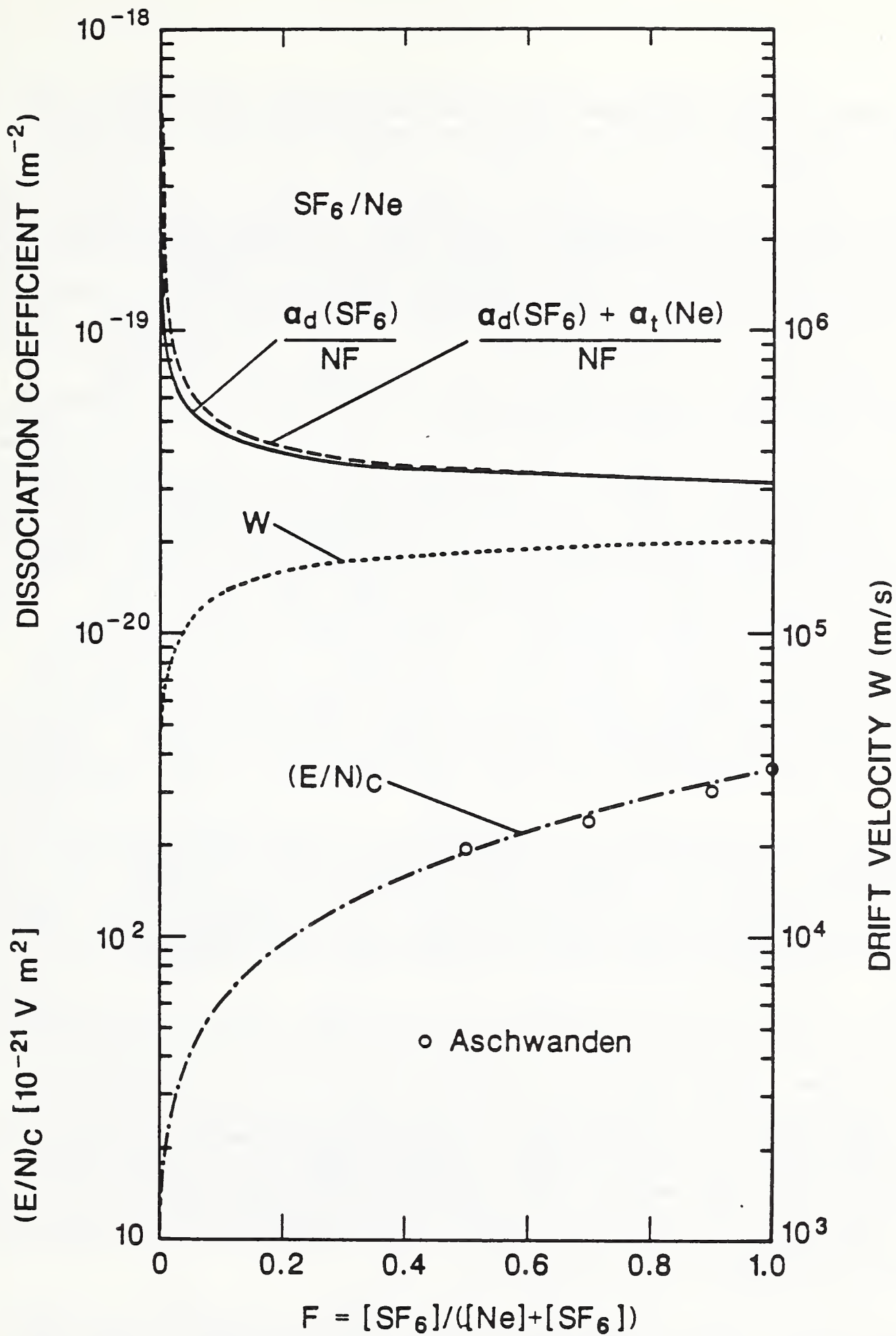Figure 17. Calculated dissociation coefficients for SF₆ with (dashed curve) and without (solid curve) excitation transfer from Ne and electron drift velocities at (E/N)_c and (E/N)_c (dot-dashed curve) versus the fractional SF₆ content F in SF₆/Ne mixtures. The calculated (E/N)_c are compared with the indicated breakdown data of Aschwanden, Ref. 34.

rates in glow-type corona discharges [29] in SF_6/N_2 mixtures also suggest that contributions to SF_6 dissociation by excitation transfer from N_2 is of minor importance.

As in the case of SF_6/N_2, the maximum effect of excitation transfer on SF_6 dissociation for SF_6/Ne mixtures was calculated and is indicated by the upper dashed curve in Fig. 17 corresponding to the quantity $(\alpha_d(SF_6) + \alpha_t(Ne))/NF$ where $\alpha_t(Ne)$ is the sum of the coefficients for excitation to the metastable states of neon. The effect of excitation transfer on SF_6 dissociation is seen to be relatively small for $F > 0.01$. An analysis of experimental observations of the products from SF_6 dissociation in SF_6/Ne mixtures by Siddagangappa et al. [29] shows that the dissociation of SF_6 by collisions with excited Ne cannot be ruled out.

In the case of SF_6/O_2 mixtures the calculation includes the contribution to electron attachment from three-body formation of O_2^- as discussed in Refs 30 and 31. It was found, however, that neglecting this process had no significant effect on the results shown in Fig. 16, except for pure or nearly pure O_2. Three-body attachment is expected to be less significant than dissociative attachment because of its relatively low magnitude and low effective energy range [31,32]. The electron-attachment rate in SF_6/O_2 is dominated by SF_6 for $F > 0.04$. The possible influence of collisional electron detachment from oxygen negative ions has not been included here. There are experimental results, although generally not in good agreement [33], indicating that electron detachment in the interactions of O^-, O_2^-, O_3^-, and O_4^- with O_2 may occur with significant probability at the $(E/N)_c$ values considered here.

In addition to the coefficient for dissociation of SF_6 normalized to F, we also calculated, as shown in Fig. 8, the coefficient for O_2 dissociation normalized to the fractional O_2 concentration, $(1 - F)$. Again, both $\alpha_d(SF_6)/NF$ and $\alpha_d(O_2)/N(1-F)$ apply only at $(E/N)_c$ for each mixture ratio. The O_2 dissociation coefficients are subject to the uncertainties discussed in Ref. 30.

The measured $(E/N)_c$ data for SF_6/N_2 and SF_6/Ne were obtained from Refs 34 and 35, and the drift-velocity data for SF_6/N_2 at $(E/N)_c$ was given in Ref. 34. At the present time no measured results have been obtained on dissociation coefficients for any of the mixtures considered here. It should be noted that the dissociation coefficients, or rates, are essential information in any attempt to theoretically predict the rate of SF_6 decomposition in electrical discharges [16,19,29]. The results from this calculation were used in the model described in the next section to predict the rate of oxyfluoride formation in negative glow-type, point-plane corona discharges in pressurized SF_6 containing trace amounts of water vapor.

The SF_6 cross-section set determined in the present work should be useful in the calculations of $(E/N)_c$ and transport and swarm parameters for other gas mixtures containing SF_6. The dissociation coefficients presented here are the first ever to be calculated for SF_6 and SF_6 mixed with N_2, O_2, and neon.

28

3.4 Zonal Model for Corona-Induced Decomposition of Dielectric Gases

A three-zone model for chemical decomposition of electronegative gases in negative point-plane corona discharges was proposed [16] and shown to be useful in predicting discharge by-product yields and the dependences of these yields on discharge current and gas mixture composition. The principal assumption of this model is that the gas in which a highly localized negative corona occurs can be partitioned into three zones of differing chemical activity, namely the glow region, ion-drift region, and main gas volume as depicted in Fig. 18.

The glow region corresponds to the relatively small volume which is observed [29] to be of approximate uniform luminosity near the tip of the point electrode. It is assumed to be the region of greatest chemical activity in which the mean electric field-to-gas density ratio, E/N, is approximately equal to, or slightly exceeds the critical value $(E/N)_c$ at which the electron-impact ionization and attachment rates are equal. This assumption is justified by recent measurements performed in similar constricted glow-type discharges in SF_6 [36]. Consistent with optical observations [29], the glow region is also assumed to be spherical of radius R and volume τ_c, where τ_c is much smaller than the main gas volume τ_t; typically $t_c/\tau_t < 10^{-9}$.

The chemistry in the glow is dominated by fast reactions primarily involving free radials or ions produced directly or indirectly by electron collisions. The rate constants for bimolecular reactions are required to be in excess of about 10^{-15} cm^3/s in order that the processes in the glow can go to completion, i.e., the reaction times are short compared to times required for molecular diffusion out of τ_c. Dissociation of the gas by electron collisions is also confined to τ_c, since for r > R, the energetic electrons needed to initiate gas decomposition rapidly thermalize and are removed by attachment. Also, consistent with observations [19], the rate-controlling processes for gas decomposition in the glow are the electron-impact dissociation processes, the rates for which were calculated by the method discussed in the previous section. Table 1 lists the reactions and corresponding rates that were used in the model for the glow region. The rate constants for the various bimolecular processes involving free radicals were derived from several sources [37-39].

The ion-drift region is the interelectrode region in which charge is predominantly carried by negative ions and the chemistry is dominated by ion-molecule reactions of the type considered above in Sec. 3.2. The reactions that occur in this zone can be important in influencing the yields of some gaseous by-products observed from discharge-induced decomposition. The present model considers, for example, the F^- transfer reaction [14,20]

$$SF_6^- + SOF_4 \xrightarrow{k_1} SOF_5^- + SF_5, \quad k_1 = 2.0 \times 10^{-10} \text{cm}^3/\text{s} \tag{5}$$
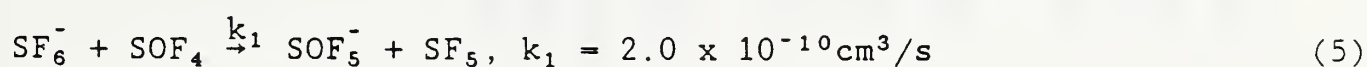
in predicting the rate for SOF_4 production. There is evidence [20] that in many cases this is the predominant SOF_4 destruction mechanism. Given here is

29

GLOW REGION

$SF_5 + O \longrightarrow SOF_4 + F$
$SF_4 + O \longrightarrow SOF_4$
$SF_5 + OH \longrightarrow SOF_4 + HF$

ION DRIFT REGION

$SF_6^- + SO_2 \longrightarrow$ Products
$SF_6^- + SOF_4 \longrightarrow SOF_5^- + SF_5$
$O_2^- + S \longrightarrow O_2 + S^-$

MAIN GAS VOLUME

$SF_4 + H_2O \longrightarrow SOF_2 + 2HF$
$SF_2 + O_2 \longrightarrow SO_2F_2$
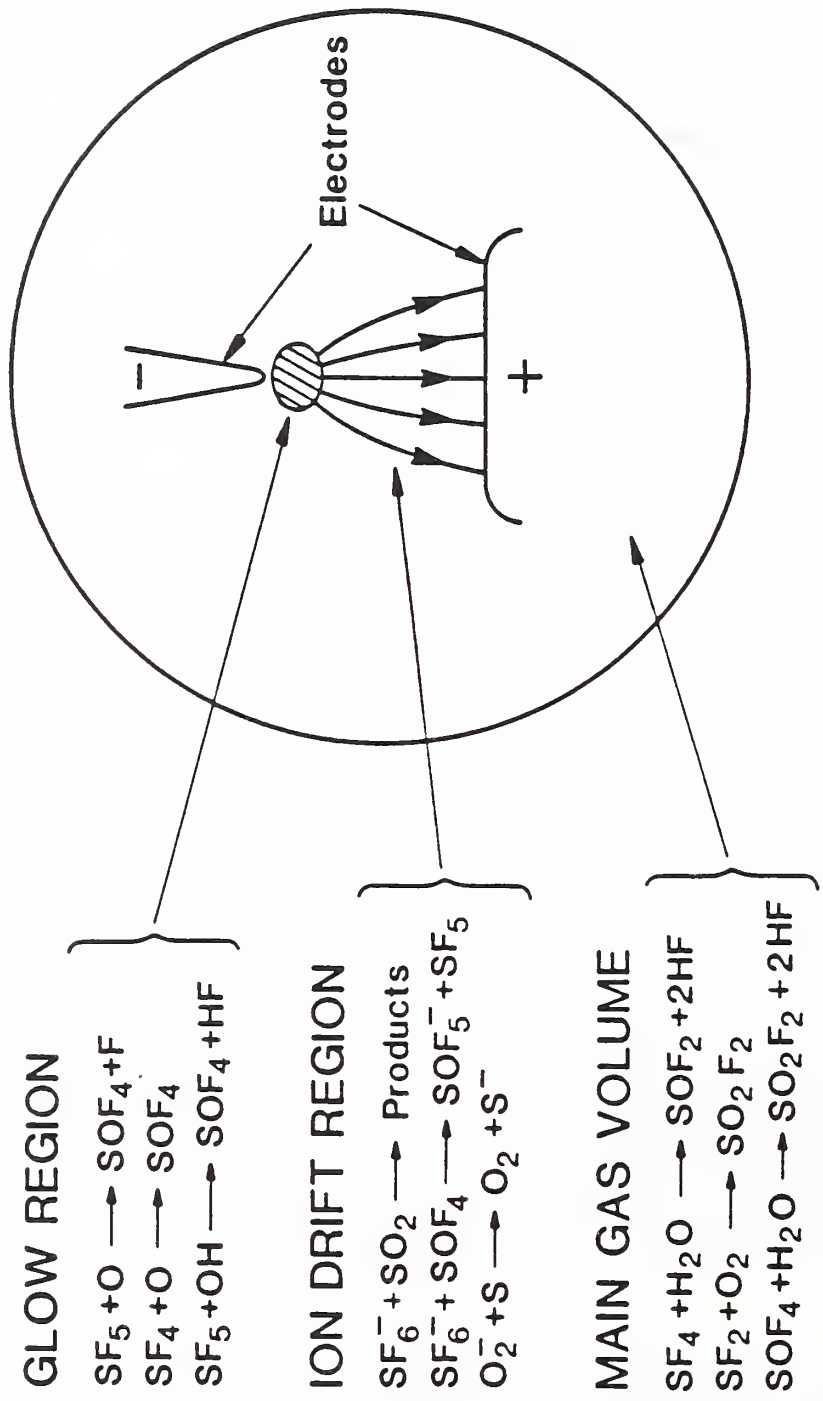$SOF_4 + H_2O \longrightarrow SO_2F_2 + 2HF$

Figure 18. Regions of differing chemical activity associated with the three zone model for SF_6 decomposition in negative, point-plane corona.
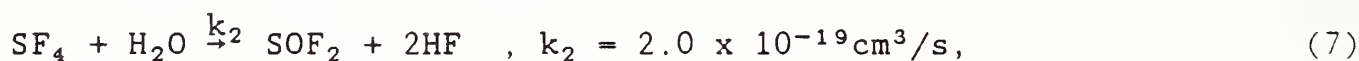
30

Table 1.   Proposed Reaction Scheme for Glow Region

18	$e + SF_6 \rightarrow SF_5 + F + e$	
19	$e + SF_6 \rightarrow SF_4 + 2F + e$	$k_{18} = 2.4 \times 10^2 \ 1/s$
20	$e + H_2O \rightarrow H + OH + e$	$k_{19} = 1.9 \ 1/s$
21	$SF_5 + SF_5 \rightarrow SF_4 + SF_6$	$k_{20} = 5.0 \times 10^2 \ 1/s$
22	$SF_5 + SF_5 \rightarrow S_2F_{10}$	$k_{21} = 5.0 \times 10^{-13} \ cm^3/s$
23	$SF_5 + F \rightarrow SF_6$	$k_{22} = 1.0 \times 10^{-12} \ cm^3/s$
24	$F + F \rightarrow F_2$	$k_{23} = 2.0 \times 10^{-10} \ cm^3/s$
25	$F + H_2O \rightarrow OH + HF$	$k_{24} = 2.0 \times 10^{-16} \ cm^3/s$
26	$SF_4 + OH \rightarrow SOF_3 + HF$	$k_{25} = 1.1 \times 10^{-11} \ cm^3/s$
27	$F + SOF_3 \rightarrow SOF_4$	$k_{26} = 3.6 \times 10^{-13} \ cm^3/s$
28	$F + H \rightarrow HF$	$k_{27} = 2.0 \times 10^{-11} \ cm^3/s$
29	$SOF_3 + OH \rightarrow SO_2F_2 + HF$	$k_{28} = 1.0 \times 10^{-13} \ cm^3/s$
30	$H + H \rightarrow H_2$	$k_{29} = 1.0 \times 10^{-15} \ cm^3/s$
31	$OH + OH \rightarrow H_2O + O$	$k_{30} = 1.0 \times 10^{-15} \ cm^3/s$
32	$OH + F \rightarrow FOH$	$k_{31} = 2.0 \times 10^{-12} \ cm^3/s$
33	$OH + SF_5 \rightarrow SOF_4 + HF$	$k_{32} = 5.0 \times 10^{-13} \ cm^3/s$
34	$OH + O \rightarrow O_2 + H$	$k_{33} = 1.6 \times 10^{-12} \ cm^3/s$
35	$O + SF_5 \rightarrow SOF_4 + F$	$k_{34} = 3.3 \times 10^{-11} \ cm^3/s$
36	$H + OH \rightarrow H_2O$	$k_{35} = 2.0 \times 10^{-11} \ cm^3/s$
		$k_{36} = 5.0 \times 10^{-13} \ cm^3/s$

the thermal value for the rate constant k_1 that applies at low E/N. The rate equation for SOF_4 production that includes the effect of reaction (5) can be written as
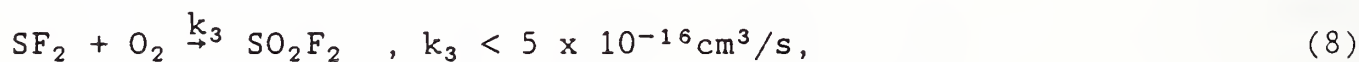
$$\frac{d[SOF_4]}{dt} = r_t - \frac{ik_1[SOF_4]}{e\bar{v}r_t} \left[\frac{\exp\{(-k_1[SOF_4]/\bar{v} - k')Z_0\} - 1}{(k_1[SOF_4]/\bar{v} - k')}\right], \qquad (6)$$

where i is the discharge current, e is the electronic charge, $\bar{v}$ is the mean drift velocity of SF_6^-, Z_0 is the distance between r_c and the anode, r_t is the production rate for SOF_4 within r_c, and k' is a decay constant for a competing SF_6^- deactivation process that can also occur in the ion-drift zone. For the purposes of the present discussion, it is sufficient to note that at t = 0, $d[SOF_4]/dt$ is initially given by r_t, and after a sufficiently long time it approaches a lower constant value of $r_t - i/er_t$ that represents the limit where all SF_6^- is destroyed by reaction (5). This latter condition is likely to be reached for the experimental situations considered here.

The main gas volume is a region of slow chemistry involving relatively stable species like SF_4 and SF_2 that diffuse out of the glow region and undergo slow reactions on the walls of the gas-containing vessel or with gas-phase contaminants like O_2 and H_2O. It will be assumed here for convenience that the vessel which defines r_t is a sphere centered at r_c with a radius R_w, where $R_w \gg R$. It has been shown by Van Brunt and Siddagangappa [20] from mass spectrometric measurements made using the mixture $SF_6/O_2/H_2O$ enriched with either $^{18}O_2$ or $H_2^{18}O$, that SOF_2 and SO_2F_2 are formed from negative corona preferentially by reactions involving H_2O and O_2 respectively. The relative insensitivity of SOF_2 and SO_2F_2 yields to $[H_2O]$ and $[O_2]$ suggest that these products are predominantly formed by the slow gas-phase reactions

$$SF_4 + H_2O \xrightarrow{k_2} SOF_2 + 2HF \quad , \quad k_2 = 2.0 \times 10^{-19} cm^3/s, \qquad (7)$$

and

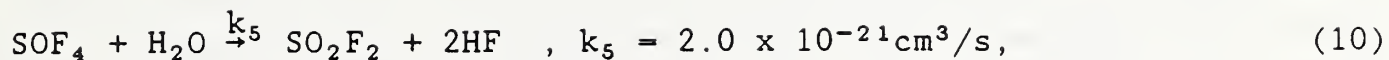$$SF_2 + O_2 \xrightarrow{k_3} SO_2F_2 \quad , \quad k_3 < 5 \times 10^{-16} cm^3/s, \qquad (8)$$

that occur in the main gas volume. The rate for reaction (7) has been measured by Sauers and coworkers [40], and for reaction (8) an upper limit was determined by Plumb and Ryan [38]. The gas-phase hydrolysis processes

$$SOF_2 + H_2O \xrightarrow{k_4} SO_2 + 2HF \quad , \quad k_4 = 1.2 \times 10^{-23} cm^3/s, \qquad (9)$$

and

$$SOF_4 + H_2O \xrightarrow{k_5} SO_2F_2 + 2HF \quad , \quad k_5 = 2.0 \times 10^{-21} cm^3/s, \tag{10}$$

also occur in the main gas volume and can affect the relative oxyfluoride yields after sufficiently long times. It has been shown by Van Brunt and Sauers [41] however, that reactions (9) and (10) are too slow to be of importance for the experimental situations under consideration here.

The model allows for diffusion of reactive species into and out of the different zones, and involves finding numerical solutions to the set of rate equations associated with the reactions mentioned above and in Table 1 coupled with the differential equations for diffusion. The numerical solutions were obtained using a chemical kinetics computer code recently developed at the National Institute of Standards and Technology [42].

Shown in Fig. 19 are examples of calculated SOF_2 and SOF_4 yields-versus-time (or equivalently, net charge transported, $Q = it$) from the proposed model in comparison with experimental data of Van Brunt [19]. The prediction for SOF_4 includes the effect of reaction (6) in the ion-drift zone. The concentrations for SF_6 and H_2O were held constant at the indicated values. The concentrations of the intermediates SF_5 and F are seen to reach constant values almost immediately as required for the steady-state condition. The relatively good agreement between calculated and experimental results was achieved in part by adjusting the relative contribution of reaction (19) to the SF_6 dissociation rate and by treating the volume ratio τ_c/τ_t as an adjustable parameter which was varied within a range restricted by the uncertainty associated with the optical measurement of R, namely R = $(1.5 \pm 0.5) \times 10^2$ cm. The rate of SO_2F_2 production derived from the calculation was five orders of magnitude below the measured rate reported by Van Brunt [19]. This is expected since SO_2F_2 is believed to be formed mainly by reaction (8) involving molecular oxygen which was not included in this model. A proper accounting for SO_2F_2 production requires not only the presence of O_2, but also the inclusion of SF_6 dissociation channels leading to formation of the lower valence sulfur fluorides SF_3 and SF_2.

An investigation of the sensitivity of the model predictions to variations and uncertainties in the various parameters used is underway. A preliminary examination of the special case considered here showed that the electron-impact dissociation rate is indeed the rate controlling factor in oxyfluoride production, and SOF_2 production, in particular, is very sensitive to the relative contribution of reaction (19) to the total dissociation. In the present case, the required contribution from reaction (19) leading to SF_4 as opposed to SF_5 formation is less than 1% of the total. The model predicts that both SOF_2 and SOF_4 production rates increase almost in direct proportion to the current as observed. Although SOF_2 production based on this model is insensitive to variations in $[H_2O]$ as required, the predictions for SOF_4 are
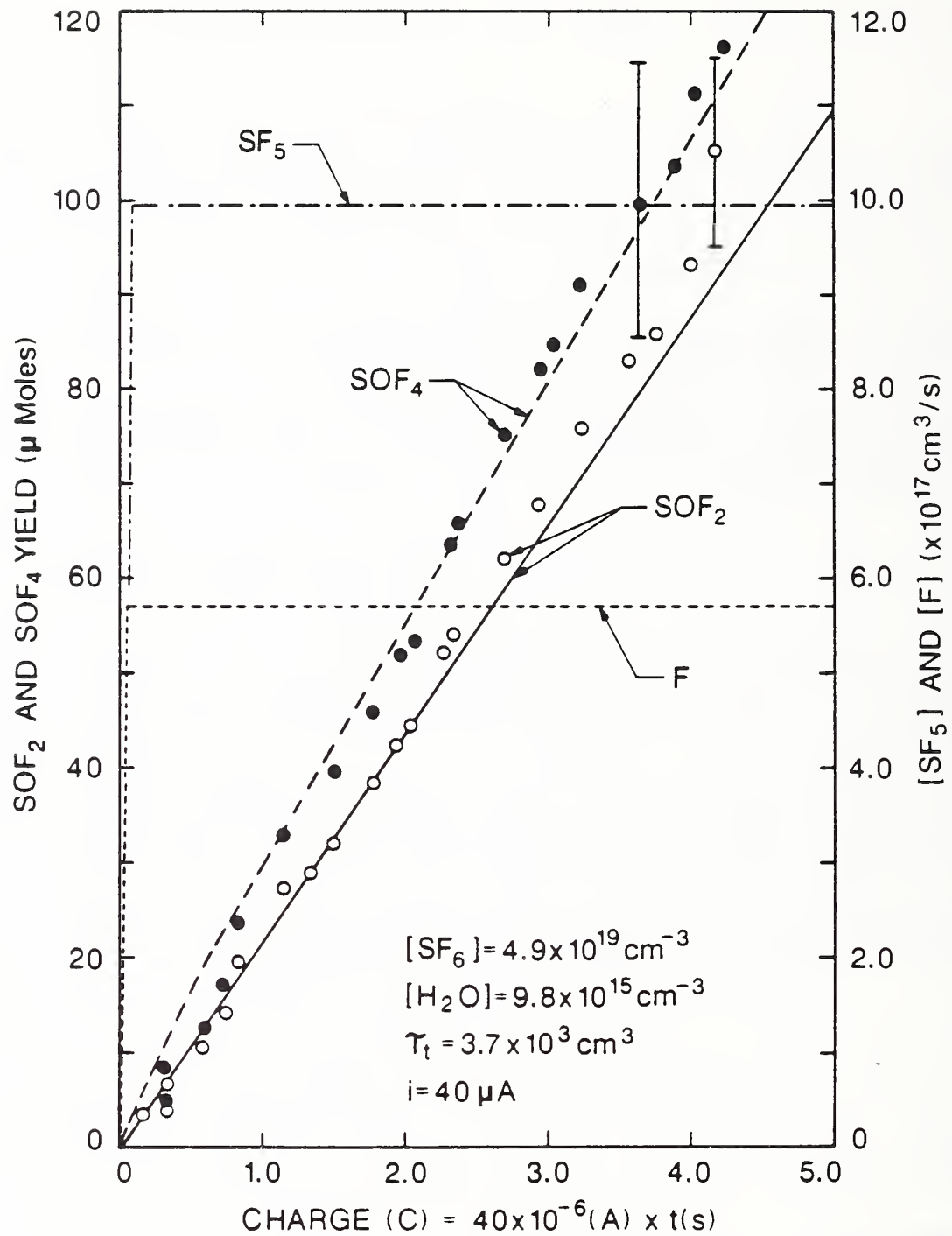
33

Figure 19. Comparison of predicted (solid and dashed lines) and measured (open and solid points) SOF_4 and SOF_2 yields versus charge transported (Q = it) from decomposition of 200 kPa SF_6 containing 200 ppm_v H_2O in a 40 μA negative corona. Also shown are the predicted steady-state levels of SF_5 and F in the glow region of the discharge.

relatively more dependent on [H$_2$O] than the experimental observations would suggest. For the scheme given in Table 1, it was found that reaction (33) is the dominant SOF$_4$ formation mechanism with reaction (25) providing most of the OH. Direct dissociation of H$_2$O appears to be relatively unimportant. The role of H$_2$O in SOF$_4$ production requires further investigations; but based on the case considered here, it would appear that the influence of H$_2$O on SOF$_4$ yield depends on the relative competition between reaction (33) and other mechanisms that can remove OH, especially reaction (31).

3.5 Analysis of Dielectric Strength Data for Binary Electronegative Gas Mixtures

The motivation for this activity was to test a theoretical model that has been proposed [43] to analyze dielectric strength data for binary gas mixtures with the purpose of determining the consistency of these data with relevant information about swarm and electron-collision cross sections for the individual gas constituents. The model was previously used successfully to evaluate dielectric strength data for the gas mixtures SF$_6$/N$_2$, CCℓ_2F$_2$/N$_2$, and CCℓ_2F$_2$/SF$_6$ [43]. In the present work the model was applied to the mixtures SF$_6$/CO$_2$, SF$_6$/Ar, SF$_6$/Ne, and SF$_6$/He [17].

Since details of the model have been described elsewhere [43], only an outline of the main assumptions is given here; namely: 1) the intrinsic dielectric strength of an electronegative gas mixture, i.e., the critical electric field-to-gas density ratio (E/N)$_{c,m}$, is defined by the criterion $\alpha_m = \eta_m$, where α_m and η_m are respectively the electron-impact ionization and attachment coefficients for the mixture; 2) the electron energy-distribution functions for the mixture are Maxwellian; 3) the mean electron energy in a binary gas mixture $\bar{\epsilon}_m$ is given by a weighted sum of the mean energies of the component gases A and B,

$$\bar{\epsilon}_m(F,E/N) = g(F) \; \bar{\epsilon}_A(E/N) + [1 - g(F)] \; \bar{\epsilon}_B(E/N), \; g(F) > 0, \tag{11}$$

where g(F) is the weighting function and F is the gas mixture ratio

$$F = [A]/([A] + [B]), \; 0 \leq F \leq 1; \tag{12}$$

and 4) the dependence of the mean energies $\bar{\epsilon}_A$ and $\bar{\epsilon}_B$ on E/N can be determined by comparing experimentally measured ionization coefficients of the constituent gases with the corresponding coefficients computed for a Maxwellian distribution function using electron collision cross-sections for momentum transfer and ionization as input data, i.e.,

$$[(E/N)(\alpha_i/N)]_{calc} = (\beta_i E/N)(\alpha_i/N)_{exp}, \; i = A, B; \; \beta_i > 0. \tag{13}$$

35

For the mixtures studies here, the E/N-range was subdivided into j sectors, where in each sector the experimental values for (α_i/N) in Eq. (13) were represented by a linear approximation:

$$(\alpha_i/N)_{exp} = a_{ij} + b_{ij} \ (E/N) \quad , \ j = 1, \ 2, \ 3... \quad \quad (14)$$

The F dependence of $(E/N)_{c,m}$ is found by solving Eq. (11) for E/N, once $\bar{\epsilon}_m(F)$ has been determined using the breakdown criterion $\alpha_m = \eta_m$, and once the E/N dependencies of $\bar{\epsilon}_A$ and $\bar{\epsilon}_B$ are known from Eq. (13). The correction factors β_i in Eq. (13) are used to obtain a least squares fit between predicted and experimentally measured $(E/N)_{c,m}$ values. Large deviations of β_i from unity indicate either a failure of the Maxwellian approximation or significant inconsistencies among the breakdown, swarm and cross-section data, or a combination of both problems.

Figures 20 and 21 show the $(E/N)_{c,m}$ results obtained from this "Maxwellian" model in comparison with results from numerical solutions of the Boltzmann Equation as discussed in section 3.1 above for the binary gas mixtures SF_6/Ar and SF_6/CO_2 respectively. The calculations in these figures are compared with data from different measurements [34,44-46]. It is seen that in both cases the agreement among the various calculations and experimental data is quite good.

Although the Maxwellian model appears to give satisfactory results for the SF_6/CO_2 and SF_6/Ar mixtures assuming an equal weighting function for mean energies, i.e., $g(F) = F$, this is not the case for the SF_6/Ne and SF_6/He mixtures. This is indicated in Table 2 which shows that the β_i parameters for SF_6/Ne and SF_6/He deviate significantly from unity and the root-mean-square deviations between the Maxwellian and corresponding experimental data are considerably higher than for SF_6/CO_2 and SF_6/Ar.

The cause of the failure of the Maxwellian approximation for SF_6/He and SF_6/Ne was initially suggested [17] to be the consequence of unaccounted for Penning ionization processes, i.e.,

$He* + SF_6 \rightarrow He + SF_6 + e,$

where He* corresponds to helium in a metastable excited state that exceeds the ionization energy of SF_6. Unfortunately, nothing is known about the rate for this process. The maximum possible influence of Penning ionization on the critical field, $(E/N)_{c,m}$, for SF_6/He and SF_6/Ne was determined from numerical Boltzmann type calculations assuming either that no Penning ionization occurs, or that all He atoms excited to metastable states are quenched by ionizing collisions. The latter case is equivalent to assuming that collisions which produce metastable excitation also produce ionization. The results of this calculation for SF_6/He are displayed in Fig. 22 in comparison with available experimental data [44,45]. It is evident that Penning ionization has an insignificant effect on $(E/N)_{c,m}$ in this case except in nearly pure helium. A similar conclusion can be drawn from the calculations of Kline, et al. [47].

Figure 20. Critical electric field-to-gas density ratio, $(E/N)_c$, as a function of the fractional SF_6 content in an SF_6/Ar gas mixture. Shown are the results of calculations based on the Maxwellian approximation and numerical solutions to the Boltzmann transport equation in comparison with various indicated experimental data.
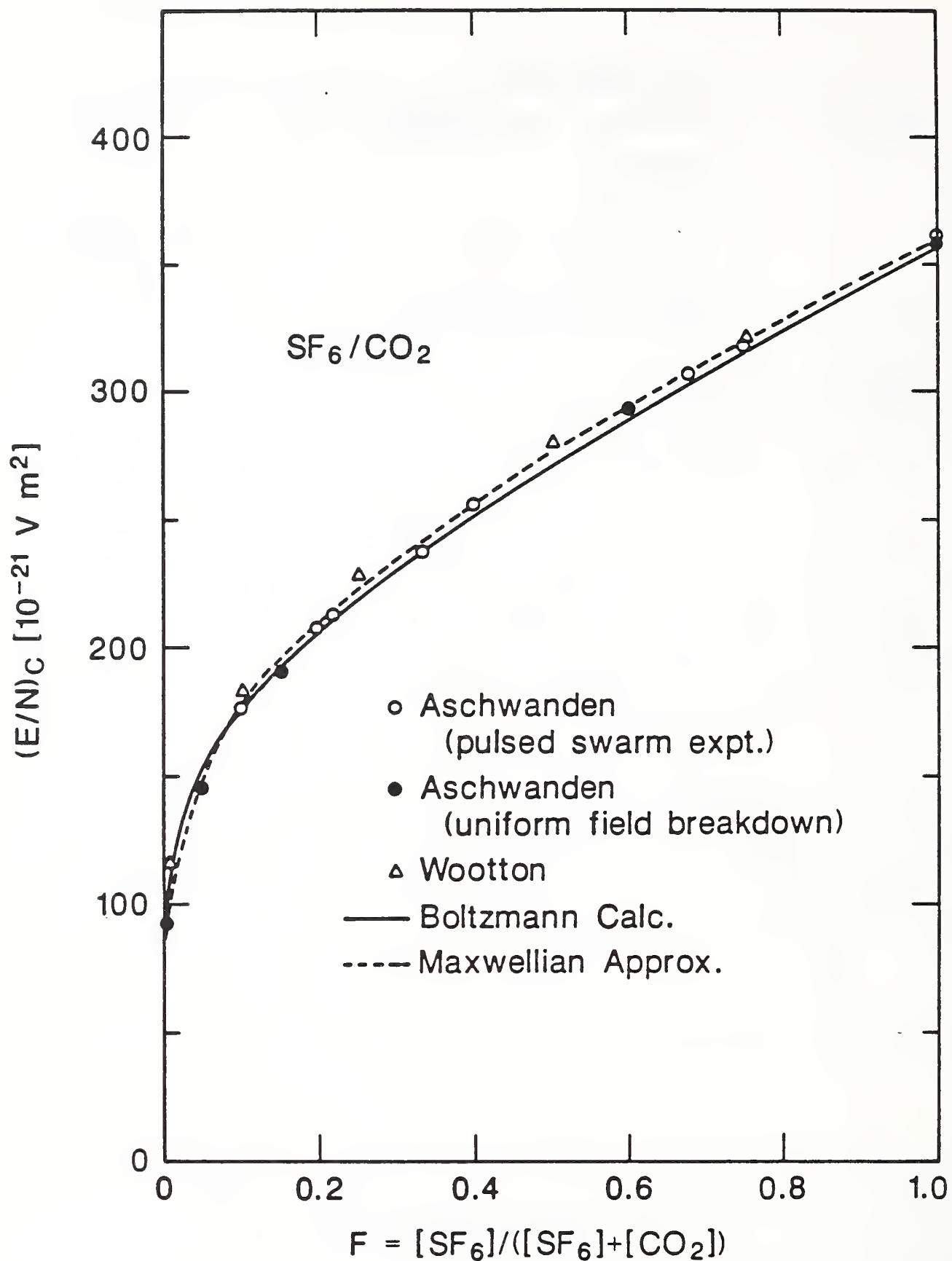
Figure 21. Critical electric field-to-gas density ratio, $(E/N)_c$, as a function of the fractional SF_6 content in an SF_6/CO_2 gas mixture. Shown are the results of calculations based on the Maxwellian approximation and numerical solutions to the Boltzmann transport equation in comparison with various indicated experimental data.
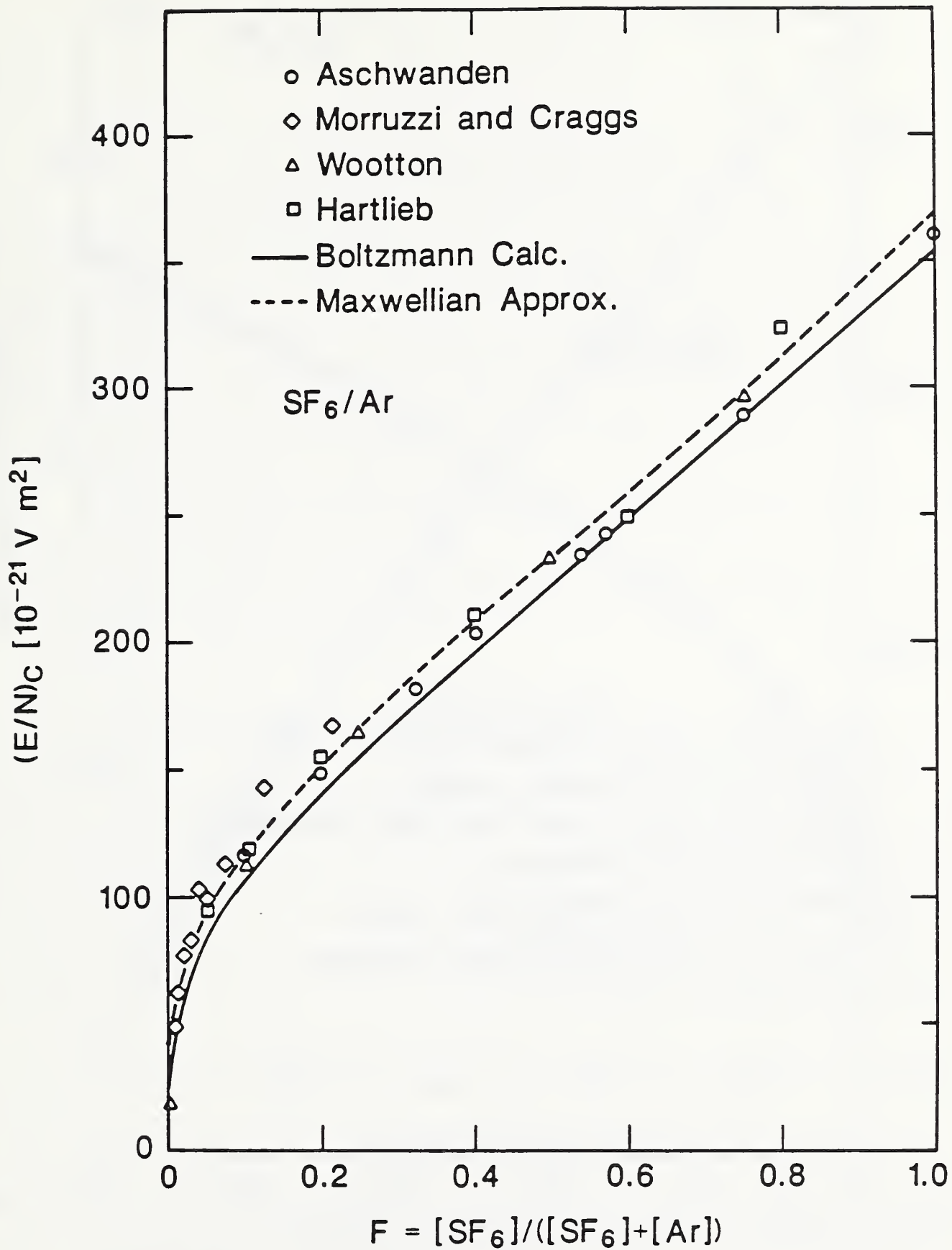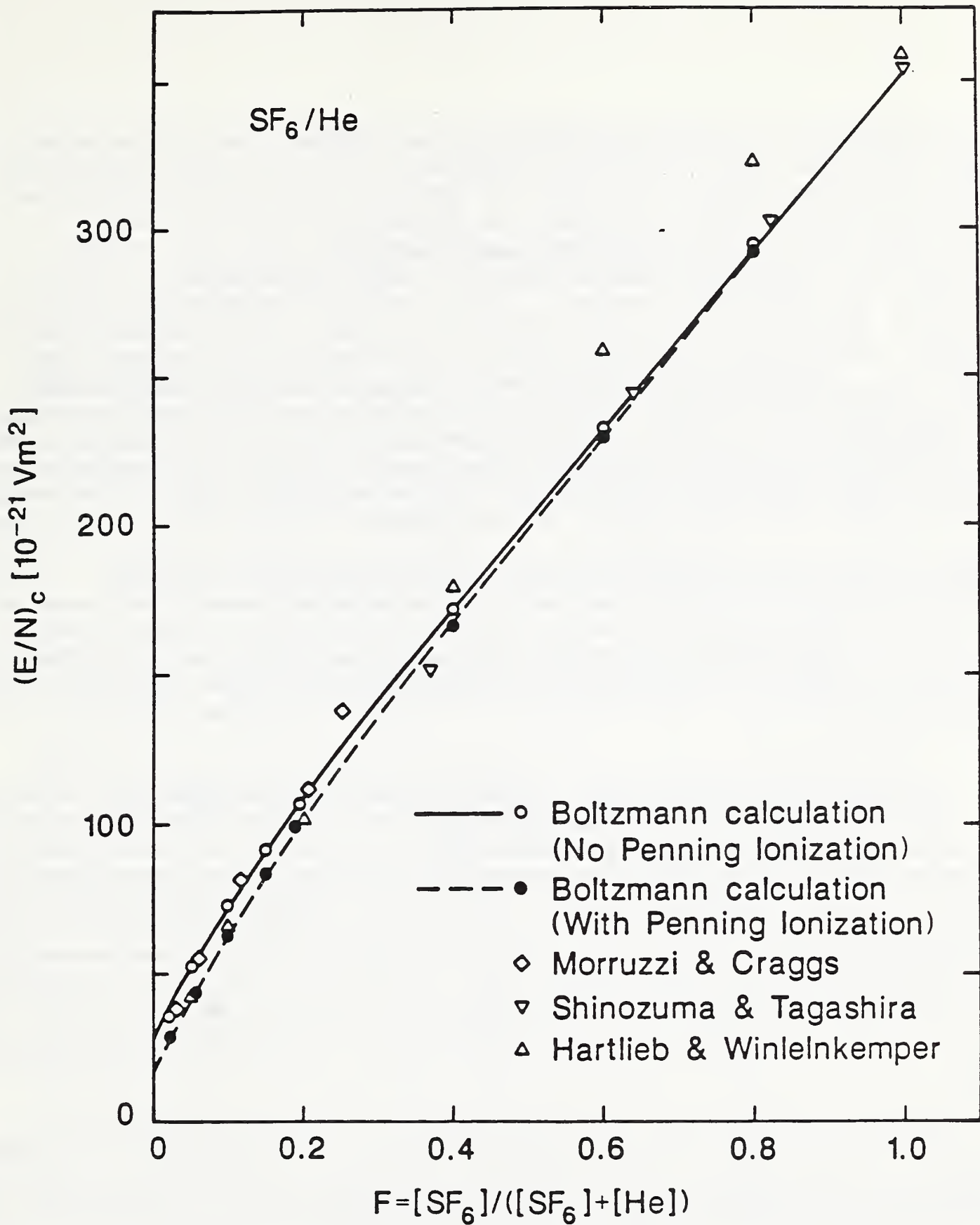
Figure 22. Critical electric field-to-gas density ratio, $(E/N)_c$, as a function of the fractional SF_6 content in an SF_6/He gas mixture calculated from numerical solutions to the Boltzmann transport equation assuming 1) no Penning ionization of SF_6 by metastable He, and 2) the maximum effect of Penning ionization whereby all He excitated to metastable states are quenched in an ionization process. Shown for comparison are various indicated data from experiments.

39

It can therefore be concluded from this investigation that the omission of Penning ionization in the Maxwellian model does not account for its failure when applied to either SF_6/Ne or SF_6/He. It was discovered from calculations of the mean electron energies that the cause of failure lies with the assumption $g(F) = F$. For these mixtures, $g(F)$ must be a much more rapidly varying function of F, perhaps of the form $(1 - e^{-\xi F})$ where [A] in Eq. (12) corresponds to SF_6 and ξ is a constant. This is expected because the lowest excited states of He and Ne are quite high (greater than 19 and 14 eV respectively), which means that they are not very effective in "thermalizing" electrons, i.e., in reducing electron kinetic energy in the gas via inelastic collisions. This is in contrast to SF_6 which has many low-lying excited states. Therefore SF_6 is a much better electron thermalizer than either Ne or He, and the addition of only a relatively small amount of SF_6 to these gases will have a disproportionately large effect on the reduction of $\bar{\epsilon}_m$. Thus, the assumption of $g(F) = F$ in Eq. (11) is not realistic in these cases.

Further investigations into the limits of the Maxwellian model for determining consistency among dielectric strength, electron swarm, and collision cross-section data are underway. The method appears to show promise in providing an analytical procedure for helping to determine the reliability of data on the uniform-field dielectric strength of numerous gas mixtures, especially those for which there exists only limited information on electron collision processes.

Table 2. Correction factors $\beta_i = \beta_A$, β_B (Eq. 13) and root-mean-square deviations found in fitting the Maxwellian model to $(E/N)_c$ for the various binary mixtures containing SF_6.

Gas Mixture:	$\beta_A(SF_6)$	β_B	RMS deviation $(V^2 m^4)$ (for $g(F) = F$)
SF_6/CO_2	0.8	1.0	0.74E-40
$SF_6/Argon$	0.9	1.03	0.14E-39
$SF_6/Neon$	0.7	1.0	0.11E-38
$SF_6/Helium$	1.1	4.7	0.88E-39

4. INTERFACIAL PHENOMENA IN LIQUIDS
Task 04

Edward F. Kelley
Electrosystems Division
National Institute of Standards and Technology

4.1 Introduction

The objective of this research is to understand the mechanisms of failure in practical insulation found in power apparatus. Electrical insulation schemes in practical apparatus generally involve composites of different media such as solids and liquids. For example, transformer windings are often wrapped with layers of paper and separated with pressboard and the entire assembly placed in a liquid insulant such as transformer oil. In order to minimize the destruction of, or damage to, such apparatus, it is necessary to develop a complete understanding of the failure mechanisms for all the range of stresses to which the apparatus is subjected. These include stresses which occur both during ordinary operation when the apparatus undergoes slow degradation due to aging, during extreme operation, including peak usage periods, and the times when the apparatus is subjected to surges or impulses from a variety of sources.

Understanding of the failure mechanisms will permit designers of apparatus and component-insulation materials to appreciate the inherent limitations of the media and the entire systems. For instance, if it were determined that sub-micron particles (conducting or non-conducting) were responsible for partial discharge initiation, it would not be likely that systems could practically be designed to eliminate such contamination. However, if research were to demonstrate that partial discharge activity was caused by micron-sized conducting particles, then designs which eliminate such contamination could be of interest. Such contaminents would be symptomatic of the assembled system and would not depend upon some fundamental property of the insulation (unless the liquid or solid were of poor quality and contaminated).

To illustrate an aspect of liquid breakdown which relates to the more fundamental characteristics of liquids in general and independent of the apparatus, consider fast breakdown. It has been shown that liquid insulation can break down at a lower voltage than expected when subjected to steep-front pulses. We can explain this behavior with our understanding of streamer structure and development, and such behavior is recognized as a fundamental property of the liquid insulation. Liquid quality can modify some of the details of the behavior, but no amount of purification will eliminate the problem associated with fast breakdown.

Such research on breakdown phenomena in liquids focuses on what we must live with and what we can avoid if we need to. But in order to be able to make these claims, we need to understand the processes involved at more fundamental levels than are presently known. If one is able to model the processes involved in terms of the liquid properties, then one can reach the necessary level of understanding to recognize the limits or boundaries which

are imposed by the insulation media. This does not refer to a gross empirical model, but to a model which derives its parameterization from the properties of the liquids used. The aim of such research serves to establish frontiers and to identify clearly the causes of degradation and failure.

In Table 3 we list a number of aspects of liquid-solid insulation which are know to affect performance. This list is not intended to be complete, but is included to outline the diversity of phenomena which characterize the acceptability of insulation systems. The list also serves to provide orientation to our research. The areas of free-charge field enhancement and breakdown streamer initiation and growth have received attention from this laboratory in the past. The work reported here concentrates on partial-discharge phenomena and experimental apparatus which assists in their observations. The details of these results are discussed below.

4.2 Image-Preserving Optical Delay

General

An optical imaging system has been invented to perform photographic observation of random, transient phenomena. An electrical signal arising from the transient phenomenon is used to trigger an image-converter camera as soon as possible after the signal is produced. By means of the image-preserving optical delay, the image associated with the phenomena is delayed from reaching the camera for a longer period of time than it takes the camera to begin taking pictures. Therefore, the first few frames show photographs of any events which occurred before the transient was created. In this way we can obtain photographs of random events before they happen, after they occur.

Results Summary

The need for an image-preserving optical delay (IPOD) arises when information is desired concerning the development of a very fast, random phenomena. Processes such as electrical breakdown or partial discharges in insulation studies are random, and the critical information concerning the process often occurs prior to the electrical event. For example, if one wanted to understand how lightning is generated, the information regarding the initiation and development of the process is not readily obtainable after the lightning has occurred. The information which is needed is a documentation of the phenomena prior to the lightning strike. In electrical breakdown processes in general, it is the prebreakdown events that are often of interest. These events may only last a few microseconds or less prior to the breakdown. If one happens to have the recording camera operative exactly at the right moment, then the prebreakdown phenomena can be photographed. However, to routinely take a picture of the processes which precede such a random event, it is necessary to delay the image from reaching the photographic recording device until it is possible to trigger the photographic system (open the "shutter"). In the case of an image converter camera (ICC) it may require 100 ns to trigger the electronics to make the camera operate and it is a simple matter to arrange for the electrical breakdown to trigger such a camera. If the image information coming from the region between the electrodes can be delayed longer than the required 100 ns, then the camera,

Table 3. Aspects of Liquid-Solid Insulation Correlating Performance

SPACE-CHARGE AND SURFACE-CHARGE FIELD ENHANCEMENTS
    Chemical nature and temperature of liquid affects space-charge content
    possibly enhancing electric field increasing discharge activity.

PARTIAL DISCHARGE DEGRADATION
    LIQUID DEGRADATION:
        CHEMICAL CHANGES:
            Increasing conductivity.
                Production of new molecular charge carriers can increase
                conduction which produces heating and accelerates aging
                process.
            Increasing space-charge field enhancement.
                Chemical byproducts can contribute to generation of space
                charge in liquid increasing probability of further partial
                discharge activity or even breakdown.
            Production of corrosive byproducts.
                Leads to more rapid degradation of insulation components.
        PARTICULATE CHANGES:
            Increasing probability of more partial discharges.
            Increasing probability of streamer initiation and breakdown.
            Contamination of solid surfaces thereby increasing their
                probability of discharge activity.
    SOLID DEGRADATION:
        Permanent damage resulting in channels or voids.
    COINCIDENCE WITH IMPULSE
        Serves as initiation site for impulse breakdown streamer.

BREAKDOWN STREAMER INITIATION AND GROWTH CHARACTERISTICS
    Similar problems as with partial discharges although damage is more
    serious. Streamer structure can be controlled somewhat by liquid used.

NATURAL CHEMICAL DEGRADATION
    Impurities and contaminants in media can change insulation properties
    over a long period of time even if the material is not subjected to use.

ELECTROCHEMICAL DEGRADATION
    Subjection of media to electric fields can cause chemically induced
    changes from nature of charge carriers and processes at electrode
    surfaces.

THERMAL DEGRADATION
    Conductivity of media and electrohydrodynamic motion of liquid provide
    heating thereby enhancing chemical degradation.

ELECTROHYDRODYNAMIC MOTION
    Liquid motion contributes to reducing temperature of hotter areas and to
    diluting contaminants generated by partial discharges -- both are
    benefits. Liquid motion can sweep particulate impurities into high field
    regions increasing the probability of discharge activity.

looking back in time, will be able to photograph the phenomena which occurred just before the breakdown event responsible for triggering the camera.

An array of ten 2.5-cm diameter flat mirrors symmetrically located about a central 5-cm diameter flat mirror is placed on the optical axis at the focal point of a spherical concave mirror having a diameter of 15 cm and focal length f of 152 cm. The light from an object placed a distance 2f from the concave mirror can be continuously refocused through the system by aligning the mirrors appropriately. The image is formed a distance of 2f from the concave mirror with a total magnification of unity. Such a system will provide a 160-ns delay in the light and provide a resolution of 10 line pairs per millimeter (lp/mm). The delay unit is less than 2 m in length and 0.2 m in width. In Fig. 23 we show a simplified drawing of the delay in an experiment to observe electrical breakdown. The image converter camera is triggered by means of a pulse transformer which senses the moment of breakdown.

A delay of 390 ns can be arranged by replacing the spherical concave mirror with a mirror having a 365 cm focal length. The penalty is a loss of resolution. Using the same flat-mirror array, the resolution will be about 5 line pairs per millimeter (lp/mm). Such a poor resolution is less than the maximum 10-lp/mm resolution of the image-converter camera. To prevent a loss in image quality using the longer focal-length mirror, it is possible to magnify the image before it enters the delay, and then reduce it at the image-converter camera. By extension, the magnification can be increased up to approximately 100X in order to provide high-magnification, high-speed photographs of transient phenomena initiation.

4.3 Partial Discharge Initiation

General

A collaborative experiment with the University of Tennessee successfully monitored the initiation and evolution of partial discharges in transformer oil subjected to dc. By means of the image-preserving optical delay we were able to photograph the initiation of a partial discharge and follow its development. The current supplied to the partial discharge was simultaneously monitored by a specially designed amplifier. This is the first time that the initiation of a partial discharge has been photographed. There were no surprises in that the structure of the partial discharge was similar to the structure of a streamer produced by the application of an impulse voltage.

Results Summary

An immediate application of the image-preserving optical delay (IPOD) was to photograph partial discharges in liquids under the application of dc. The objective of this collaborative experiment with the University of Tennessee was to combine their electronics expertise in making fast current measurements of a partial discharge (PD) with the capabilities at NIST to take high-speed photographs back in time. The result was to monitor the current supplied to a PD and simultaneously photograph the evolution of the partial discharge from its inception through its growth.
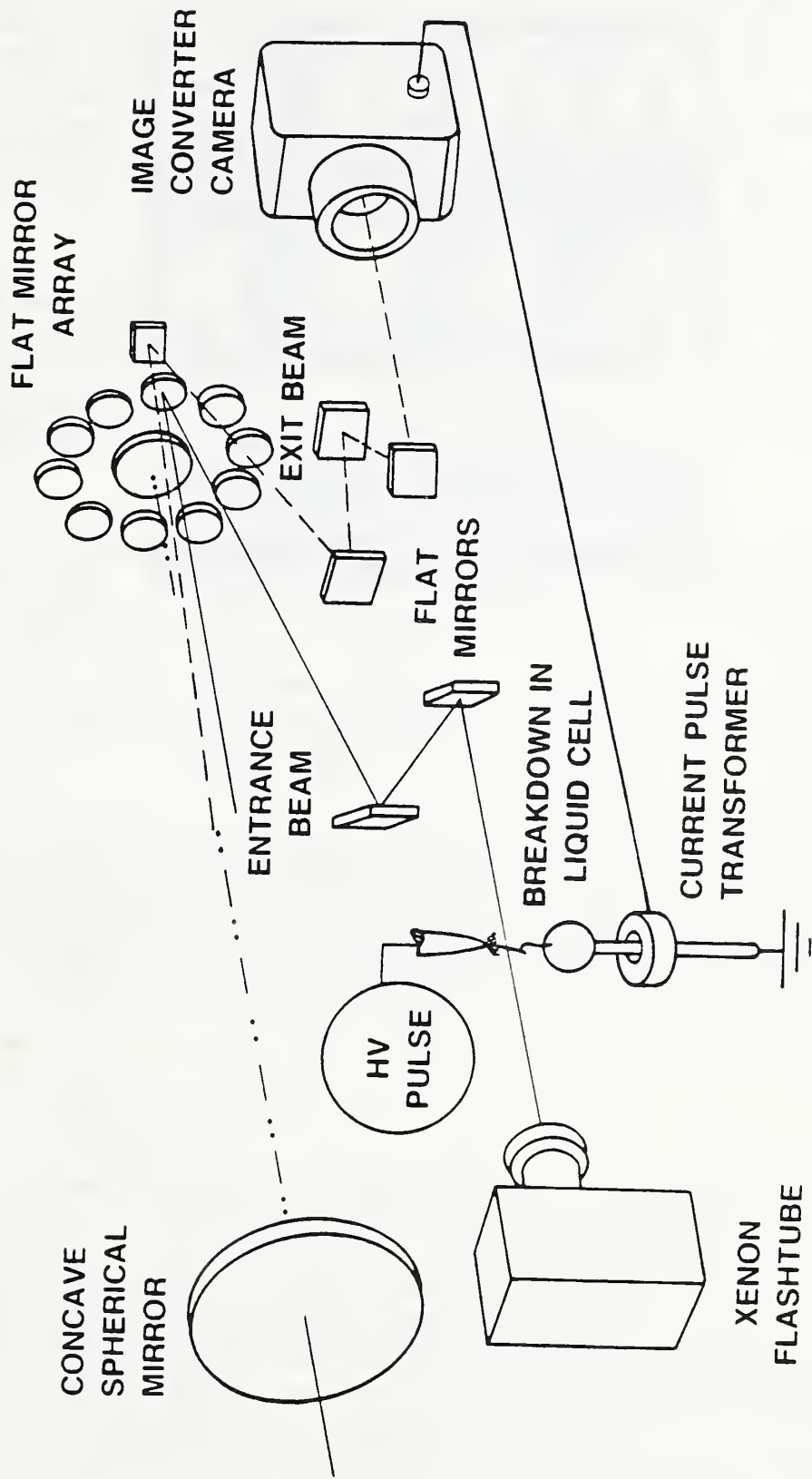
Figure 23. Schematic of use of image-preserving optical delay in liquid breakdown experiment.

In order to accomplish this simultaneous measurement not only was a sensitive amplifier needed, but an amplifier with a fast through-put so that when coupled with two pulse generators it was possible to fire the image-converter camera (ICC) and a Pockels-cell shutter (PCS) all within 150 ns after the PD initiated. The PCS was necessary to limit the light striking the ICC to the time period necessary to make the exposure. Since cw laser light was needed to illuminate the tip of the needle electrode during the application of dc, without the PCS too much light would impinge on the photosensitive surface of the ICC and fog the film.

The results showed that the PD grows uniformly while the current supplied to the PD is principally in the form of pulses. This was observed for both the negative and positive PD. Figure 24 illustrates the uniform growth characteristics in contrast with the discreet nature of the supplied current. This feature of uniform growth despite pulsed current is true for the initiation and growth of discharges in liquids under the application of impulse voltages.

By using high-magnification (75X), we attempted to observe any particles which might be responsible for the initiation of the PD. The resolution was limited to approximately 5 μm due to the optical system employed. No particles of that size were observed in the vicinity of the point which could cause PD initiation. If particles, even ones smaller than 1 μm, do not serve as initiation sites for PD's, then further research is needed to fully understand the charge-injection process at high fields.

In a future experiment it is anticipated that an examination will be made of the effects of pressure on the initiation and growth of partial discharges in attempts to correlate the current signature with growth structure. Provided an improved optical system is possible, we also anticipate exploring to determine the phenomena at the limits of optical resolution.

4.4 Streamer Initiation and Collapse Under Pressure

General

A collaborative experiment was conducted with the University of Tennessee on the initiation of streamers in liquid under the application of impulse voltages applied to a needle-sphere gap. A square pulse was applied having a peak voltage so that the streamer would not grow to breakdown before the pulse was chopped to zero. With the application of pressure, the initial streamer was observed to collapse and disappear while the voltage remained on the needle tip. When the voltage was chopped, a new streamer appeared which resembled the structure of the anode streamers, the branches of which did not follow the previous branches of the cathode tree which injected the charge in the liquid. An estimate of the amount of charge injected and the charge diffusion time is shown to be consistent with the high resistivity of hexane.
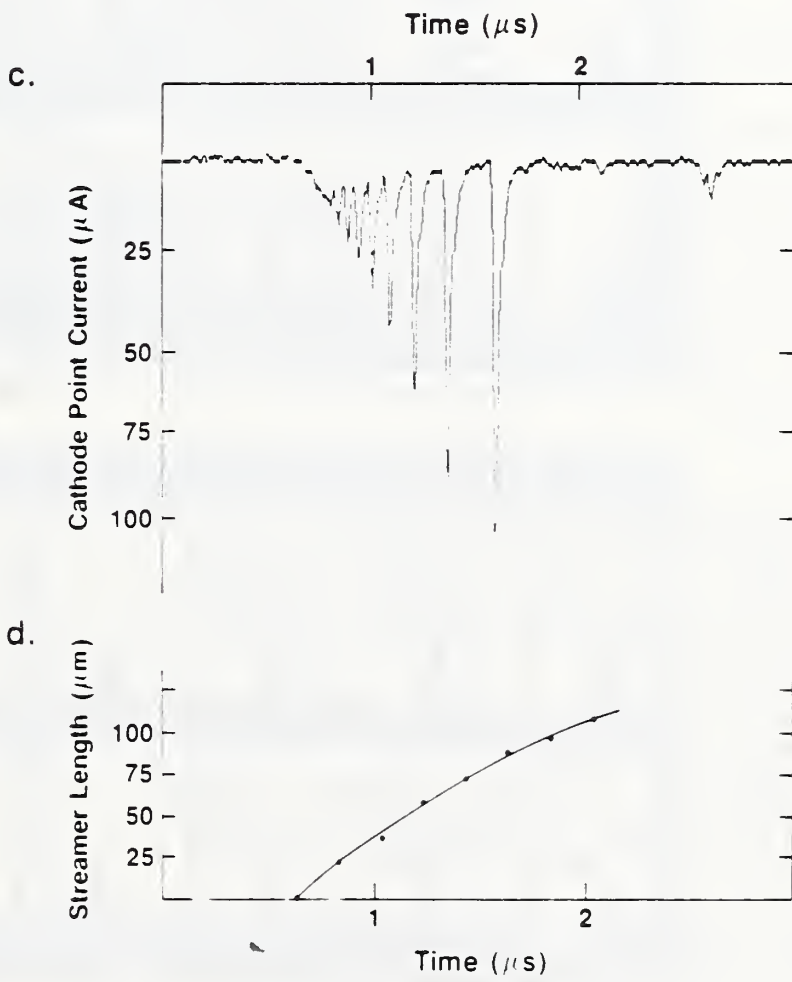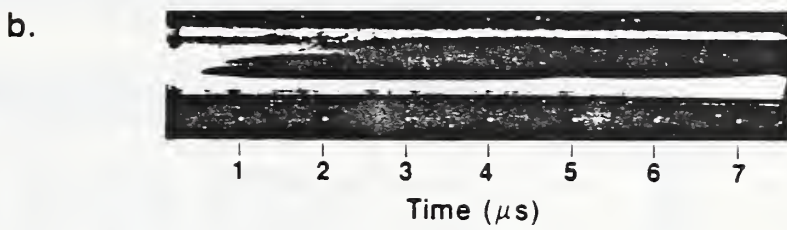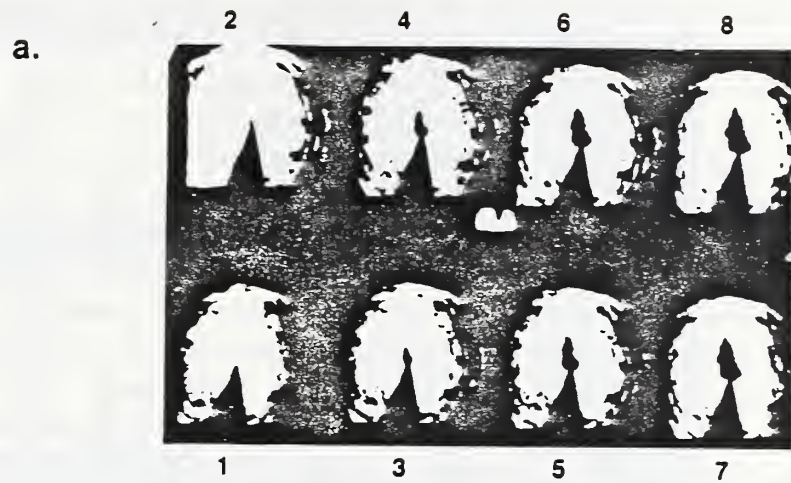
46

Figure 24. Uniform partial discharge growth despite pulsed current supplied.

47

Results Summary

The photographic results of the structure of partial discharges conducted in the previous study (see 4.3) shows a similarity to the initiation phase of streamers in liquids under the application of impulse voltages. To explore the similarities further, a needle-sphere electrode system having a gap of 5 mm is placed in hexane and is subjected to a square pulse having a rise-time of order 100 ns and a selectable chop time from 10 μs to 100 μs. The current supplied to the resulting streamer is monitored while the growth of the streamer is photographed by an image-converter camera (ICC). Because of the nature of the impulse generator used much of the current waveform information is contaminated by noise associated with the generation of the pulse. However, a remarkable phenomena is observed in the streamer structure. At atmospheric pressure (0.1 MPa), the cathode streamer displays its characteristic bush-like shape - an almost spherical structure which increases in size until a faster filamentary event emanates from the bush and bridges the gap causing breakdown. Reducing the voltage will cause the bush to appear, but it does not grow to breakdown. As the hydrostatic pressure increases, it becomes more difficult to initiate the cathode streamer or bush, and one generally finds that the bush tends to become more branched and less filled. In addition, once a voltage is reached where the cathode streamer initiates, it is observed to collapse within a few microseconds because of the pressure even though the voltage remains on the needle. If the voltage is sustained, the cathode bush will eventually collapse completely leaving only traces of its existence. The charges which were responsible for the growth of the bush (or streamer) are left in the liquid and do not diffuse quickly into the surrounding liquid. This can be verified by chopping the voltage to zero. The needle is now at zero (ground) potential and there are negative charges in the liquid. Another streamer develops quickly which permits these negative charges to be removed from the liquid into the tip of the needle. The observed streamer is very similar to the filamentary streamers created when the needle is the anode. This "reversed" streamer is approximately the same size as the cathode streamer which deposited the charge, but its shape is very different.

In Fig. 25 we show moderately magnified ICC photographs of the time-evolution of the streamers. In these photographs, the first frame is in the lower left hand corner and the last frame is in the upper right hand corner. The height of each frame is approximately 1.2 mm, and the tip radius of curvature is approximately 40 μm. In Fig. 25a the time between photographs is 2 μs and the entire process of the disintegration of the cathode bush and the creation of the anode-type tree can be seen. The first frame is taken after the voltage is applied and the voltage is chopped between the fourth and the fifth frames. It is interesting to note how the cathode streamer collapses. The collapse begins nearest the needle and extends to the end of the streamer. This is readily seen in Fig. 25b. The between fram is 210 ns. The creation of the "reversed" anode-like tree occurs rapidly. In Fig. 25c the time between frames is 50 ns and the process is completed within that time interval.

We can make an estimate of the amount of charge deposited in the liquid by this pressure-induced collapse process. We have established in an earlier
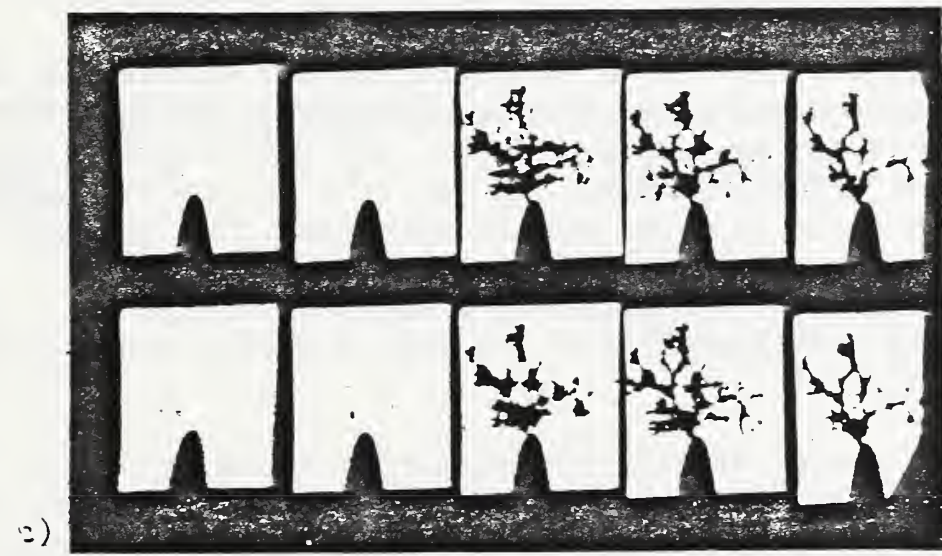
Figure 25. Framing camera photographs of streamer collapse and regeneration under chopping of voltage pulse. Liquid is under pressure. a) 2 μs between frames, b) 210 μs between frames, c) 50 μs between frames (after chop).

paper that these streamers act as if they are extensions of the electrodes and have the characteristics of conductors [53]. In that paper, a model was developed whereby the spherical structure of the streamer (especially the cathode bush) can be approximated by a sphere at the potential of the needle. A simple approximation to the resulting potential is obtained by choosing an appropriate point charge which would produce a quasi-spherical equipotential of about the same size. We adapt that model to the present situation as follows: Consider a sphere which is roughly the same size as the cathode bush before it collapses entirely. From Fig. 25 we could use a diameter of 0.75 mm. The sphere has a radius R and the gap between the bottom of the sphere and the grounded electrode is G. The grounded electrode is actually a sphere in this experiment, but because of its comparatively large radius of curvature (1.3 cm) and the fact that this is only an order-of-magnitude calculation, we assume it acts like a plane to simplify the calculation. If V is the potential on the quasi-point-charge sphere, the method of point-image-charges can be used to obtain the size of the charge needed to create an equipotential similar to this imaginary sphere. The charge is given by

$$q = 4\pi\epsilon V(h^2 - G^2)/2G. \tag{1}$$

Here ϵ is the permittivity of the liquid ($1.9\epsilon_0$) and h is the height of the charge q above the ground plane:

$$h = \alpha + \beta - G/3, \tag{2}$$

where

$$\alpha = (S + \sqrt{P})^{1/3}, \quad \beta = (S - \sqrt{P})^{1/3},$$

$$S = (8/27)G^3 + 2G^2R + 2GR^2,$$

$$P = (32/27)G^5R + (140/27)G^4R^2 + 8G^3R^3 + 4G^2R^4$$

For small spheres high above the ground plane, the location of the charge is approximately at the center of the sphere: $h \simeq G + R$. Using a radius of $R = 0.375$ mm, a gap beneath the sphere of $G = 4.25$ mm, and a voltage of $V = 130$ kV, we find that a charge of $q = 11$ nC at approximately the center of the sphere would produce an equipotential which would match the voltage which is applied to the tip ($h = 4.624$ mm, vs the center at 4.625 mm). In Fig. 26 we show a diagram of this model drawn to scale. It may well be argued that there is a contribution to the field from the needle electrode, but in this calculation it is ignored for simplicity since we are interested in an estimate of the charge deposited in the liquid. Assuming this charge is evenly distributed through this spherical volume, we have a charge density of 49 μC/cm^3.

The fact that such a high charge density can exist for a number of microseconds without dispersing can be seen from a simple calculation involving the conductivity of the liquid. In this calculation we will ignore any external field for the purposes of simplicity. Consider an isotropic, linear, resistive medium with conductivity σ. For such an ohmic liquid the current density is proportional to the electric field
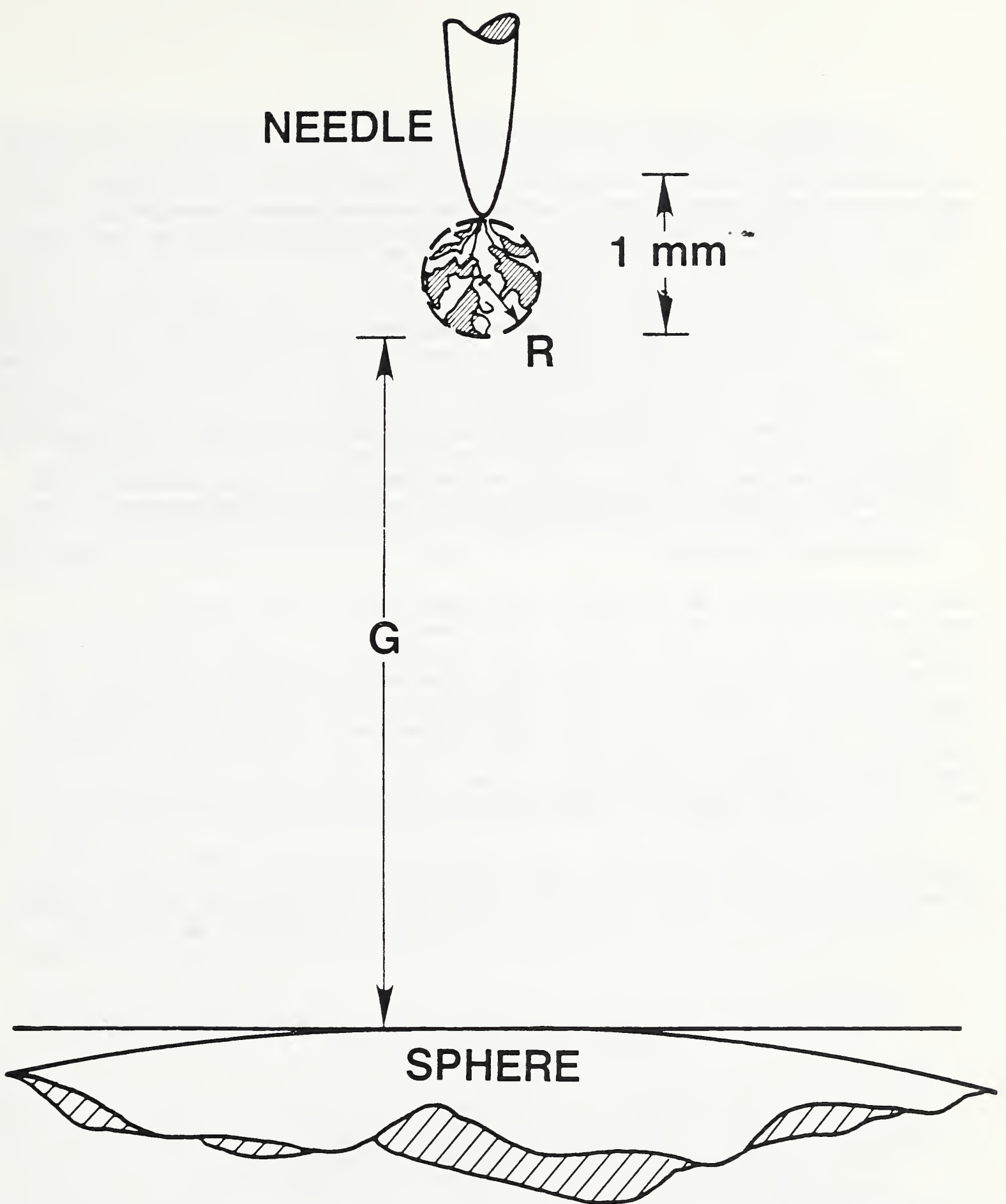
50

Figure 26. Quasi point charge model of collapsing cathode streamer.

$$J = \sigma E. \tag{3}$$

The time rate-of-change of charge leaving the quasi-point-charge sphere with surface area Σ is simply the outflow of the current density through the surface of the sphere, which by the divergence theorem of Gauss is the volume integral of the divergence of the current density:

$$- dq/dt = \iint J \cdot n \, d\Sigma = \iiint_{\Sigma} \nabla \cdot J \, dxdydz. \tag{4}$$

Since the divergence of J and E are related by ohms law, Eq. (3), and since the divergence of the electric field is proportional to the charge density (Maxwell's equations), $\nabla \cdot E = \rho/\epsilon$, the volume integral is proportional to the charge contained within the surface, and the rate equation reduces to

$$dq/dt = - q \, (\sigma/\epsilon). \tag{5}$$

Thus, the charge is seen to deplete from the region of the sphere exponentially with a characteristic time constant of $\tau = \epsilon/\sigma$. To require that the time constant be long compared to 20 μs amounts to requiring a conductivity such that $\sigma \ll 0.84 \, \mu$S (or a resistivity $1/\sigma \gg 120$ MΩcm). Comparing this to typical values of conductivity for liquid hydrocarbons of 10^{-12} S or less, it is reasonable to postulate that the charge will remain essentially motionless after the collapse of the bush [54]. Clearly this simple model neglects charge migration and other complications; it only serves to provide us with a means of checking the reasonability of the estimate.

The results presented here suggest further experimentation. By using liquids such as water which have much higher conductivities, we should be able to see an extension of the "reversed" tree beyond the collapse of the cathode bush depending upon how long we wait for the chop or decay of the voltage.

5. CHARACTERIZING TRANSIENT MEASUREMENTS BY USE OF THE STEP RESPONSE AND THE CONVOLUTION INTEGRAL
Task 05

R. H. McKnight, J. Lagnese and Y. Zhang
Electrosystems Division
National Institute of Standards and Technology

5.1 Introduction

The measurement of high-voltage transients requires a means of reducing the high voltage signal to levels which are compatible with data recording equipment. The measurement devices which accomplish this reduction are known generically as voltage dividers and they should ideally scale the signal to a smaller value without distortion. These dividers, however, invariably

introduce some distortion of the input signal, due primarily to inadequate bandwidth or aberrations such as overshoot. This distortion may be negligible or totally unacceptable, depending on the allowable error associated with the particular measurement requirement. One example of the type of distortion encountered in cascading systems is the effect on rise time, which can be calculated for certain conditions by using the well known root-mean-square expression, $\tau_{eff} = \sqrt{\tau_1{}^2 + \tau_2{}^2 + \ldots}$ where the individual rise times are those of the cascaded system [55]. It should be noted that this calculation is frequently applied inappropriately, since it applies only to systems (and pulses) which have monotonic transitions. For many applications, free-standing voltage dividers are used and the examples presented in this paper are primarily of this type of divider. As will be pointed out, however, the method has general applicability to other voltage measuring systems.

If the divider system is assumed to be linear, then the general methods of linear-system analysis can be applied to characterize the system. Two equivalent approaches involve either time-domain or frequency-domain analysis. In the frequency-domain [56], the divider is characterized by the following equation

$$
\begin{bmatrix} V_{in}(\omega) \\ I_{in}(\omega) \end{bmatrix} = \begin{bmatrix} A_{11}(\omega) & A_{12}(\omega) \\ A_{21}(\omega) & A_{22}(\omega) \end{bmatrix} \begin{bmatrix} V_o(\omega) \\ I_o(\omega) \end{bmatrix}. \tag{1}
$$

The voltage transfer function, $H(\omega)$, is defined for zero output current, $I_o = 0$, i.e.,

$$
H(\omega) = V_o(\omega)/V_i(\omega)\big|_{I_o(\omega) = 0} = 1/A_{11}(\omega). \tag{2}
$$

The conventionally defined divider ratio is given by

$$
N = A_{11}(0) = \lim_{\omega \to 0} A_{11}(\omega). \tag{3}
$$

if the limit exists. For some dividers, capacitive dividers for example, the limit does not exist and the ratio is defined for a region of little change in $A_{11}(\omega)$. In general, the elements of the matrix are complex numbers containing both amplitude and phase information. Clearly, one of the requirements in analyzing the divider in terms of its frequency response is the ability to measure that response. In practical terms, this is not an easy task [55]. It certainly is not practical to provide a complete response curve, so that some limits must be applied and these limits must be based on an understanding of the divider response. Commercial network analyzers can be used to provide quickly both amplitude and phase information about a given circuit. Unfortunately, these analyzers are not usually available in laboratories where transient measurements are to be made.

In the time-domain, the divider characteristics are incorporated in the impulse response. Under the assumption that the system is linear, causal and time-shift invariant, the input and output voltage are related through the convolution integral (also known as Duhamel's integral), given in Eq. (4) [58].

$$v(t) = \int v(s) \ g(t-s)ds = \frac{d}{dt}\int v(s)[u(t-s)]ds \tag{4}$$

where $g(t-s)$ is the system impulse response and $u(t-s)$ is the step response.

It is generally not feasible to measure the impulse response directly. Because of the impulse and step response relationship indicated in Eq. (4), the step response can be used to characterize the system. This approach is attractive for many laboratories, since a transient recording device is required to make measurements and can also be used to record the step response, if the bandwidth, sampling rate, etc., are adequate. Step (or square wave) responses are frequently used in the laboratory to align compensated probes and, as noted below, are used to determine divider characteristics qualitatively.

The use of the step response to characterize systems for high voltage measurements is detailed as a part of both IEEE (IEEE 4) [59] and IEC (IEC 60-1 to 4) [60] standards concerned with the measurement of standard pulses used in the electrical power industry. In each, various parameters are obtained from a measured step response and are used to predict whether a given measuring system is adequate to provide a measurement within the uncertainty limits specified by the standards. The step response is not used directly in the actual measurement, and there has been much discussion, both published and in working group meetings about the usefulness of the step response parameters in the existing standards [61,62,63]. The appropriate interpretation of the step response itself in real measuring systems was also extensively debated prior to and during the process of developing the existing standards [64,65,66,67]. Different parameters obtained from experimental step responses have been proposed as alternatives in the existing standards, but have not been adopted and also have generated much discussion [62]. A proposed revision to the IEC standard recommends that the accuracy of the measurement be determined by use of a measuring system that has been compared to a reference system maintained by the appropriate national laboratory [68].

5.2 Discussion of Proposed Method

Described below is the use of experimentally determined step responses along with analytic waveforms to determine the suitability of a particular measuring system for making measurements of interest and to present examples of the application of the method. The method involves the convolution of the experimental step response with analytic waveforms which represent the ideal waveform expected in the experimental arrangement. For example, for the full lightning waveform, this would be a double exponential with appropriate time constants. The same waveform would be used for canonical EMP waveforms, with an appropriate change in time constants. Actual waveforms obtained from a measuring system which was known to introduce negligible errors could also be used in the calculation. The use of this method has been discussed at various

times and in working group meetings and one application is presented in a paper describing comparisons of two dividers [69]. Two earlier communications describe convolution calculations and their application to measurement analysis [70,71].

Values of waveform parameters such as peak-value and front-time, which is approximately the 30-90% transition time for standard, or chopped lightning waveforms (defined in the existing IEC and IEEE standards), or risetime (appropriately defined) and peak value for an arbitrary waveform, can be determined for both the input and calculated output waveform. By comparing the values, the error introduced by the measuring system can be estimated. This estimate should not be considered as constituting a number which can be used to make a correction. Rather, it represents an uncertainty bound on the actual measurement and is an estimate of the best measurement that can be made with a given system for the assumed waveform. Systematic errors, random noise, and other confounding factors will further degrade the quality of the measurement. However, this method does allow a direct indication as to whether or not the dynamic response of a measuring system is adequate for the measurement as represented by the step response used in the convolution.

5.3 Experimental Method

One necessary component of the evaluation method described here is an experimentally determined step response. Methods for obtaining the step response of free-standing divider systems are given in [59,60] and one recommended method is indicated in figure 27. Here the divider assembly and the associated leads are brought to a steady-state voltage, typically less than 1 kV, and the system is then shorted to ground through a fast-acting switch. Conventionally, this switch is a small mercury-wetted relay which has closure times of the order of 1 ns. The output of the divider system then is the step response. As noted earlier, there has been extensive discussion in the literature and at various meetings about the relationship of the step response, determined using the method shown above, and the actual measurement made in a laboratory experiment. These concerns are based on several objections, including the change in geometry when the divider is attached to the test generator and object, the impedance mismatch between the transmission line formed by the line connecting the divider to the signal to be measured, the traveling wave aspect of the leads connecting system components, and the effect of source impedance, both in the step response measurement and the test itself. These concerns add uncertainty to the measurement, but are not (with the possible exception of the source impedance) a cause of inadequate dynamic response in the divider system.

As part of recent studies to determine sources of error introduced when two dividers are being compared for purposes of calibration, step responses for a range of different conditions were measured for two free standing dividers designed to measure standard and chopped-lightning impulses as defined in IEC and IEEE standards [72]. An example of the range of responses obtained for one of these dividers is shown in Fig. 28.

The parameter changed in these measurements was the value of the damping resistor, RD, shown in Fig. 27. The oscillations seen in the step response
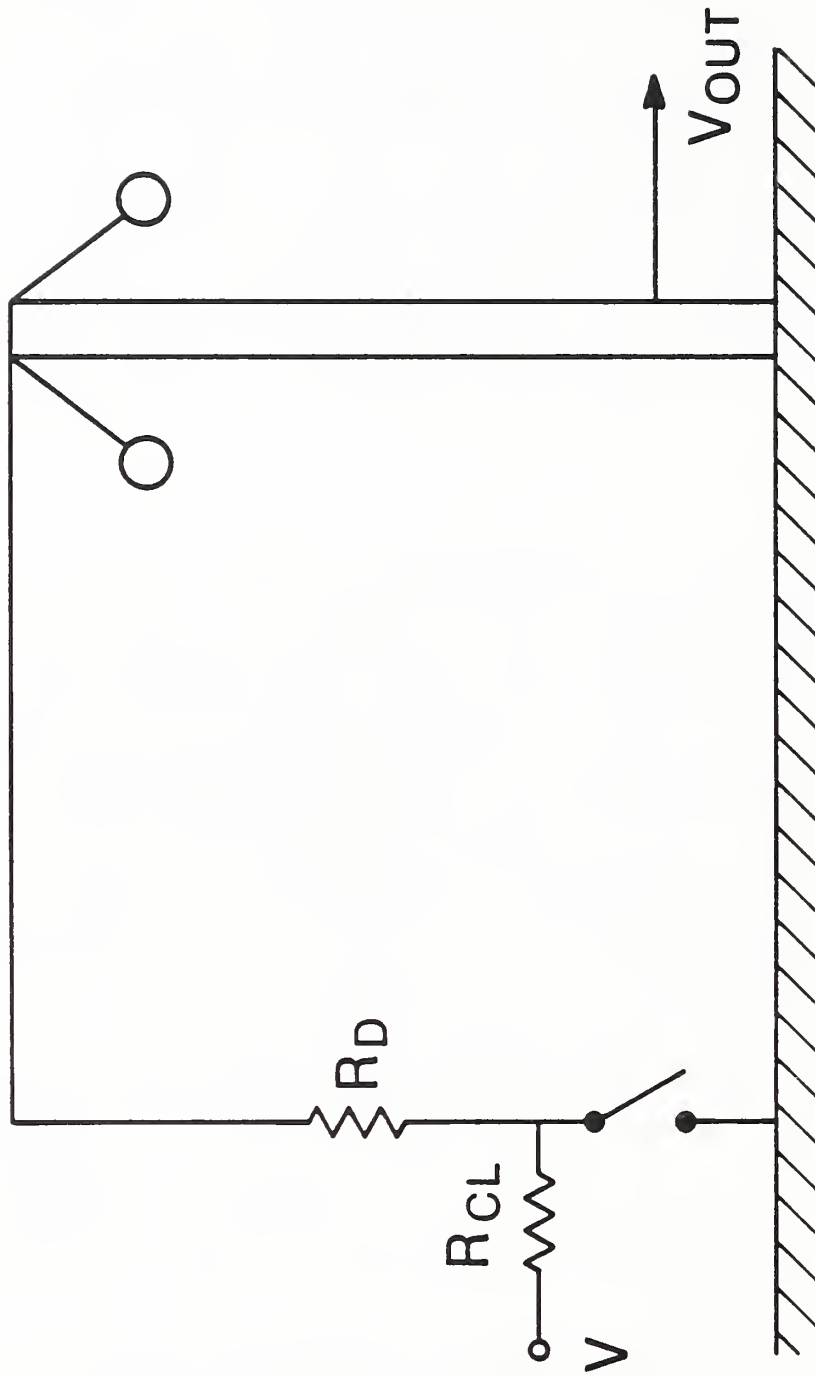
Figure 27. Configuration for obtaining step response of free standing divider (Ref. 58). R_D is a damping resistor, while R_{CL} limits the current flow from supply V during the period the relay shorts to ground.

result primarily from the inductance and capacitance associated with the external lead, and the stray capacitance-to-ground of the divider itself including the capacitive grading ring attached to the top of the divider. Selected parameters obtained from the step response measurements as defined in the IEC and IEEE standards for two dividers, designated NBS1 and NBS3, with different-response characteristics are listed in Table 4. The definitions of these parameters are not presented here, and the numbers listed in Table 4 are given only for the purpose of illustrating the effect of the damping resistor on divider response.

Table 4. Effect of Damping Resistor on Divider Response

R_d (ohms)	T_n (Unit Step Response) (ns)	T_α (Partial Step Response) (ns)	Overshoot (%)
		NBS1	
0	23	27	39
50	29	30	28
150	33	36	14
250	41	44	6
400	52	53	2
		NBS3	
0	19	17	24
150	23	20	11
350	28	29	3
550	36	36	1

For voltage measurement systems installed in devices such as gas-insulated power equipment or pulse-power systems, as compared to free standing devices, the main difficulty in applying step response measurement methodology is that of producing a fast step in the equipment. Such steps have been produced by charging the system and then shorting-to-ground through an existing switch or through a switch installed for the test. In some test lines or specific geometries, it may be possible to apply a step from an external generator and observe the wave propagating on the line by means of the installed sensor. An example of this approach, done in a test line designed to evaluate fast sensors, is shown in Fig. 29, where the directly measured input signal and the output from a small resistive divider with overshoot are shown for comparison [73]. Sensors used to measure transients in gas-insulated power equipment and pulse-power systems, for example, have been subjected to step-response evaluation and several examples have been published. Input and output step waveforms for voltage dividers designed for use in gas insulated equipment are shown in [74]. A fast current probe, a subnanosecond attenuator, and a fast divider are similarly characterized in [75,76,77]. These "evaluations" are qualitative, and basically attempt to show that the step-response of the system has a transition time much faster than the anticipated signal to be measured, as well as some modest degree of
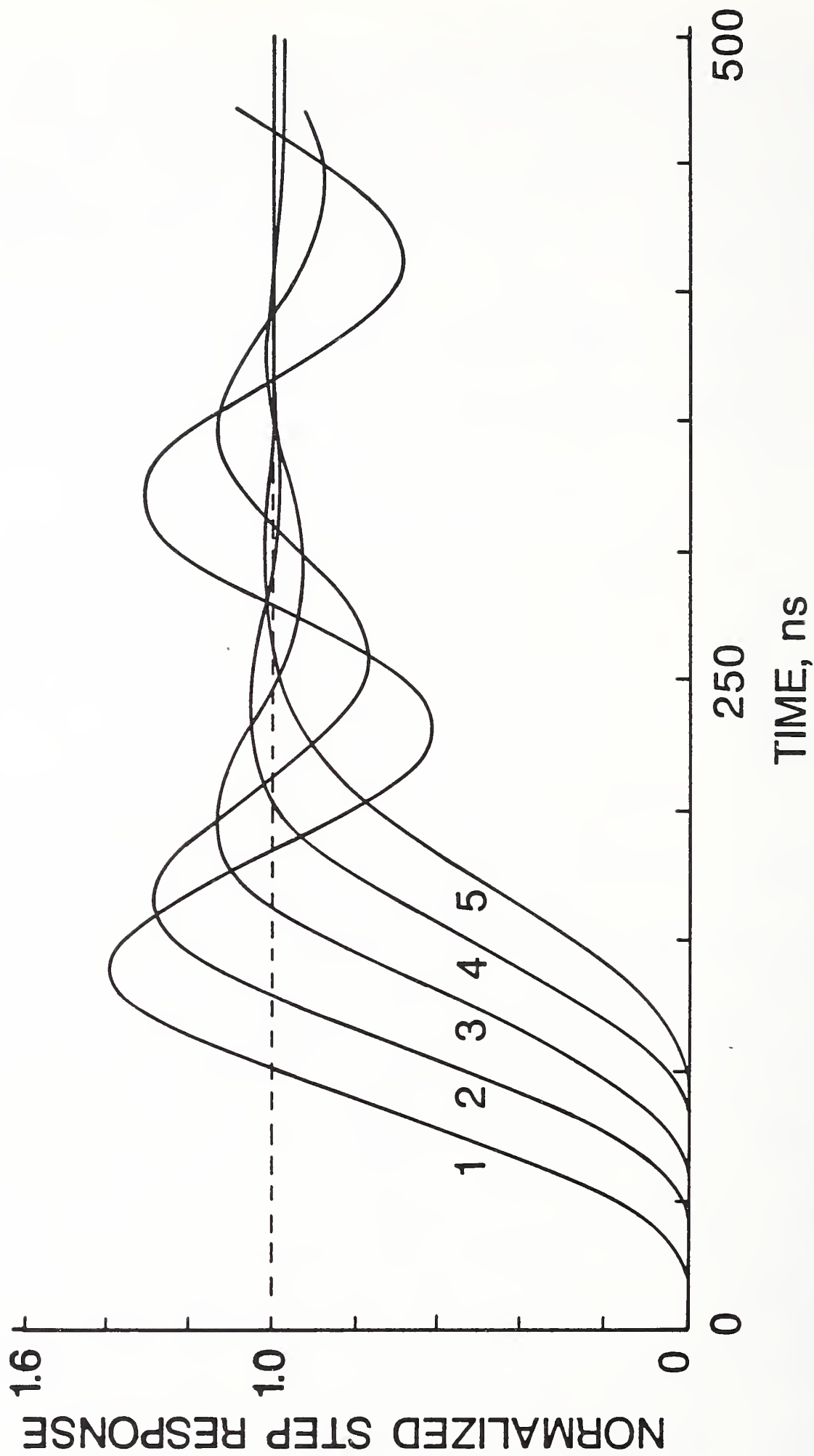
57

Figure 28. Step response of NBS1 divider. (1) RD1 = 0 Ω, (2) RD1 = 50 Ω, (3) RD1 = 150 Ω, (4) RD1 = 250 Ω, (5) RD1 = 400 Ω.

overshoot, and so would contribute a negligible error in the actual measurement.

5.4 Convolution Calculations

The functional form of the double exponential voltage waveform used in these calculations is given in Eq. (5), while the parameters α and β for four different waveforms are given in Table 5.

$$v(t) = A(\exp(-\alpha t) - \exp(-\beta t)) \tag{5}$$

	Table 5. Parameter Values for Selected Waveforms	
Waveform	α (s^{-1})	β (s^{-1})
Standard 1.2x50	1.39×10^4	2.71×10^6
Standard 0.9x50	1.39×10^4	3.61×10^6
Fast waveform 1	1.39×10^6	66.3×10^6
Fast waveform 2	4.0×10^6	476×10^6

In (5), A is a normalizing factor. The designation of the waveforms by a "T1xT2" statement refers in the case of the standard lightning waveforms to approximate front time and the time for the waveform to decay to 50% of the peak value measured from the peak. The two fast waveforms are used to represent particular waveforms of interest to workers studying the effects of fast transients on various equipment. The first is roughly a "50x500 ns" waveform, while the second is a canonical waveform frequently used in EMP calculations. Two different standard lightning waveforms were used. One had front and fall times near the 1.2x50 microsecond waveform of the standard, while the second had a faster front time. In addition to the full waveform, chopped waveforms were also used in the calculations. For these, the standard waveforms were disrupted at some fraction of the peak value and brought linearly to zero in a chosen time, typically 50 or 100 ns.

The experimentally determined step responses shown previously and a digitized representation of the input waveform were used in the convolution calculations. The calculation is straightforward and can be done on a personal computer. An example of a convolution is displayed in Fig. 30 where both input and output waveforms are shown for the NBS1 divider configured for near critical damping. This represents the slowest front time measured for
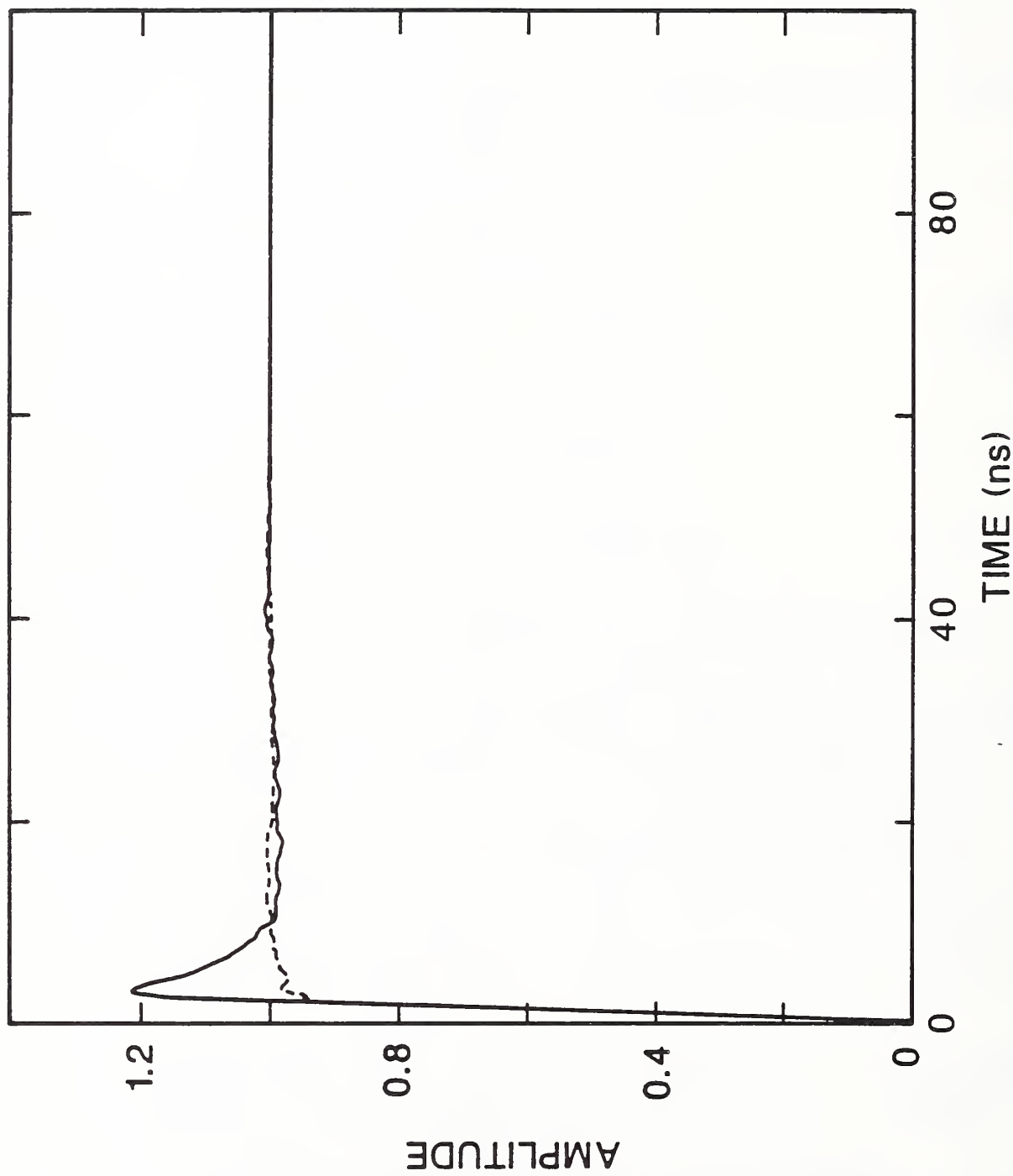
59

Figure 29. Input step (solid) and output signal (dashed) from a small resistive divider located in a coaxial test line. The input signal was produced by a fast cable pulser.

the divider. In Fig. 30 and all comparison figures, the input waveform has been normalized to have a peak value of 1.

Similar calculations for a chopped waveform and the same divider configuration are shown in Fig. 31. These calculations illustrate the distortion introduced in the output waveform as a result of the inadequate dynamic response of the divider. As is well known, the chopped waveform is significantly more difficult to measure accurately than is the full lightning waveform. Front times and peak values (normalized) obtained from a set of calculations for two dividers NBS1 and NBS3 are summarized in Table 6.

Two different chopped waveforms were used for illustration. The values presented with front times of about 1 microsecond were calculated using the 1.2x50 waveform chopped at 0.9 of the peak value. Those with the shorter front times represent a chop at 0.75 of the peak value of the 0.9x50 waveform. This waveform represents an extreme condition, and would not realistically be used in measurements. These calculations illustrate the errors that can be expected as a divider's dynamic response becomes inadequate.

For full-lightning impulses, these results indicate the two dividers would be expected to provide accurate measurements. Front-times show larger differences, in part due to uncertainty in calculating front times when there are superimposed oscillations. For the chopped-lightning measurements, the differences become much more significant. In particular, for the early chop on the faster waveform, the NBS1 divider would be expected to show a significant error, but as noted above, a waveform like this would probably not be used in actual measurements. In a recently completed international comparison of impulse measuring systems, experimental results were obtained which were consistent with these calculations [78].

Convolutions clearly show that superficial deductions based on observations of step response measurements may be misleading. For example, a theoretical step response was devised in which there was significant overshoot and severe oscillations of varing frequency. The three step responses used in the calculations are shown in Fig. 32. The overshoot is extreme (about 80 percent), while the resonant frequencies of the system ranged from 5 to 16 MHz. Figures 33 and 34 show convolutions of the two extreme cases. Clearly, both the step response of the measuring system and the waveform to be measured are important in the calculation. The high-frequency oscillations seen in Fig. 33(a) do not contribute distortion, since there is little spectral power-density in the waveform to be measured at this frequency. As the resonant frequency of the system decreases, there is more overlap between the frequency space representing the signal and the divider response. The effects consequently become more severe.

These calculations also present a problem which is of practical concern in the measuring laboratory and one which is inadequately dealt with in the present standards. The oscillations on the front of the output make a calculation of the time parameters, subject to considerable error, such as transition times based on percentages of the waveform, (front time or rise time).

61

Table 6. Calculation of Distortion Introduced by Various Divider Configurations

Full Lightning Impulse

Divider	Rd(Ω)	Actual Front Time	Calculated Front Time	Actual Max	Calculated Max
NBS1	0	1.2μs	1.27μs	1.0	0.996
NBS1	250	1.2	1.26	1.0	0.998
NBS1	500	1.2	1.27	1.0	0.995
NBS3	0	1.2	1.29	1.0	0.996
NBS3	250	1.2	1.21	1.0	1.0
NBS3	550	1.2	1.21	1.0	1.0
NBS1	0	0.9	0.96	1.0	0.994
NBS1	250	0.9	0.95	1.0	0.996
NBS1	500	0.9	0.96	1.0	0.992
NBS3	0	0.9	0.97	1.0	0.993
NBS3	250	0.9	0.92	1.0	1.0
NBS3	550	0.9	0.92	1.0	1.0

Chopped Lightning Impulse

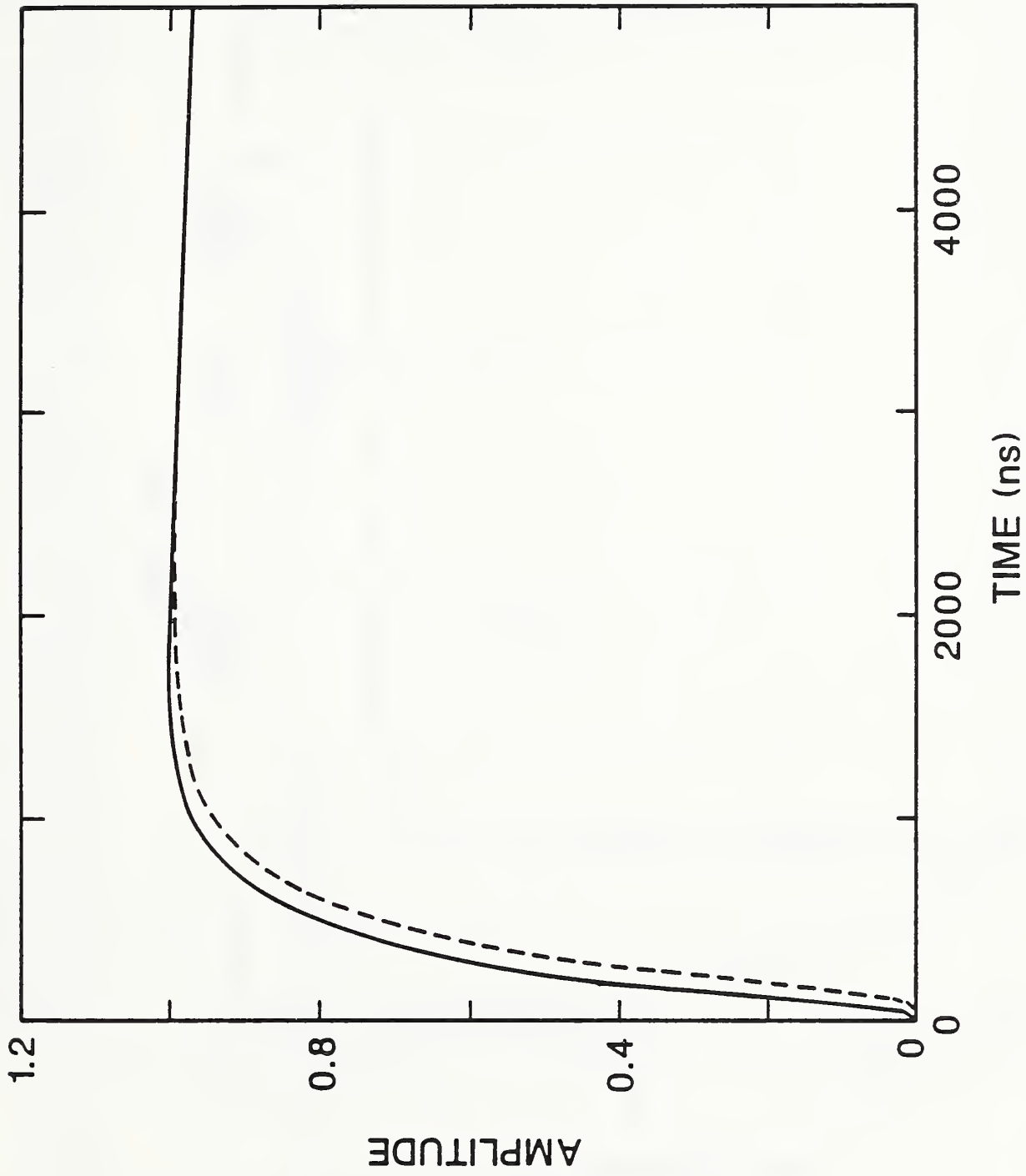| Divider	Rd(Ω)	Actual Front Time	Calculated Front Time	Actual Max	Calculated Max
NBS1	0	1.04μs	1.02μs	1.0	0.975
NBS1	250	1.04	0.95	1.0	0.962
NBS1	500	1.04	0.95	1.0	0.958
NBS3	0	1.04	1.02	1.0	0.973
NBS3	250	1.04	1.00	1.0	0.987
NBS3	550	1.04	0.99	1.0	0.984
NBS1	0	0.42	0.38	1.0	0.947
NBS1	250	0.42	0.37	1.0	0.898
NBS1	500	0.42	0.37	1.0	0.886
NBS3	0	0.42	0.39	1.0	0.938
NBS3	250	0.42	0.39	1.0	0.947
NBS3	550	0.42	0.39	1.0	0.944

Figure 30. Convolution of the measured step response for NBS1 configured to be near critically damped (E in Fig. 28) with the 1.2x50 waveform. Input waveform is solid, output dashed.
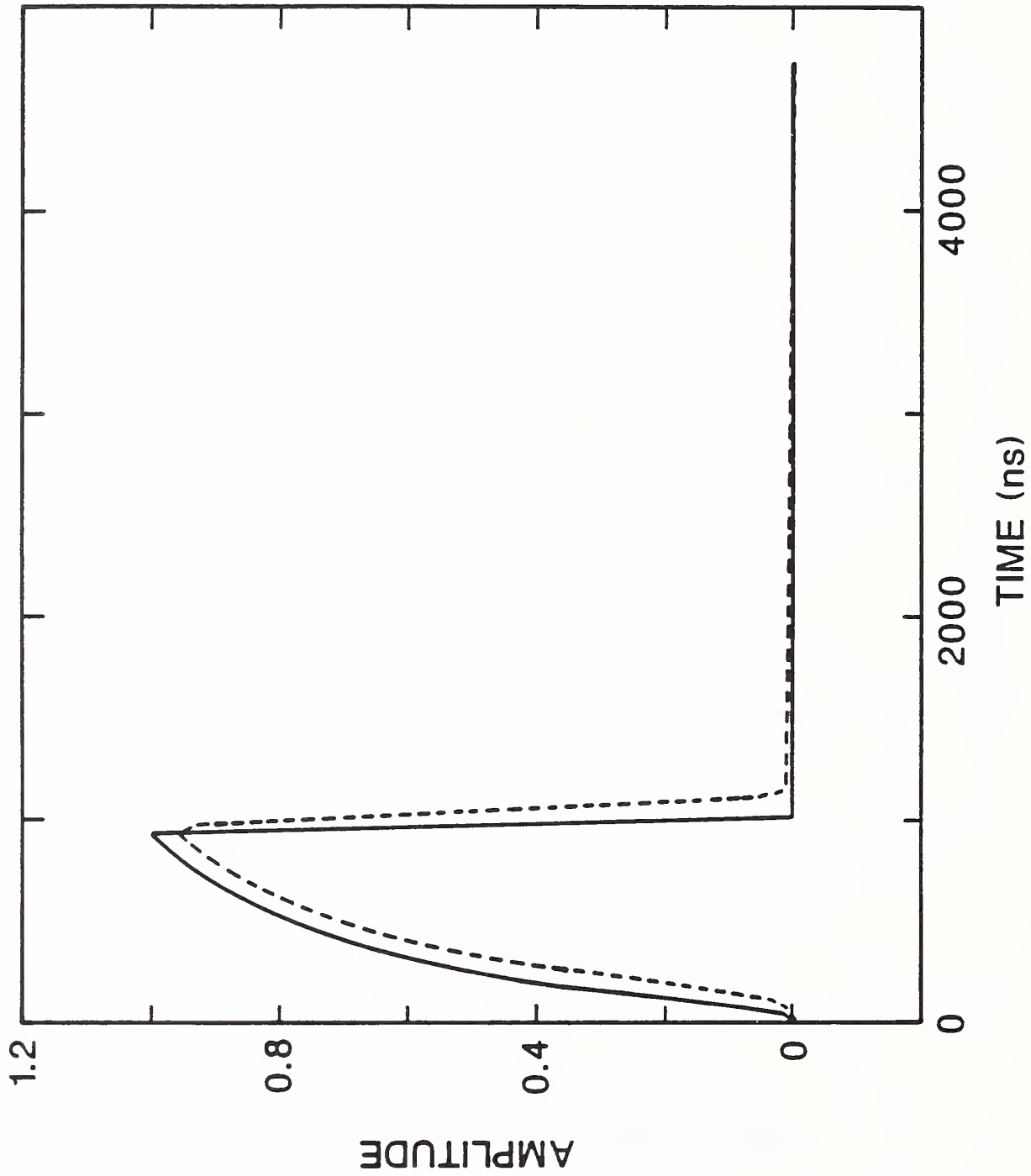
63

Figure 31. Convolution of the same step as in Fig. 30 with a chopped waveform. Chop was at 90% of the full waveform peak and the chop was a linear 50 ns ramp to zero. The input waveform was renormalized to 1 for presentation.
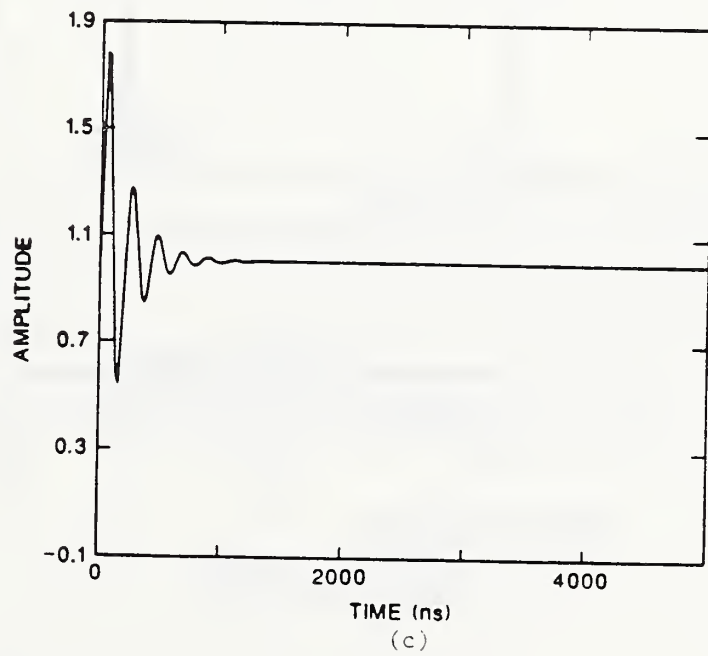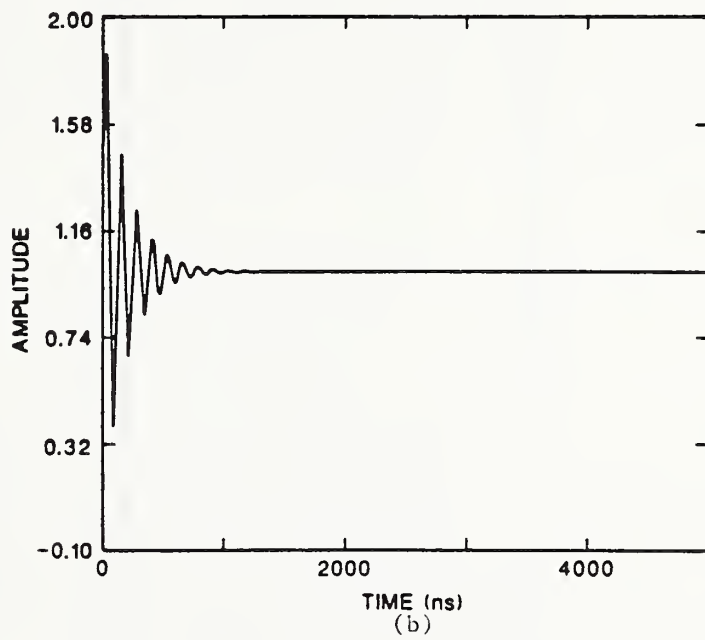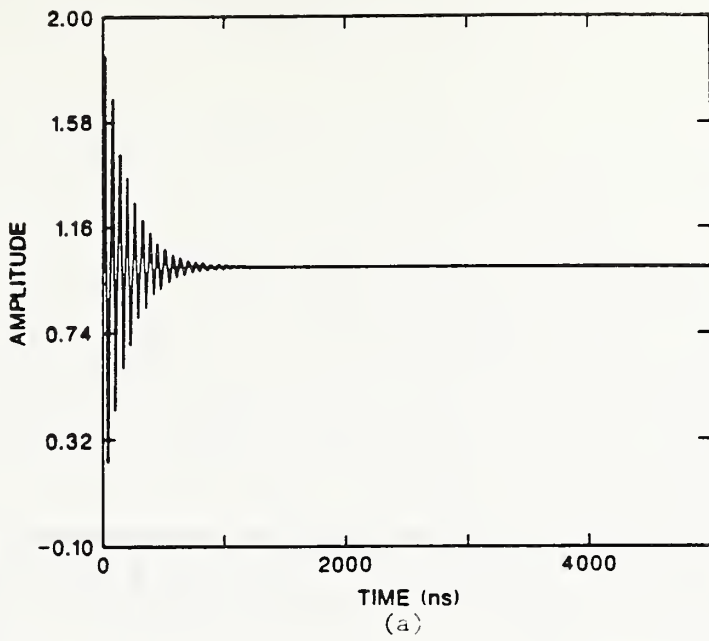
64

Figure 32. Empirical step responses calculated to show effects of ring frequency. Overshoot in each case was approximately 80 percent, and the ring frequencies were approximately (a) 16 Mhz; (b) 8 Mhz; (c) 4.8 Mhz. The settling time was slightly more than 1 microsecond.
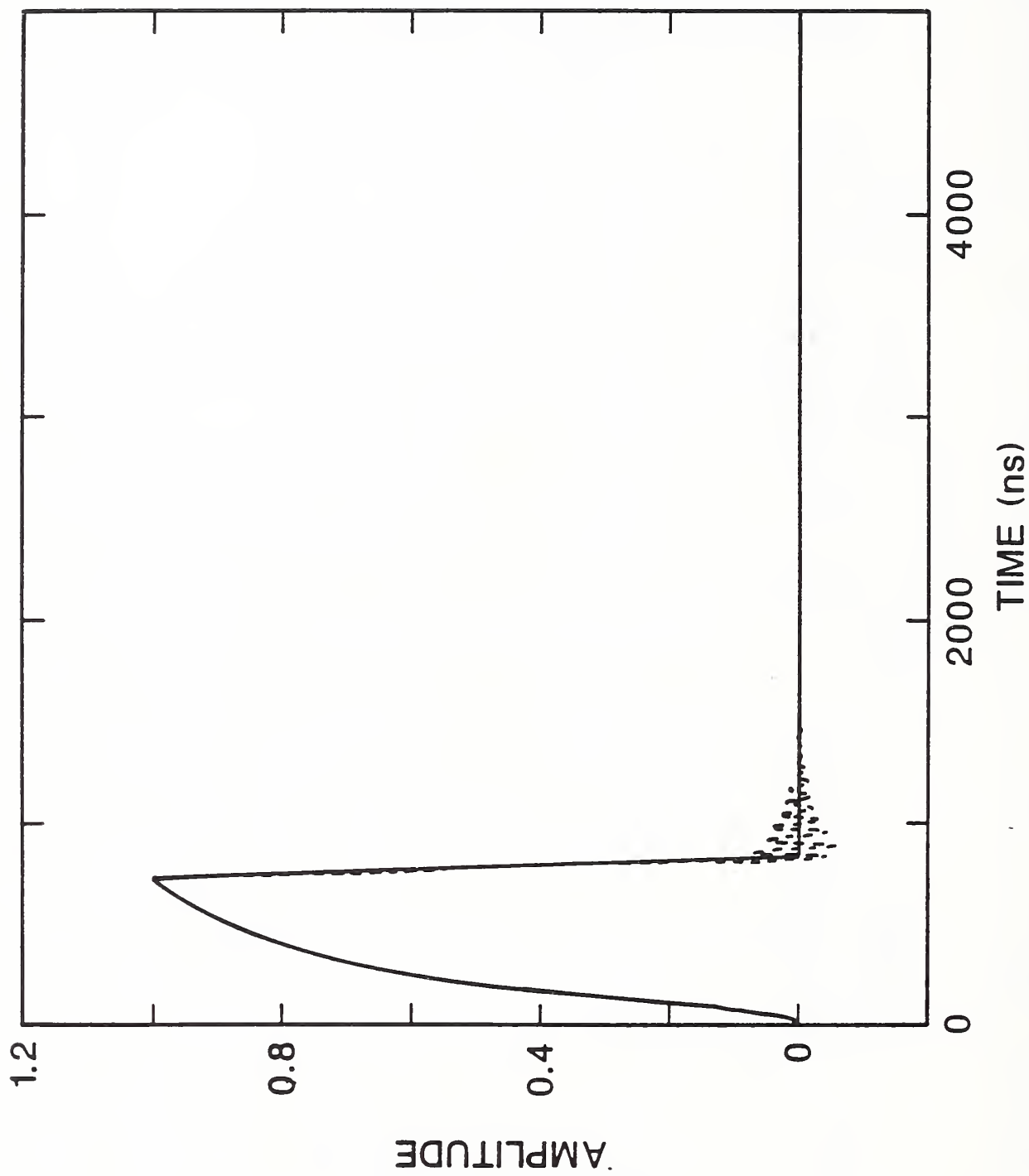
65

Figure 33. Convolutions of step shown in 32 (a) with a chopped waveform constructed by chopping the 0.9x50 waveform at 90 percent of the peak. The chop was a linear 100 ns ramp.
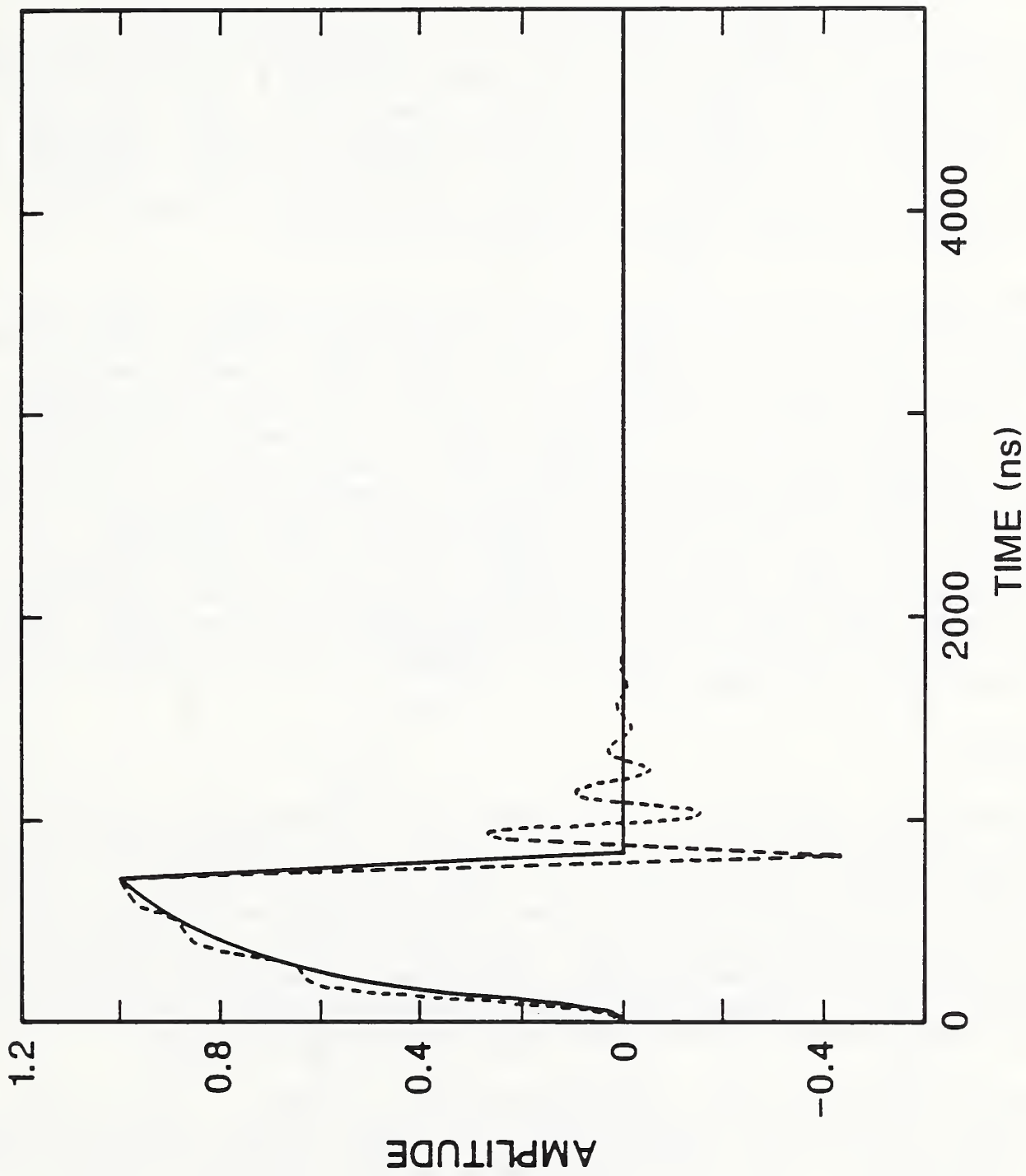
Figure 34. Convolution of step 32 (c) with the wavefom of Fig. 33.

The limitations posed by the use of conventional free-standing dividers to measure pulses faster than those typically used by the power community is shown in Fig. 35. Here, the waveform is the fast waveform 1 from Table 5, and the step response is that of the NBS3 divider configured with no damping resistor. The resulting oscillatory output makes this measurement useless. In contrast, Fig. 36 shows the same waveform with a critically damped response. This calculation presents one of the interesting results to appear in the convolution study. Despite the very large error introduced in the front-time of the waveform due to the inadequate divider response, the error in the peak value is much smaller. Of course, faster dividers can be constructed for these waveforms, but as the required voltage increases this becomes more difficult.

As an example of the distortion that can be introduced in the peak value of a waveform, consider the convolution of fast waveform 2 (Table 5) with the step response of the small resistive divider (shown in Fig. 29) illustrated in figure 37. Although the step response of the divider is almost adequate to follow the waveform, the overshoot produces a significant error. This is an example of a situation where the convolution can be used to judge if the potential error is excessive for the intended measurement.

An additional question about the use of the step response is how the closure speed of the switch involved in the measurement affects the measured step response. A series of convolutions have been done in which ramps of different 0-100% rise times ranging from 1 to 60 ns (for this calculation) were used with an arbitrarily chosen experimental step response for NBS1. The measured step response and its convolution with a ramp step of 60 ns is shown in Fig. 38. Although the distortion of the step response shown in Fig. 38 is significant, the calculations indicated that for this step response, transition times as long as 20 ns had little effect on the step response. This implies that for many dividers designed to measure standard lightning impulses, switches other than the fast mercury relays could be used. This may decrease some of the "noise" problems encountered due to radiation effects associated with fast rise times [56].

5.5 Discussion

In contrast to a calculation method which uses unrealistic signals such as ramps, the convolution method presented can show the effect of the use of a given measuring system, represented by its step response, to measure a signal of a shape which is closely related to the actual signals of interest. The use of this method and the plotting of input and output waveforms is instructive in that the distortion is clearly seen. Intuition may be a poor substitute for calculation, as is evidenced in figure 33, where a highly oscillatory step response has little effect on a chopped lighting-impulse waveform.

It should be emphasized that this method does not address some of the questions raised in historical debate about the step response itself and the methods of obtaining it. The measurement must be done properly, and the individual experimenter must have sufficient expertise and knowledge to insure this. The damping conditions resulting from the internal impedance of the test generator and any external damping resistance in general are not known.
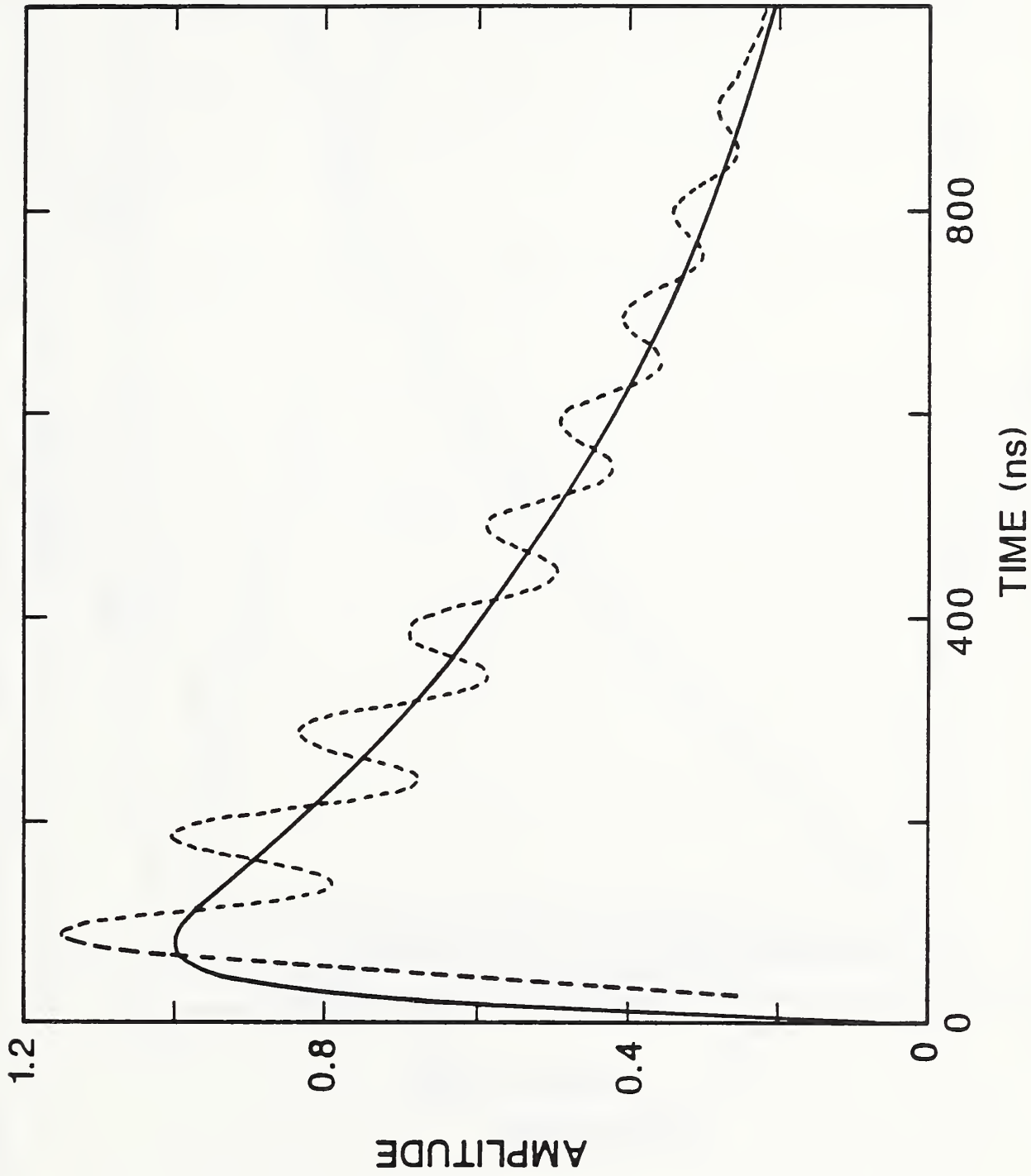
68

Figure 35. Convolution of fast waveform 1 (Table 5) with an undamped step response for NBS3. Observed overshoot is approximately 15 percent.
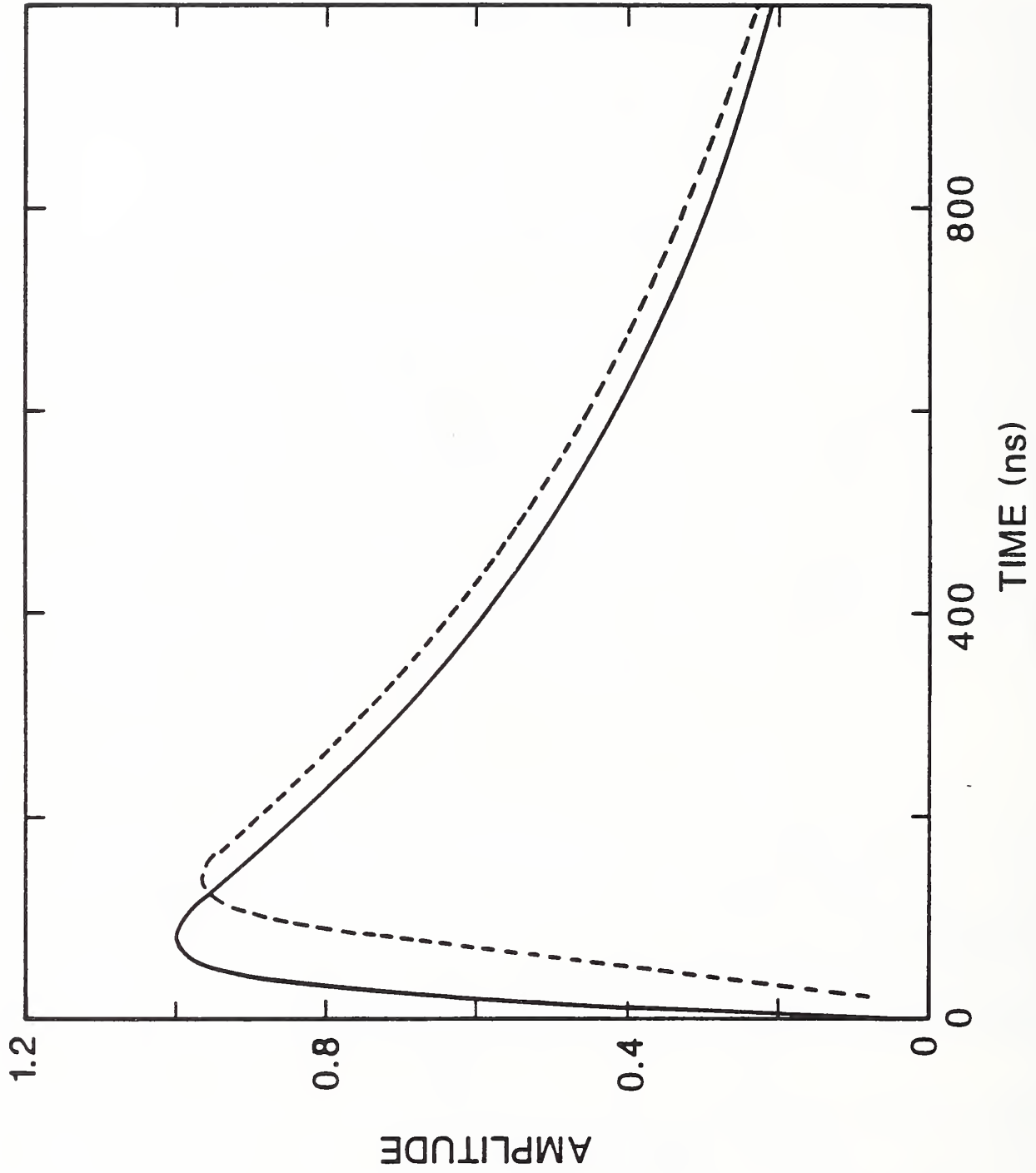
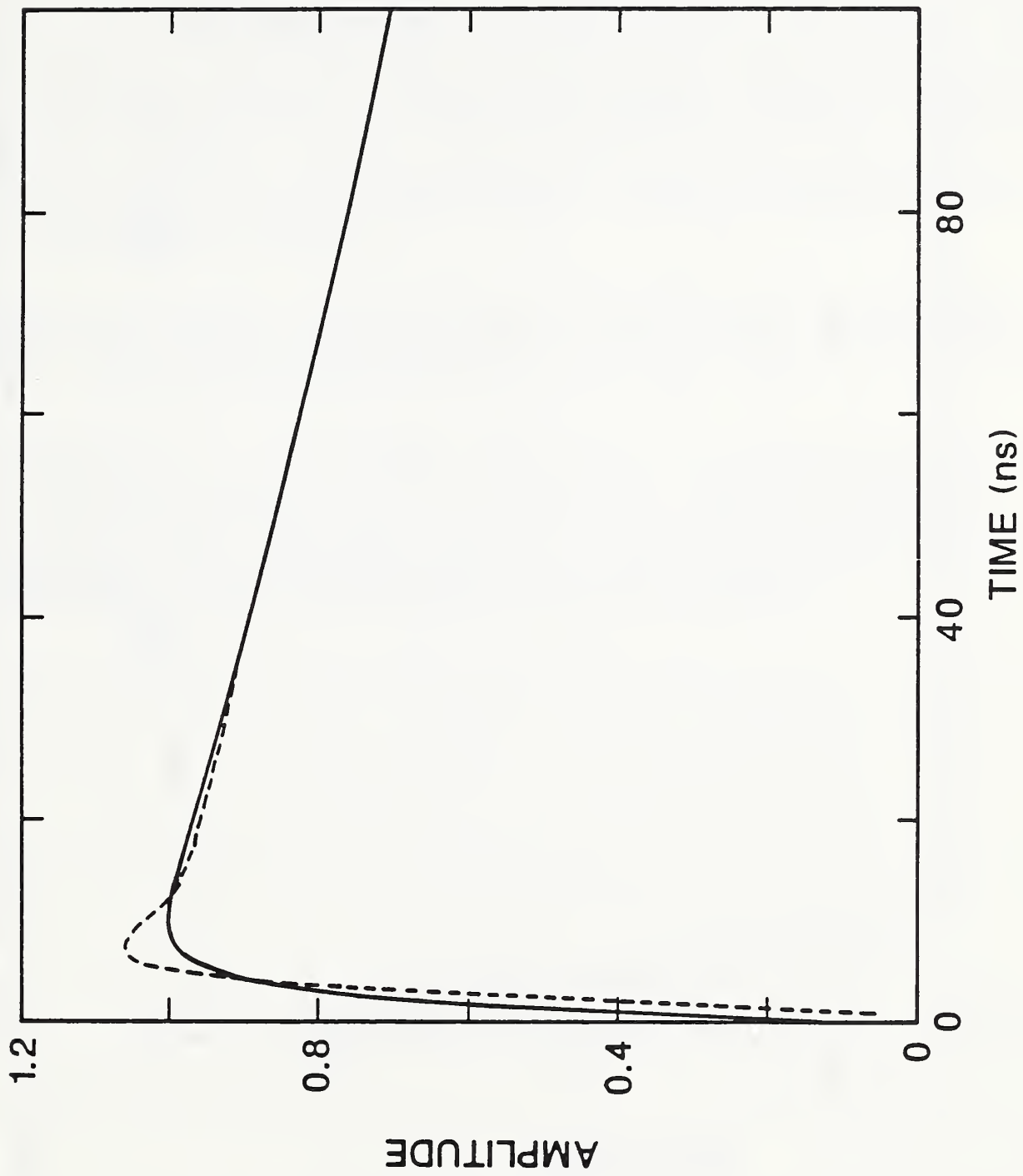Figure 36. Fast waveform 1 convolved with a critically damped step response for NBS3.

Figure 37. Fast waveform 2 (Table 5) convolved with the step response of the resistive divider shown in Fig. 29.
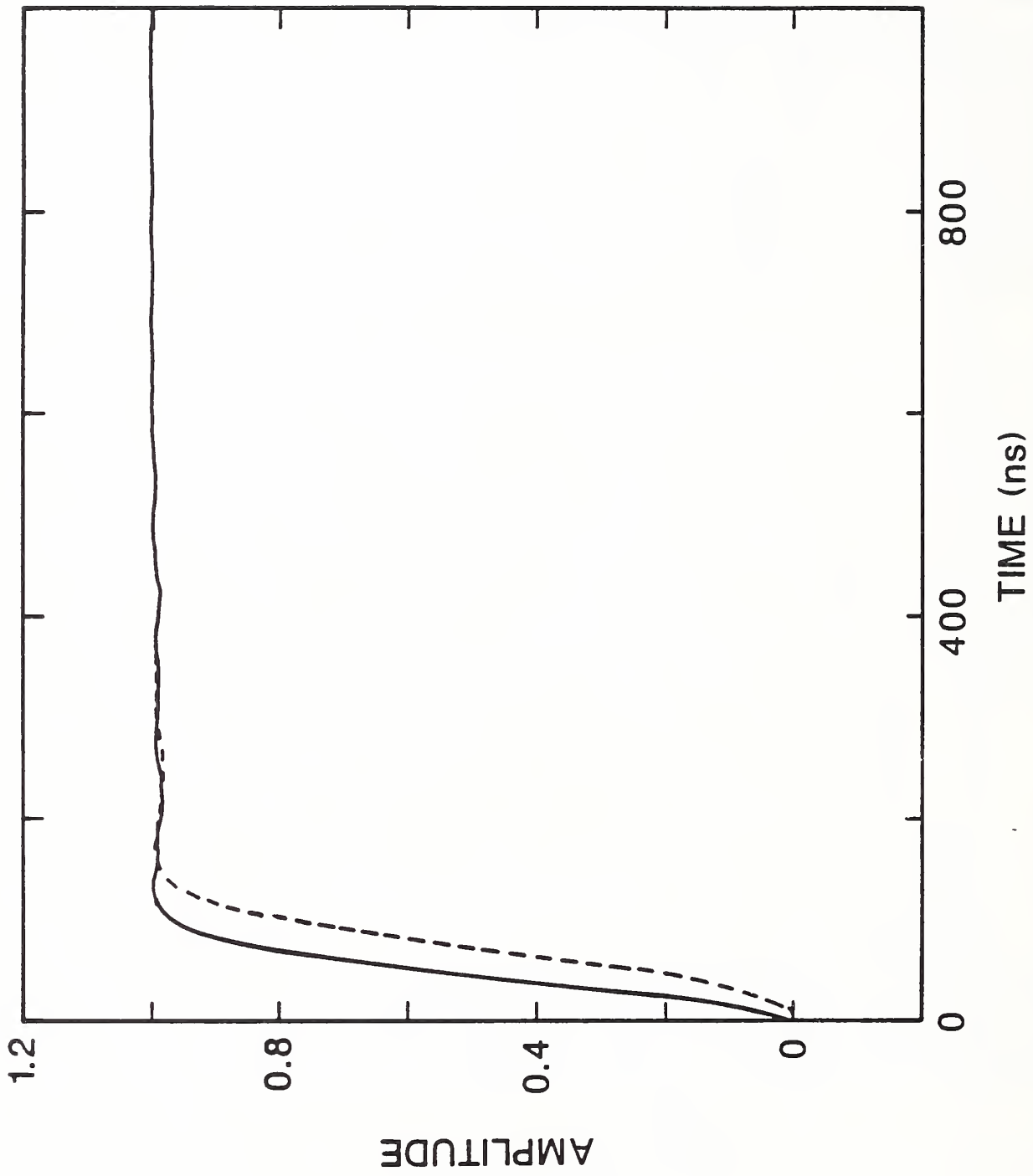
71

Figure 38. Distortion of critically damped step for NBS1 by convolution with a 60 ns (0-100%) ramp. Solid curve is undistorted step, dashed result of calculation.

As a result, only bounds can be placed on the measurement using this method. Considerations of requirements on the data recording system are beyond the context of the present work and are not discussed here.

5.6 Conclusions

The examples of convolution calculations shown above illustrate a method of evaluating a measurement system and are not intended to be exhaustive. Each laboratory would have to measure the step response of its own system by devising a method to produce a step to which the measuring system will respond. For free-standing dividers, the methods outlined in the standards listed previously or those discussed in the literature will suffice. Earlier technical problems, encountered with producing a step with a fast transition time at a high enough voltage to produce any adequate signal to register on the relatively insensitive impulse oscilloscopes, have all but disappeared with the advent of fast, versatile, digital waveform recorders with low level inputs. Frequently, the present day problem is one of attenuating the signal to usable levels during testing.

Waveforms of the type expected in the experiment can be calculated using a simple analytic form as illustrated here, or by using a look-up table in the calculation. An experimentally determined waveform, recorded by a divider known to introduce little distortion, could also be used.

As noted earlier, this approach should not be considered as a method from which correction factors can be obtained for a given measurement. It does appear to be useful however, in providing an evaluation of the application of a given measurement method of known experimental step response to the measurement of well characterized impulse waveforms.

6. REFERENCES

[1] G. W. Griffen, I. Dzidic, D. I. Caroll, R. N. Stillwell and E. C. Horning, "Ion Mass Assignments Based on Mobility Measurements", Anal. Chem., Vol. 45, pp. 1294-1209 (1973).

[2] H. Bohringer, D. W. Fahey, W. Lindinger, F. Howorka, F. C. Fehsenfeld and D. L. Albritton, "Mobilities of Several Mass-Identified Positive and Negative Ions in Air", Int. J. Mass. Spectrom. Ion Phys., Vol. 81, pp. 45-65 (1987).

[3] F. L. Eisele, "Direct Tropospheric Ion Sampling and Mass Identification", Intl. J. Mass Spectrometry and Ion Processes, Vol. 54, pp. 119-126 (1983).

[4] National Institute of Standards and Technology Report NBSIR 87-3643, "Research for Electric Energy Systems--Annual Report", R. E. Hebner, Ed., pp. 1-8 (1987).

[5] E. W. McDaniel and E. A. Mason, "The Mobility and Diffusion of Ions in Gases", Chpt. 2, (John Wiley & Sons, New York, 1973).

[6] A. M. Tyndall and C. F. Powell, "The Mobility of Ions in Pure Gases", Proc. Roy. Soc., Vol. 129, pp. 162-180 (1930).

[7] A solution for the electric potential in the volume enclosed by the guard rings is given in the reference, B. Barber, "The Basic Design Data of a Guarded-field Thimble Ionization Chamber: A Theoretical Investigation," Physics in Medicine and Biology, Vol. 4, pp. 1-9 (1959), assuming a negligible gap width between the guard bands. The electric field in the drift space is found by taking the gradient of the potential. The finite width of the gap between the guard rings appears to have a negligible effect on the electric field for much of the volume if the gap width is less than 10% of the guard band width (L. A .W. Kemp and B. Barber, "The Basic Design Data of a Guarded-Field Thimble Ionization Chamber: A Precision Ionometric Investigation", Physics in Medicine and Biology, Vol. 3, pp. 123-138 (1958).

[8] M. Misakian, "Generation and Measurement of dc Electric Fields with Space Charge", J. Appl. Phys., Vol. 52, pp. 3135-3144 (1981).

[9] M. Misakian and M. Mumma, "Effect of Electron Beam Pulse Width on Time-of-Flight Spectra", Rev. Sci. Instrum., Vol. 45, pp. 296-297 (1974). The right-hand-side of Eq. (2) in this reference should not have a "dt".

[10] J. D. Cobine, "Gaseous Conductors", (Dover, New York, 1958) pp. 55-56.

[11] Reference 5, Chpt. 1.

[12] M. M. Shahin, "Mass-Spectrometric Studies of Corona Discharges in Air at Atmospheric Pressure", J. Chem. Phys., Vol. 45, pp. 2600-2605 (1966).

[13] L. W. Sieck and R. J. Van Brunt, Proc. 15th Int. Conf. on Physics of Electronic and Atomic Coll., Brighton, UK (1987) pp. 710.

[14] L. W. Sieck and R. J. Van Brunt, J. Phys. Chem., Vol. 92 (2), pp. 708-713 (1988).

[15] A. V. Phelps and R. J. Van Brunt, J. Appl. Phys. (in press, 1988).

[16] R. J. Van Brunt, J. T. Herron, and C. Fenimore, Gaseous Dielectrics V, Proc. 5th Int. Symp. on Gaseous Dielectrics, Knoxville (Pergamon Press, NY, 1987) pp. 163-173.

[17] Th. Aschwanden, R. J. Van Brunt, and M. E. Bieber, 18th Int. Conf. on Phenomena in Ionized Gases, Swansea, UK (1987) pp. 102-103.

[18] Th. Aschwanden, R. J. Van Brunt, and A. V. Phelps, Proc. 40th Annual Gaseous Electronics Conf., Atlanta, Bull. Am. Phys. Soc., Vol. 33 (2), pp. 122 (1988).

[19] R. J. Van Brunt, J. Res. NBS, Vol. 90 (3), pp. 229-253 (1985).

[20] R. J. Van Brunt and M. C. Siddagangappa, Plasma Chem. Plasma Proc., Vol. 8 (2) pp. 207-223 (1988); R. J. Van Brunt, L. W. Sieck, I. Sauers, and M. C. Siddagangappa, Plasma Chem. Plasma Proc., Vol. 8 (2) pp. 225-246 (1988).

[21] L. C. Pitchford, S. V. O'Neil, and J. R. Rumble, Phys. Rev. A, Vol. 23, pp. 294 (1981); L. C. Pitchford and A. V. Phelps, Phys. Rev. A, Vol 25, pp. 540 (1982); A. V. Phelps and L. C. Pitchford, Phys. Rev. A, Vol. 31, pp. 2932 (1985).

[22] M. Yousfi, Thesis, Universite Paul Sabatier de Toulouse, Toulouse, France, 1986 (unpublished); P. Sequr, M. Breznotits, and J. P. Zurru, Proc. 40th Annual Gaseous Electronics Conf., Atlanta, Bull. Am. Phys. Soc., Vol. 33 (2), pp. 146 (1988).

[23] V. H. Dibeler and F. L. Mohler, J. Res. NBS, Vol. 40, pp. 25 (1948).

[24] H. F. Winters and M. Inokuti, Phys. Rev. A, Vol. 25, pp. 1420 (1982).

[25] K. A. Blanks, A. E. Tabor, and K. Becker, J. Chem. Phys., Vol. 86, pp. 4871 (1987); K. A. Blanks and K. Becker, J. Phys. B (in press, 1988).

[26] J. L. Forand, Ph.D. Thesis University of Windsor, Canada, 1986 (unpublished).

[27] K. Masek, L. Laska, V. Perina, and J. Krasa, Acta Phys. Slov., Vol. 33, pp. 145 (1983). Since these authors used the two-term approximation to the solution of the Boltzmann equation, their results must be considered questionable.

[28] R. F. Heider, D. G. Sutton, S. N. Suchard, Chem. Phys. Lett., Vol. 37, pp. 243 (1976).

[29] M. C. Siddagangappa, R. J. Van Brunt, and A. V. Phelps, Conf. Record - 1986 IEEE Int. Symp. on Elec. Insul., IEEE, New York, pp. 225-229 (1986).

[30] S. A. Lawton and A. V. Phelps, J. Chem. Phys., Vol. 69, pp. 1055 (1978). See also B. Eliasson and U. Kogelschatz, J. Phys. D, Vol. 19, pp. 1241 (1986); Vol. 20, pp. 1421 (1987). The modified set of electron-O_2 cross sections is tabulated in: A. V. Phelps, Joint Institute for Laboratory Astrophysics Information Center Report No. 28 (unpublished), September 1985.

[31] T. Taniguchi, H. Tagashira, I. Okada, and Y. Sakai, J. Phys. D, Vol. 11, pp. 2281 (1978); T. Taniguchi, K. Kawamura, S. Sakamoto, and H. Tagashira, J. Phys. D, Vol. 15, pp. 1187 (1982).

[32] D. Spence and G. J. Schulz, Phys. Rev. A, Vol. 5, pp. 724 (1972).

[33] J. Comer and G. J. Schulz, J. Phys. B, Vol. 7, pp. L249 (1974); D. A. Parkes, Vacuum, Vol. 24, pp. 561 (1974); B. C. O'Neill and J. D. Craggs, J. Phys. B, Vol. 6, pp. 2625 (1973); D. W. Goodson, R. J. Corbin, and L. Frommhold, Phys. Rev. A, Vol. 9, pp. 2049 (1974); D. A. Price, J. Lucas, and J. L. Moruzzi, J. Phys. D, Vol. 5, pp. 1249 (1972).

[34] Th. Aschwanden, Gaseous Dielectrics IV, Proceedings of the 4th International Symposium on Gaseous Dielectrics, edited by L. G. Christophorou and M. O. Pace (Pergamon, New York, 1984), pp. 24-33; Thesis, ETH, Swiss Federal Institute of Technology, Zurich, 1985 (unpublished). Recently measured electron drift velocities in SF_6, not shown here, by Y. Nakamura (J. Phys. D, Vol. 21, pp. 67 (1988)) are in good agreement with the data of Aschwanden.

[35] H. F. A. Verhaart, Thesis, Technical University of Eindhoven, The Netherlands, 1982 (unpublished).

[36] D. B. Ogle and G. A. Woolsey, J. Phys. D, Vol. 20, pp. 453-461 (1987).

[37] J. T. Herron, Int. J. Chem. Kinetics, Vol. 19, pp. 129-142 (1987).

[38] I. C. Plumb and K. R. Ryan, Plasma Chem. Plasma Proc., Vol. 6, pp. 247-258 (1986).

[39] W. B. DeMore, J. J. Margitan, J. J. Molina, R. T. Watson, R. F. Hampson, M. J. Kurylo, C. J. Howard, and A. R. Ravishankara, Jet Propulsion Laboratory Publication 85-37, pp. 27-102 (1985).

[40] I. Sauers, J. L. Adcock, L. G. Christophorou, and H. W. Ellis, J. Chem. Phys., Vol. 83, pp. 2618-2619 (1985).

[41] R. J. Van Brunt and I. Sauers, J. Chem. Phys., Vol. 85, 4377-4380 (1986).

[42] W. Braun, J. T. Herron, and D. K. Kahaner, Int. J. Chem. Kinetics, Vol. 20, pp. 51-62 (1988).

[43] R. J. Van Brunt, J. Appl. Phys., Vol. 61 (5), pp. 1773-1787 (1987).

[44] J. L. Moruzzi and J. D. Craggs, Proc. 12th Int. Conf. on Phenomena in Ionized Gases, pp. 225 (1975).

[45] B. Hartlieb and H. Winkelnkemper, ETZ-Archiv, Vol. 2, pp. 351-356 (1980).

[46] R. E. Wootton, S. J. Dale, and N. J. Zimmerman, Gaseous Dielectrics II, Proc. 2nd Int. Symp. on Gaseous Dielectrics, Knoxville, Pergamon Press, NY (1980) pp. 137-148.

[47] L. E. Kline, D. K. Davies, C. L. Chen, and P. J. Chantry, J. Appl. Phys., Vol. 50, pp. 6789-6796 (1979).

[48] M. C. Siddagangappa, C. S. Lakshminarasimha, and M. S. Naidu, J. Phys. D, Vol. 16, pp. 763 (1983); Vol. 15, pp. L83 (1982); Vol. 16, pp. 1595 (1983); IEEE Trans. Elec. Insul., Vol. EI-19, pp. 359 (1984).

[49] M. S. Naidu and A. N. Prasad, J. Phys. D, Vol. 5, pp. 1090 (1972).

[50] K. B. McAfee, J. Chem. Phys., Vol. 23, pp. 1435 (1955); D. Edelson and K. B. McAfee, Rev. Sci. Instr., Vol. 35, pp. 187 (1964).

[51] M. Hayashi (unpublished).

[52] M. S. Bhalla and J. D. Craggs, Proc. Phys. Soc. London, Vol. 80, pp. 151 (1962).

[53] E. F. Kelley and R. E. Hebner, "The Electric Field Distribution Associated with Prebreakdown Phenomena in Nitrobenzene," J. Appl. Phys., Vol. 52, No. 1, pp. 191-195 (Jan. 1981).

[54] T. J. Gallagher, "Simple Dielectric Liquids -- Mobility, Conduction, and Breakdown," (Oxford University Press, London, 1975) chapter 2.

[55] W. C. Elmore, "The Transient Response of Damped Linear Networks
with Particular Regard to Wideband Amplifiers," J. Appl. Phys.,
Vol. 19, pp. 55-63 (1948).

[56] IRR-IMS-Group: "Facing UHV Measuring Problems," Electra No. 35
(July 1974).

[57] W. R. Fowkes and R. M. Rowe, "Refinements in Precision Kilovolt
Pulse Measurements," IEEE Trans. Inst. and Meas., Vol. IM-15, pp.
284-292, 1966.

[58] A. V. Oppenheim, A. S. Willsky with I. T. Young, Signals and
Systems, (Prentice-Hall Signal Processing Series, Prentice-Hall,
1983).

[59] IEEE Standard Techniques for High Voltage Testing, IEEE Std 4-1978.

[60] International Electrotechnical Commission, High Voltage Test
Techniques, IEC Publication 60-1, 2, 3, 4, 1973-1977.

[61] N. Hylten Cavallius and T. Parnell, "The Measurement of Standard
Lightning Impulses," Third International High Voltage Symposium,
Milan, August 1979, Vol. 2, paper 42.05.

[62] Qi, Qing-Cheng and W. S. Zaengl, "Investigations of Errors Related
to the Measured Virtual Front Time T_1 of Lightning Impulses," IEEE
Trans. on Power Apparatus and Systems, Vol. PAS-102, pp. 2379-2390
(1983).

[63] N. Hylten-Cavallius, F. A. Chagas and A. Chakrabarti, "A New
Approach to Minimize Response Errors in the Measurement of High
Voltage Impulses," IEEE Trans. Pow. Appar. Syst., Vol. PAS-102,
pp. 2077-2091, (1983).

[64] F. C. Creed and M. M. C. Collins, "The Measurement of Short-
Duration Impulse Voltages," IEEE Trans. on Communication and
Electronics, Vol. 82, pp. 621-630 (1963).

[65] F. C. Creed, T. Kawamura and G. Newi, "The Step Response of
Measuring Systems for High Impulse Voltages," IEEE Trans. Pow.
Appar. Syst., Vol. PAS-86, No. 11, pp. 1408-1420 (1967).

[66] A. Pedersen and P. Lausen, "Dynamic Properties of Impulse Measuring
Systems," IEEE Trans. Pow. Appar. Syst., Vol. PAS-90, pp. 1424-1432
(1971).

[67] F. C. Creed and M. M. C. Collins, "Transient Impedance of High-
Voltage Impulse Generating Systems," IEEE TRAns. Pow. Appar. Syst.
Vol. Pas-89, pp. 1387-1393, (1970).

[68] Draft--High Voltage Test Techniques Revision of Publication 60-3
and 60-4; Prepared by WG7 of IEC/TC42 (undated).

[69] D. Kind, H. Korff, A. Schmidt and K. Schon, "Chopping Errors for Characterizing HV Impulse Dividers," paper 71.02, Fifth International Symposium on High Voltage Engineering, Braunschweig, FRG, 1987.

[70] R. E. Hebner and S. Annestrand, "Evaluation of Calibration Techniques for Multimegavolt Impulse Dividers," Third International High Voltage Symposium, Milan, August 1979, Vol. 2, paper 42.18.

[71] H. Link, Discussion of reference 10 (this paper), IEEE Trans. Pow. Appar. Syst. Vol. PAS-86, pp. 1417-1418, (1967).

[72] Y. X. Zhang, R. H. McKnight, and R. E. Hebner, "Interactions Between Two Dividers Used in Simultaneous Comparison Measurements," to be presented at the Summer Meeting of the IEEE Power Engineering Society, 1988.

[73] R. H. McKnight and H. K. Schoenwetter, "Capacitive Sensors for Voltage Measurements in Pulse Power Systems," Conference Record of 1984 Sixteenth Power Modulator Symposium (June, 1984).

[74] R. Malewski, Y. Gervais and M. Zwicky, "Resistor Voltage Divider for Impulse Measurements in SF_6 Test Vessels," in Proceedings of Fourth International Symposium on High Voltage Engineering, Athens, Greece, National Technical University, 1983.

[75] M. Kromholz, J. Doggett, K. H. Shoenbach, J. Gahl, C. Harjes, G. Schaefer and M. Kristiansen, "Nanosecond Current Probe for High-Voltage Experiments," Rev. Sci. Inst., Vol. 55, pp. 127-128 (1984).

[76] H. D. Sutphin, "Subnanosecond High Voltage Attenuator," Rev. Sci. Inst., Vol. 43, pp. 1535-1536 (1972).

[77] Z. Y. Lee, "Subnanosecond High-Voltage Two-Stage Resistive Divider," Rev. Sci. Inst., Vol. 54, pp. 1060-1062 (1983).

[78] T. R. McComb, R. C. Hughes, H. A. Lightfoot, K. Schon, R. Schulte, R. H. McKnight, and Y. X. Zhang, "International Comparison of HV Impulse Measuring Systems," to be presented at the Summer Meeting of the IEEE Power Engineering Society, 1988.

U.S. DEPT. OF COMM. BIBLIOGRAPHIC DATA SHEET (See instructions)	1. PUBLICATION OR REPORT NO. NISTIR 88-3886	2. Performing Organ. Report No. 728	3. Publication Date November 1988

4. TITLE AND SUBTITLE

Research for Electric Energy Systems -- An Annual Report

5. AUTHOR(S)

Richard J. Van Brunt, editor

6. PERFORMING ORGANIZATION (If joint or other than NBS, see instructions) NATIONAL BUREAU OF STANDARDS U.S. DEPARTMENT OF COMMERCE GAITHERSBURG, MD 20899	7. Contract/Grant No. 8. Type of Report & Period Covered

9. SPONSORING ORGANIZATION NAME AND COMPLETE ADDRESS (Street, City, State, ZIP)

U.S. Department of Energy
Division of Electric Energy Systems
1000 Independence Avenue, N.W.
Washington, D.C. 20585

10. SUPPLEMENTARY NOTES

☐ Document describes a computer program; SF-185, FIPS Software Summary, is attached.

11. ABSTRACT (A 200-word or less factual summary of most significant information. If document includes a significant bibliography or literature survey, mention it here)

This report summarizes the technical accomplishments during fiscal year 1987 from a U.S. Department of Energy sponsored program at the National Bureau of Standards to provide technical support for DOE's research on electrical energy systems. Major activities associated with each of the four subtasks that constitute the program are highlighted. These include research on: 1) electric field and ion measurements; 2) fundamental physical and chemical processes in commonly used gaseous dielectrics like SF_6; 3) development of advanced methods for observing and catagorizing prebreakdown interfacial phenomena in liquid dielectrics; and 4) evaluation of advanced methods for characterizing transient measurements by use of step response and convolution integrals as they apply to free standing dividers.

12. KEY WORDS (Six to twelve entries; alphabetical order; capitalize only proper names; and separate key words by semicolons)

convolutions; collision cross sections; dividers; drift tubes; insulation; ion mobilities; ion-molecule reactions; liquid dielectrics; optical delay; partial discharges; step response; sulfur hexafluoride

13. AVAILABILITY	14. NO. OF PRINTED PAGES
☒ Unlimited ☐ For Official Distribution. Do Not Release to NTIS ☐ Order From Superintendent of Documents, U.S. Government Printing Office, Washington, D.C. 20402.	85
	15. Price
☒ Order From National Technical Information Service (NTIS), Springfield, VA. 22161	$13.95